RÉPUBLIQUE ALGÉRIENNE DÉMOCRATIQUE ET POPULAIRE
MINISTÈRE DE L'ENSEIGNEMENT SUPÉRIEUR ET DE LA RECHERCHE SCIENTIFIQUE

FERHAT ABBAS UNIVERSITY-SETIF1
FACULTY OF SCIENCES
DEPARTMENT OF PHYSICS

THESIS

Presented for the degree of

DOCTORATE 3$^{\text{rd}}$ cycle

In: Physics
Specialty: Theoretical Physics

By: ***Sana MEKHALFA***

TITLED

(e,2e) and (e,3e) reaction of Nitrogen Molecule: Study of Charge Effects and Post Collisional Interaction.

Publicly defended on // before the examination committee:

Mr. Kamel BENCHEIKH	Prof. at UFA Sétif-1	Chair
Mr. Messaoud NEMOUCHI	Prof. at USTHB	Examiner
Mr. Boumedienne LASRI	Prof. at UNIV SAIDA	Examiner
Mrs. Imene KADA	Prof. at UFA Sétif-1	Examiner
Mr. Abdelaziz MANSOURI	Prof. at UFA Sétif-1	Supervisor
Mr. Salim HOUAMER	Prof. at UFA Sétif-1	Co-Supervisor
Mr. Mohamed MOULAY	Senior Research Director at (H.C.R.)	Invited member

I dedicate this work to the memory of my beloved father, Dr. Mekhalfa Abdelmalek, whose integrity, dedication to knowledge, and unwavering belief in education continue to inspire me. Although he is no longer with us, his values and guidance remain a constant presence throughout my life and in every step of this achievement.

I also dedicate this thesis to my family, whose unconditional love, patience, and sacrifices have been my greatest source of strength.

Finally, I dedicate this work to my dear friends Laifa Dounia, Rahba Kamilia, and Grar Khaoula for their understanding, encouragement, and constant support throughout this journey.

Acknowledgement

I would like to express my sincere gratitude to my thesis director, Prof. Abdelaziz Mansouri, and my co-director, Prof. Salim Houamer, for their continuous guidance, patience, and invaluable scientific support throughout the course of this work. Their expertise, insightful advice, and encouragement were essential to the successful completion of this thesis.

I am deeply grateful to the members of my examination jury for accepting to evaluate this work and for the honor of their presence and contributions: Prof. Kamel Bencheikh, Prof. Messaoud Nemouchi, Prof. Boumedienne Lasri, and M.C.A. Imene Kada. I would also like to sincerely thank the invited member of the jury, Mr. Mohamed Moulay, for his interest in this work and for his valuable participation.

This research was carried out at the Laboratory of Quantum Physics and Dynamic Systems (LPQSD) at Ferhat Abbas University Sétif 1. I would like to acknowledge the laboratory for providing a stimulating scientific environment and the necessary resources to conduct this research.

My sincere thanks go to my laboratory colleagues and friends Zaidi Omar, Tamin Ayoub, Khiat Imene, Sakhraoui Wafa, and Attia Maroua not only for the academic exchanges we shared, but also for their friendship, kindness, and constant moral support, which made the research environment both motivating and enjoyable.

I would also like to express my sincere thanks to Louamri Mohamed Messaoud for his support throughout my entire PhD journey, and for his constant presence and understanding, which were invaluable along the way.

ملخص

تمَّت دراسة عملية التأيّن الأحادي والمزدوج لجزيء النيتروجين في نطاقات طاقة متوسطة إلى منخفضة في حالة التأيّن الأحادي، تم حساب الـ*TDCS* باستخدام نموذج *M3CWZ* الذي يتضمن تفاعلات ما بعد التصادم وتأثيرات التشويه لكلٍّ من تصادمات الإلكترونات والبوزيترونات. أمّا في حالة التأيّن المزدوج، فقد تم الحصول على الـ*5DCS* والـ*4DCS* في إطار تقريب بورن الأوّل باستخدام نموذج *2CWG* لتأيّن الجزيء بتأثير تصادم الإلكترونات.

الكلمات المفتاحية:التأين، تأثير الإلكترون والبوزيترون، تأثيرات التشويه، تفاعل ما بعد التصادم.

Abstract

Single and double ionization of the nitrogen molecule have been investigated in intermediate to low energy regimes. For single ionization, the TDCS was calculated using the M3CWZ model, which includes post-collisional interactions and distortion effects for both electron and positron impact. For double ionization, the 5DCS and 4DCS were obtained within the first Born approximation using the 2CWG model for electron impact ionization.

Keywords: ionization, electron and positron impact, distortion effects, post-collision interaction.

Résumé

La simple et la double ionisation de la molécule d'azote ont été étudiées dans des régimes d'énergie intermédiaire à faible. Pour la simple ionisation, la TDCS a été calculée à l'aide du modèle *M3CWZ*, qui inclut les interactions post-collisionnelles et les effets de distorsion pour l'impact d'électrons et de positrons. Pour la double ionisation, les 5DCS et 4DCS ont été obtenues dans le cadre de la première approximation de Born en utilisant le modèle *2CWG* pour l'ionisation par impact d'électrons.

Mots-clés : ionisation, impact d'électron et de positron, effets de distorsion, interaction post-collision

Contents

List of Figures

List of Tables

Introduction

The study of atomic and molecular ionization by charged-particle impact is a central tool for probing the structure and dynamics of matter. Ionization processes play key roles not only in fundamental atomic and molecular physics but also in applied areas such as plasma physics, astrophysics, and even life sciences. On one hand, Single ionization of atoms and molecules by electron impact have been widely investigated experimentally and theoretically for a long time offering a precious knowledge of the problem [1–4], while studies dealing with positron-impact ionization are still in the nascent stage. Using both positrons and electrons as projectile might enable to isolate competing interactions which are not detected by a single particle as projectile. In addition, insights to the post collision interaction could also be gained in experiments with both positron and electron projectiles, the goal is ultimately to test the theoretical model in more details. The interest is mainly focused on kinematically complete experiments where the measured fully differential cross section provides the most detailed information on the dynamics of the ionization reaction. It should be noted that positron impact ionization faces some practical difficulties particularly at low impact energy, where the direct ionization is inevitably accompanied by competition of positronium formation process [5]. Another problem is that positron beam intensities are orders of magnitude smaller than those of electrons, TDCS measurements for positron impact are therefore much less available compared to electrons. Despite the great success of the theory for electron impact ionization through (e,2e) studies for atoms [6–8] and molecules [9–11], the ionization reaction of low to intermediate energy interaction is not fully understood even for atomic targets [12]. Studies on positron-impact ionization are much less advanced but are currently growing, the major interest is ultimately to provide additional information that was previously unavailable. From a practical point of view, it is necessary that reliable experiments exist in order to benchmark the theory. Measurements of the TDCS have been realized in particular for argon in a wide range of kinematics [13, 14], and extended to further experiments for other atoms [15, 16] and molecules [17, 18]. Meanwhile, numerous sophisticated theoretical models have been developed for (e,2e) reaction for atoms [19–21] and molecules [22–24], developed theories have moreover provided a rich source of information on atomic and molecular targets, where good agreement was found between experiment and theory for a long range of different targets. Historically, the (e,2e) process was much more investigated, each of the developed models uses different kinds of approximations whose accuracy was checked by direct confrontation with experiments. For atoms, highly sophisticated approaches have achieved considerable success in providing accurate experimental data like DWBA [25], CCC [26], and BSR [27], and appear to be among ones of the most reliable alternatives for modeling the ionization process of complex many-electron systems. For molecules the most currently known are DWBA [28], M3DW [29] and MCTDW [30] models. One assertion that has caught particular interest in studying ionization processes by positron impact is that experimental data could provide detailed information on charge effects. Positron impact studies are usually investigated using theories that are similar to standard models developed for electron impact processes [31–33] by simply changing the sign of the projectile charge. The change in the sign of the projectile charge will induce an inversion of the direction of the electric field between the positron and the target, which will likely lead to some differences between the TDCSs exhibited for positron or electron projectiles. In recent publications, a model called 3CWZ was used to investigate the ionization of argon atom by electrons [34] and positrons [35]. The model was subsequently extended to molecular targets and called M3CWZ, TDCS calculations for (e,2e) process of water molecule were reported and compared with a complete set of experiments performed at low impact energies [36]. This model, takes into account the exchange effects and the post collision interaction (PCI), and it was shown to reproduce results in overall good agreement with the data, and to perform as well as other sophisticated models like M3DW. The M3CWZ is now used to study the ionization reaction of nitrogen molecule by electron and positron impact, the present investigation focuses on TDCS measurements for N_2 molecule, performed in a range of intermediate impact energy regime (200-700 eV). Different kinematics in coplanar asymmetric geometries, varying from small to large momentum transfer are therefore considered, offering a more stringent test for theory.

Double ionization (DI) of atoms and molecules by electron impact is a particularly challenging process to study in coincidence experiments, and it has been extensively investigated both experimentally and theoretically. The pioneering work of Lahmam-Bennani *et al.* [37] provided the first *(e,3e)* measurements of the DI reaction for argon, in which the scattered projectile and the two ejected electrons were detected in triple coincidence. These experiments were later extended to a variety of atomic and molecular targets—including He, Kr, Ne, Mg, CH_4, H_2O, and N_2 over a broad range of incident energies [38–50]. Complementary *(e,3-1e)* studies were also performed using double-coincidence techniques, where only two of the three outgoing electrons are detected and the third is integrated over all emission angles [51–60]. The principal observables in these kinematically complete experiments are the five-fold differential cross section (FDCS) for (e,3e) and the four-fold differential cross section (4DCS) for (e,3-1e), which provide the most detailed information on the collision dynamics.

To interpret these measurements and to unravel the mechanisms of DI, numerous theoretical models have been developed. Early approaches employed perturbative methods such as the first- and second-Born approximations combined with three-Coulomb (3C/BBK) final states, which enforce correct Coulomb boundary conditions for the two ejected electrons. Refinements including the Gamow and Ward Macek factors were introduced to approximate the mutual repulsion of the outgoing electrons while reducing computational complexity. Other frameworks incorporate distorted waves for the incident and outgoing electrons, for example the distorted-wave Born approximation (DWBA) models applied to argon and magnesium, sometimes with explicit initial- and final-state correlations. Highly accurate but numerically demanding non-perturbative methods such as the convergent close-coupling (CCC) approach, the 6C model, the J-matrix method, and expansions in generalized Sturmian functions have achieved excellent agreement with data for helium and remain benchmarks for simpler systems.

These theoretical efforts aim to describe the competing mechanisms of DI [61–64]. At high incident energies, the process is often dominated by first-order mechanisms such as *shake-off* (SO), where the sudden removal of one electron causes the second to escape, and *two-step-1* (TS1), where the incident electron directly ejects both electrons in a single interaction. As the impact energy decreases to the intermediate range, second-order *two-step-2* (TS2) mechanisms become increasingly important: the projectile first ionizes one electron, and a subsequent interaction either by the projectile or by the first ejected electron knocks out the second. Post-collision interactions between the outgoing electrons further influence the angular distributions and energy sharing, making the FDCS and 4DCS sensitive probes of electron-electron correlation.

This thesis is organized as follows: Chapter 1 establishes the fundamental theoretical framework for single ionization. It details the (e,2e) reaction, conservation laws, experimental techniques, and kinematic considerations. Key theoretical models, including the BBK, DWBA, M3DW, and the M3CWZ model, are introduced and their approaches to describing the transition amplitude and differential cross-sections are outlined.

Chapter 2 focuses on the theoretical framework for double ionization processes. It introduces the (e,3e) reaction and discusses experimental approaches such as complete coincidence (e,3e) and partially coincidence (e,3–1e) measurements, which yield Five-Fold

(5DCS) and Four-Fold (4DCS) differential cross-sections, respectively. The double ionization mechanisms, namely Shake-Off (SO), Two-Step 1 (TS1), and Two-Step 2 (TS2) are explained providing insights into the electron-electron correlation dynamics. The chapter concludes by reviewing key theoretical models employed to describe these complex interactions, including extensions of the BBK model, the Two Coulomb Waves with Gamow factor (2CWG) model, the Two Coulomb Waves with Ward and Macek factor (2CWWM), and the correlated Two-Center double Continuum (TCC-C) model.

Chapter 3 details the target system, the diatomic nitrogen molecule (N_2). It begins with a general description of physical and symmetry properties, followed by the formulation of the molecular Hamiltonian and the application of the Born-Oppenheimer approximation. The core of the chapter addresses the construction of molecular orbitals (MOs) using the Linear Combination of Atomic Orbitals (LCAO-MO) method. The chapter concludes by outlining the transformation formalism between laboratory and molecular frames using Euler angles, essential for comparing theoretical calculations with experimental data.

Chapter 4 examines the single ionization of molecular nitrogen N_2 by both electron and positron impact in the intermediate energy regime, using the M3CWZ model. An Electron Momentum Spectroscopy (EMS) study is performed to validate the molecular orbitals employed. Theoretical calculations of Triple Differential Cross Sections (TDCS) for the ionization of valence orbitals ($2\sigma_g$, $2\sigma_u$,$1\pi_u$ and $3\sigma_g$) are presented and compared with available experimental data and other theoretical models (DWBA, M3DW) under different kinematic conditions. The analysis emphasizes the role of post-collisional interactions, projectile charge effects (positron vs. electron), and the model's ability to reproduce binary and recoil peak features in the angular distributions.

Chapter 5 investigates the electron impact double ionization of the outermost $3\sigma_g$ orbital of the nitrogen molecule using the Two Coulomb Waves with Gamow factor (2CWG) model, operating within the First Born approximation. Calculations of both Four-Fold Differential Cross Sections (4DCS) for (e,3–1e) process and Five-Fold Differential Cross Sections (5DCS) for (e,3e) process are presented and are compared with experimental measurements and other theoretical models, such as the second Born approximation A3C model and the correlated Two-Center double Continuum (TCC-C) model. The discussion focuses on interpreting the observed structures in the cross-sections by considering the contributions of first- and second-order double ionization mechanisms (SO, TS1, TS2).

Bibliography

[1] M. Cherid, A. Lahmam-Bennani, A. Duguet, R. R. Zurales, R. W. Lucchese, M. C. Dal Cappello, and C. Dal Cappello. Triple differential cross sections for molecular hydrogen, both under Bethe ridge conditions and in the dipolar regime. Experiments and theory. *J. Phys. B: At. Mol. Opt. Phys*, **22**(21):3483–3499, 1989.

[2] D. S. Milne-Brownlie, S. J. Cavanagh, Birgit Lohmann, C. Champion, P. A. Hervieux, and J. Hanssen. Dynamics in electron-impact ionization of H_2O. *Phys. Rev. A*, **69**(3):032701, 2004.

[3] I. Bray. Convergent close-coupling calculations of electron-impact ionization of hydrogen. *J. Phys. B*, **33**(3):581–595, 2000.

[4] K. Bartschat and I. Bray. Electron-impact ionization of atomic hydrogen from the 1s and 2s states. *J. Phys. B*, **29**(15):L577–L583, 1996.

[5] P. K. Biswas, J. S. E. Germano, and T. Frederico. Positron-hydrogen molecule scattering considering the positronium-formation channel. *J. Phys. B*, **35**(18):L409–L418, 2002.

[6] A. S. Kheifets, A. Naja, E. M. S. Casagrande, and A. Lahmam-Bennani. DWBA-G calculations of electron impact ionization of noble gas atoms. *J. Phys. B*, **41**(14):145201, 2008.

[7] O. Zatsarinny and K. Bartschat. Nonperturbative treatment of electron-impact ionization of Ar(3p). *Phys. Rev. A*, **85**(3):032708, 2012.

[8] K. Wang, O. Zatsarinny, and K. Bartschat. Electron-impact excitation and ionization of atomic boron at low and intermediate energies. *Phys. Rev. A*, **93**(5):052715, 2016.

[9] S. Houamer, M. Chinoune, and C. Dal Cappello. Theoretical study of (e, 2e) process of atomic and molecular targets. *Eur. Phys. J. D*, **71**(1):17, 2017.

[10] J. Zhou, E. Ali, M. Gong, S. Jia, Y. Li, Y. Wang, Z. Zhang, X. Xue, D. V. Fursa, I. Bray, X. Chen, D. Madison, A. Dorn, and X. Ren. Absolute triple differential cross sections for low-energy electron impact ionization of biochemically relevant systems: Water, tetrahydrofuran, and hydrated tetrahydrofuran. *Phys. Rev. A*, **104**(1):012703, 2021.

[11] X. Li, M. Gong, L. Liu, Y. Wu, J. Wang, Y. Qu, and X. Chen. Triple differential cross sections for electron-impact ionization of tetrahydrofuran. *Phys. Rev. A*, **95**(1):012703, 2017.

[12] X. Ren, A. Senftleben, T. Pflüger, A. Dorn, K. Bartschat, and J. Ullrich. Signatures of projectile–nucleus scattering in three-dimensional (e,2e) cross sections for argon. *J. Phys. B*, **43**(3):035202, 2010.

[13] O. G. de Lucio, J. Gavin, and R. D. DuBois. Differential electron emission for single and multiple ionization of argon by 500 eV positrons. *Phys. Rev. Lett.*, **97**(24):243201, 2006.

[14] J. Gavin, O. G. de Lucio, and R. D. DuBois. Triply differential measurements of single ionization of argon by 1-kev positron and electron impact. *Phys. Rev. A*, **95**(6):062703, 2017.

[15] G. Purohit, P. Singh, V. Patidar, Y. Azuma, and K. K. Sud. Effects of target polarization and postcollision interaction on the electron-impact single ionization of Ne 2p, Ar 3p, and Na 3s atoms. *Phys. Rev. A*, **85**(2):022714, 2012.

[16] R. I. Campeanu, H. R. J. Walters, and C. T. Whelan. Electron- and positron-impact ionization of inert gases. *Phys. Rev. A*, **97**(6):062702, 2018.

[17] P. Singh, G. Purohit, C. Champion, and V. Patidar. Electron- and positron-induced ionization of water molecules: theory versus experiment at the triply differential scale. *Phys. Rev. A*, **89**(3):032714, 2014.

[18] O. G. de Lucio and R. D. DuBois. Differential studies and projectile charge effects in ionization of molecular nitrogen by positron and electron impact. *Phys. Rev. A*, **93**(3):032710, 2016.

[19] I. Bray, D. V. Fursa, A. S. Kheifets, and A. T. Stelbovics. Electrons and photons colliding with atoms: Development and application of the convergent close-coupling method. *J. Phys. B*, **35**(15):R117, 2002.

[20] O. Zatsarinny and K. Bartschat. Nonperturbative treatment of ionization with excitation of helium by electron impact. *Phys. Rev. Lett.*, **107**(2):023203, 2011.

[21] A. L. Harris, D. H. Madison, J. L. Peacher, M. Foster, K. Bartschat, and H. P. Saha. Effects of the final-state electron-ion interactions on the fully differential cross sections for heavy-particle-impact ionization of helium. *Phys. Rev. A*, **75**(3):032718, 2007.

[22] M. Chinoune, S. Houamer, C. Dal Cappello, and A. Galstyan. Application of a post-collisional-interaction distorted-wave model for (e, 2e) of some atomic targets and methane. *J. Phys. B*, **49**(20):205201, 2016.

[23] D. H. Madison and O. Al-Hagan. The distorted-wave Born approach for calculating electron-impact ionization of molecules. *J. At. Mol. Opt. Phys.*, **2010**:367180, 2010.

[24] E. Acebal and S. Otranto. Continuum-distorted-wave eikonal-initial-state description of the electron-impact ionization of H_2O at low impact energies. *Phys. Rev. A*, **98**(1):012703, 2018.

[25] A. S. Kheifets, A. Naja, E. M. Staicu Casagrande, and A. Lahmam-Bennani. DWBA-G calculations of electron impact ionization of noble gas atoms. *J. Phys. B*, **41**(14):145201, 2008.

[26] I. Bray. Close-coupling approach to Coulomb three-body problems. *Phys. Rev. Lett.*, **89**(27):273201, 2002.

[27] O. Zatsarinny and K. Bartschat. Nonperturbative B-spline R-matrix-with-pseudostates calculations for electron-impact ionization of helium. *Phys. Rev. A*, **85**(6):062709, 2012.

[28] A. L. Monzani, L. E. Machado, M. T. Lee, and A. M. Machado. Intermediate-energy electron-impact ionization of molecules. *Phys. Rev. A*, **60**(1):R21–R24, 1999.

[29] J. Gao, D. H. Madison, and J. L. Peacher. Distorted wave Born and three-body distorted wave Born approximation calculations of the fully differential cross section for electron-impact ionization of nitrogen molecules. *J. Chem. Phys.*, **123**(20):204314, 2005.

[30] M. Gong, X. Li, S. B. Zhang, L. Liu, Y. Wu, J. Wang, Y. Qu, and X. Chen. Theoretical study of (e, 2e) triple differential cross section of $1b_{3g}$ orbital of pyrimidine. *Phys. Rev. A*, **96**(4):042703, 2017.

[31] G. Purohit and D. Kato. Projectile charge effects on the differential cross sections for the ionization of molecular nitrogen by positrons and electrons. *J. Phys. B*, **51**(13):135202, 2018.

[32] R. I. Campeanu and C. T. Whelan. Few body effects in the electron and positron impact ionization of atoms. *Atoms*, **9**(2):33, 2021.

[33] O. G. de Lucio, S. Otranto, R. E. Olson, and R. D. DuBois. Triply differential single ionization of argon: Charge effects for positron and electron impact. *Phys. Rev. Lett.*, **104**(16):163201, 2010.

[34] A. Sakaamini, M. Harvey, S. Amami, A. J. Murray, D. Madison, and C. Ning. Differential cross section measurements for ionisation of N_2 in coplanar geometry. *J. Phys. B*, **51**(3):035207, 2018.

[35] K. Bechane, S. Houamer, T. Khatir, A. Tamin, and C. Dal Cappello. Electron-impact ionization of argon in asymmetric kinematics. *Phys. Rev. A*, **109**(1):012812, 2024.

[36] O. Zaidi, A. Mansouri, S. Houamer, A. Tamin, T. Khatir, and C. Dal Cappello. Ionization of argon atom by positron and electron impact. *Eur. Phys. J. D*, **78**(11):65, 2024.

[37] A. Lahmam-Bennani, C. Dupré, and A. Duguet. Electron-impact double ionization of argon studied by double and triple coincidence techniques: The first (e,3e) experiment. *Phys. Rev. Lett.*, **63**:1582–1585, 1989.

[38] F. Catoire, E. M. Staicu-Casagrande, A. Lahmam-Bennani, A. Duguet, A. Naja, X. G. Ren, B. Lohmann, and L. Avaldi. New developments for an electron impact (e,2e)/(e,3e) spectrometer with multiangle collection and multicoincidence detection. *Rev. Sci. Instrum.*, **78**:013108, 2007.

[39] I. Taouil, A. Lahmam-Bennani, A. Duguet, and L. Avaldi. Fully determined (e, 3 e) experiments for the double ionization of helium. *Phys. Rev. Lett.*, **81**:4600, 1998.

[40] A. Lahmam-Bennani, I. Taouil, A. Duguet, M. Lecas, L. Avaldi, and J. Berakdar. Origin of dips and peaks in the absolute fully resolved cross sections for the electron-impact double ionization of he. *Phys. Rev. A*, **59**:3548, 1999.

[41] A. Lahmam-Bennani, A. Duguet, M. N. Gaboriaud, I. Taouil, M. Lecas, A. Kheifets, J. Berakdar, and C. Dal Cappello. Complete experiments for the double ionization of he:(e, 3e) cross sections at 1 kev impact energy and small momentum transfer. *J. Phys. B*, **34**:3073, 2001.

[42] A. Lahmam-Bennani, A. Duguet, C. Dal Cappello, H. Nebdi, and B. Piraux. Importance of non-first-order effects in the (e, 3 e) double ionization of helium. *Phys. Rev. A*, **67**:010701, 2003.

[43] B. El Marji, C. Schröter, A. Duguet, A. Lahmam-Bennani, M. Lecas, and L. Spielberger. Dynamics of the double ionization process from experiments: I. absolute cross sections for argon. *J. Phys. B*, **30**:3677, 1997.

[44] C. C. Jia, A. Lahmam-Bennani, A. Duguet, L. Avaldi, M. Lecas, and C. Dal Cappello. Dynamics of the double ionization process by electron impact: Ar (e, 3e) experiments at low collision energy. *J. Phys. B*, **35**:1103, 2002.

[45] C. C. Jia, A. Lahmam-Bennani, C. Dal Cappello, A. Duguet, and L. Avaldi. Deviations between experimental and theoretical results in ar (e, 3e) double ionization. *J. Phys. B*, **36**:1103, 2003.

[46] A. Naja, E. M. Staicu-Casagrande, X. G. Ren, F. Catoire, A. Lahmam-Bennani, C. Dal Cappello, and C. T. Whelan. An (e, 2e)–(e, 3e) investigation of argon: competition between inner-shell single ionization and direct double ionization processes. *J. Phys. B*, **40**:2871, 2007.

[47] C. Schröter, B. El Marji, A. Lahmam-Bennani, A. Duguet, M. Lecas, and L. Spielberger. Dynamics of the double-ionization process from (e, 3e) experiments: Ii. fivefold differential cross sections for neon. *J. Phys. B*, **31**:131, 1998.

[48] A. Dorn, R. Moshammer, C. D. Schröter, T. J. M. Zouros, W. Schmitt, H. Kollmus, R. Mann, and J. Ullrich. Double ionization of helium by fast electron impact. *Phys. Rev. Lett.*, **82**:2496, 1999.

[49] A. Dorn, A. Kheifets, C. D. Schröter, B. Najjari, C. Höhr, R. Moshammer, and J. Ullrich. Double ionization of helium by electron-impact: complete pictures of the four-body breakup dynamics. *Phys. Rev. Lett.*, **86**:3755, 2001.

[50] M. Dürr, A. Dorn, J. Ullrich, S. P. Cao, A. Czasch, A. Kheifets, J. R. Götz, and J. S. Briggs. (e, 3 e) on helium at low impact energy: The strongly correlated three-electron continuum. *Phys. Rev. Lett.*, **98**:193201, 2007.

[51] A. Lahmam-Bennani, H. Ehrhardt, C. Dupre, and A. Duguet. Identification of mechanisms of electron impact double ionizing collisions by e,(3-1)e experiments. *J. Phys. B*, **24**:3645, 1991.

[52] A. Duguet, C. Dupré, and A. Lahmam-Bennani. Electron impact double ionization of argon studied by coincidence techniques. *J. Phys. B*, **24**:675, 1991.

[53] A. Lahmam-Bennani, H. Ehrhardt, C. Dupré, and A. Duguet. Identification of mechanisms of electron impact double ionizing collisions by e,(3-1)e experiments. *J. Phys. B*, **24**:3645, 1991.

[54] B. El Marji, A. Lahmam-Bennani, A. Duguet, and T. J. Reddish. Electron impact double ionization of argon: angular distributions. *J. Phys. B*, **29**:L157, 1996.

[55] A. Lahmam-Bennani, A. Duguet, and S. Roussin. New measurements of electron impact double ionization of argon. *J. Phys. B*, **35**:L59, 2002.

[56] E. M. Staicu-Casagrande, C. Li, A. Lahmam-Bennani, C. Dal Cappello, M. Schulz, and M. Ciappina. Electron impact double ionization of argon at intermediate energies. *J. Phys. B*, **43**:105201, 2011.

[57] X. G. Ren, A. Dorn, and J. Ullrich. Kinematically complete study of electron impact double ionization of argon. *Phys. Rev. Lett.*, **101**:093201, 2008.

[58] C. Li, A. Lahmam-Bennani, E. M. Staicu-Casagrande, and C. Dal Cappello. Experimental study of electron impact double ionization of argon. *J. Phys. B*, **44**:115201, 2011.

[59] E. M. Staicu-Casagrande, C. Li, A. Lahmam-Bennani, and C. Dal Cappello. New measurements of electron impact double ionization of argon at higher energies. *J. Phys. B*, **47**:115203, 2014.

[60] P. Bolognesi, C. C. Jia, L. Avaldi, A. Lahmam-Bennani, K. A. Kouzakov, and Y. V. Popov. Electron impact double ionization of argon studied with a multi-parameter coincidence technique. *Phys. Rev. A*, **67**:034701, 2003.

[61] R. E. Olson. Collisional mechanisms for single and double ionization of he by protons and antiprotons. *Phys. Rev. A*, **36**(4):1519–1522, 1987.

[62] J. H. McGuire. Double ionization of helium by protons and electrons at high velocities. *Phys. Rev. Lett.*, **49**(17):1153–1156, 1982. Erratum: Phys. Rev. Lett. **51**, 1108 (1983).

[63] F. W. Byron Jr. and Charles J. Joachain. Multiple ionization processes in helium. *Phys. Rev.*, **164**(1):1–14, 1967.

[64] C. Dal Cappello, R. El Mkhanter, and P. A. Hervieux. Mechanisms of double ionization of atoms by electron impact. *Phys. Rev. A*, **57**(R):R693–R696, 1998.

Part I

Theoretical Background on Ionization Processes

Chapter 1

Single Ionization Process

1.1 Introduction

The study of single ionization of atomic [1, 2] and molecular [3, 4] targets by charged particle impact, such as electrons [5], positrons [6], and protons [7], provides valuable insights into the fundamental mechanisms of particle collisions, electron dynamics, and many-body interactions, making it an essential topic in both theoretical and experimental physics. Understanding single ionization helps to improve models of atomic and molecular structures and contributes to applications in fields such as plasma physics, astrophysics, and radiation science.

In a single ionization reaction, a charged particle collides with an atomic or molecular target, causing the ejection of an electron from the target and the scattering of the incident particle. The detection in coincidence of ejected and scattered particles enables the measurement of differential cross sections, thus providing detailed insights into the dynamics of the interaction [8].

This chapter presents the fundamental theoretical framework for the single ionization reaction, focusing on the general kinematic and geometrical conditions required to determine differential cross sections. It also reviews key theoretical models used to describe the process, including the BBK [9], Distorted Wave Born Aproximation (DWBA) [10], and Molecular Three Distorted Waves (M3DW) [11] models, along with the recently developed M3CWZ approach, which incorporates post-collisional interactions and distortion effects in approximative way.

1.2 Description of the Single Ionization Process

The process of single ionization involves the removal, by a projectile electron or positron with momentum $\vec{k}_i$ and energy E_i, of an electron with momentum $\vec{k}_1$ and energy E_1 from a target A (which can be atomic or molecular), leading to the formation of a residual ion A^+, in accordance with the following equation:

$$e_i(\vec{k}_i, E_i) + A \rightarrow A^+ + e_1(\vec{k}_1, E_1) + e_s(\vec{k}_s, E_s) \tag{1.1}$$

When the incident projectile is scattered, it emerges with momentum $\vec{k}_s$ and energy E_s. In the case of electron impact, the electrons emerging in the exit channel after the collision are indistinguishable, making the terms ”scattered” and ”ejected” equivalent. However, when one electron is fast and the other is slow, the faster one is generally referred to as ”scattered,” while the slower one is termed ”ejected”.

In contrast, for positron impact, the issue of indistinguishability does not arise since the projectile and ejected particles are of different nature.

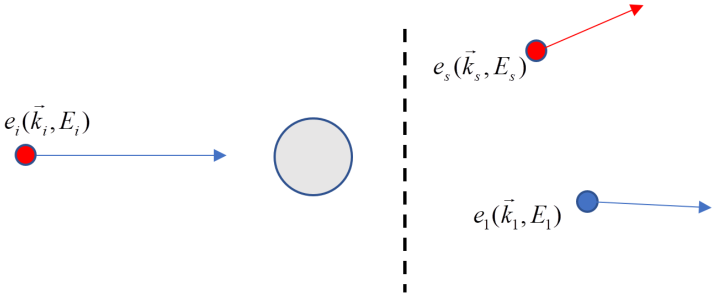

Figure 1.1: The *(e,2e)* Single ionization reaction.

1.2.1 Conservation Laws

This process is ruled by the well known conservation laws of energy and momentum:

$$\begin{aligned} E_i &= E_1 + E_s + I \\ \vec{k}_i &= \vec{k}_1 + \vec{k}_s + \vec{q} \end{aligned} \tag{1.2}$$

I represents the ionization energy required to remove an electron from the target, $\vec{q}$ represents the residual ion momentum. We also define the momentum transfer $\vec{K}$, which represents the difference in the momentum of the incident and scattered electron:

$$\vec{K} = \vec{k}_i - \vec{k}_s \tag{1.3}$$

In atomic units, where

$$a_0 = m_e = \hbar = e = 1,$$

the kinetic energy of the incident, scattered, and ejected particles in the continuum is given by [12]:

$$E_a = \frac{1}{2}k_a^2, \quad a = \{i, s, 1\}. \tag{1.4}$$

1.3 Experiments

Several experimental techniques are available for studying electron and positron impact ionization of atomic and molecular targets.

- **Orsay group Multi-Coincidence Spectrometer:** The experiment uses a specialized electron impact spectrometer to study ionization processes in atoms and molecules. The scattered electron and the ejected electrons are analyzed using three toroidal energy analyzers equipped with position-sensitive detectors. These analyzers collect data on the energy and angles of the outgoing electrons. The system allows measurements of single and double ionization processes with high precision by detecting multiple electrons in coincidence. The experiment records the time and position of detected electrons, reconstructing the dynamics of the ionization event [13].

- **Electron Momentum Spectroscopy (EMS):** Electron Momentum Spectroscopy (EMS) is a technique used to study the electronic structure of atoms and molecules by measuring how electrons are ejected during high-energy collisions. In EMS, a high-energy electron beam (typically in the keV range) collides with a target in a gas state causing its ionization. Both the scattered and ejected electrons are detected in coincidence, and their momenta and energies are measured and analyed to determine the momentum distribution of electrons in the target and reconstruct the binding energy spectra, providing valuable information about orbital wavefunctions, electron correlation, and many-body effects in molecular systems [14].

- **Positron Impact Ionization Experiment:** O. G. de Lucio from the Instituto de Física, Universidad Nacional Autónoma de México (UNAM), Mexico, and R. D. DuBois from the Missouri University of Science and Technology, USA, conducted experiments to study how positrons and electrons ionize atoms and molecules. The experiment used a positron or electron beam, with positrons generated from a sodium-22 radioactive source, moderated by tungsten, and guided through an electrostatic transport system. The beam was directed at a gas jet target inside a vacuum chamber. After collisions, the scattered positrons or electrons were analyzed using a position-sensitive detector (PSD), while ejected electrons and recoil ions were collected using electrostatic analyzers and a channeltron detector. By measuring coincidences between scattered particles and ejected electrons, the team determined the detailed kinematics of ionization events [15].

1.4 Geometrical Configurations and Kinematics

The (e,2e) reaction depends on the electron energies and the value of the momentum transfer $\vec{K}$. The kinematics used to measure the triply differential cross-section (TDCS) are categorized based on different geometries, which can be symmetric or asymmetric, as well as coplanar or non-coplanar. Each geometry is selected according to specific objectives in the study of the ionization process.

1.4.1 Asymmetric Coplanar Geometry:

In the asymmetric coplanar geometry, the incident electron energy E_0 can vary across a wide range: low, intermediate, and high energy regimes. This configuration is characterized by a significant energy difference between the scattered electron E_s and the ejected electron E_1, with the scattered electron generally moving much faster than the ejected one.

The term coplanar refers to the fact that both outgoing electrons remain in the same plane, defined by their momentum vectors $\vec{k_s}$ and $\vec{k_1}$. The azimuthal angle difference between the scattered and ejected electrons, $\phi = \phi_s - \phi_1$, can take values of either 0 or π, indicating that the two electrons are either emitted in the same direction or in opposite directions within the plane. Additionally, the scattering angle θ_s of the incident electron is fixed and kept below $20°$, while the ejection angle θ_1 is allowed to vary.

This specific geometry and kinematic setup are widely used to study ionization dynamics and collisional mechanisms, providing insights into how electrons interact and transfer energy during the ionization process [16]. Furthermore, under particular conditions, this approach has been applied to probe the atomic and molecular structure of the target, as well as to investigate the role of exchange effects between electrons [17, 18]. By carefully analyzing the angular and energy distributions of the scattered and ejected electrons, researchers can gain a deeper understanding of fundamental electron-impact ionization processes.

- **High Energies ($E_i \geq 600$ eV):**At high energies, two regimes can be defined:
  - **Impulsive regime:** Characterized by a large momentum transfer, the collision is primarily binary, involving the incident electron and one of the target electrons. The TDCS exhibits a single peak in the direction of the transferred momentum $\vec{K}$. This regime serves as a useful test for studying the target structure.
  - **Dipole regime:** When the momentum transfer is low, the collision is no longer binary. The TDCS displays two lobes: one in the direction of the transferred momentum $\vec{K}$ and another in the opposite direction $-\vec{K}$. The recoil lobe is associated with the nucleus, which influences the motion of the ejected electron. After the collision, the ejected electron moves with a reduced velocity due to the nucleus's attraction, causing a deviation that redirects its trajectory opposite to the transferred momentum.
- **Intermediate Energies (100 eV $\leq E_i < 600$ eV)** At intermediate energies, the TDCS still exhibits both binary and recoil lobes. However, these lobes are shifted towards larger angles due to post-collisional interactions (PCI), which account for the interaction between the scattered and ejected electrons after the ionization event. To accurately model the TDCS in this regime, these post-collisional effects must be incorporated using appropriate theoretical models.

- **Low Energies (20 eV $\leq E_i < 100$ eV)** In the low-energy range, the TDCS continues to show both binary and recoil peaks, but these are even more displaced toward larger angles. Multiple interaction effects play a crucial role in the collision process at these energies, including:
  - **Post-collisional interactions (PCI):** These interactions occur between the scattered and ejected electrons, influencing the final angular distribution.
  - **Distortion effects:** The trajectory of the ejected electron is modified due to the interaction with the residual ion and the surrounding potential.
  - **Target polarization effects:** The presence of the residual ion alters the interaction potential, affecting the dynamics of the ejected electron.

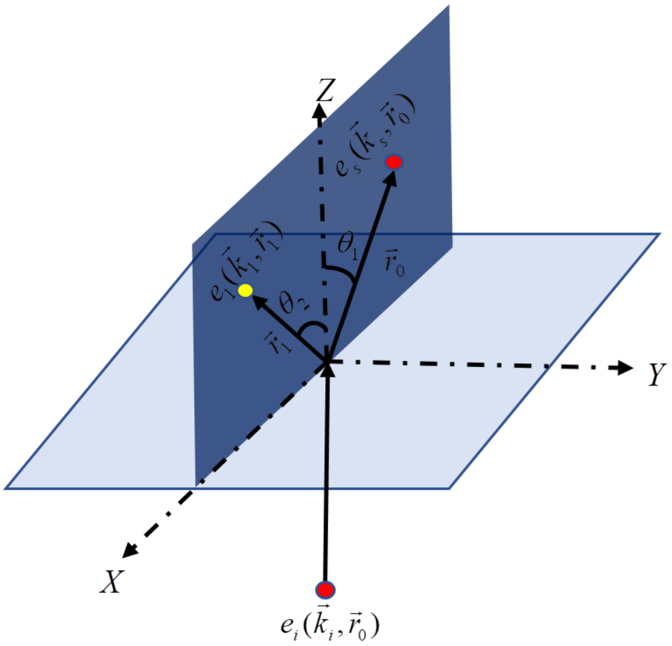

Figure 1.2: Asymmetric coplanar geometry.

1.4.2 Symmetric Geometry:

In this type of experiment, the two electrons in the outgoing channel are detected with equal energies and at symmetric angles relative to the direction of the incident beam. This configuration is particularly useful for investigating the structure of the target as a function of the recoil momentum.

$$E_s = E_1 = \frac{E_0 - E_I}{2} \quad \text{and} \quad \theta_s = \theta_1 = \theta$$

1.4.2.1 Coplanar Symmetric Geometry:

The scattered and ejected electrons lie in the same plane. By applying the conservation of momentum Eq (1.2), it follows that the momentum of the residual ion $\vec{q}$ is aligned with the direction of the incident electron $\vec{k}_i$.

$$q = k_i - 2k_1 \cos\theta$$

The momentum $\vec{q}$ is relatively small for scattering angles θ below 60° and approaches zero at $\theta = 45°$. However, for θ greater than 90°, $\vec{q}$ increases significantly, indicating that the collision involves a large momentum transfer $\vec{K}$. In this geometry, the collision process simplifies to a binary interaction between the incident electron and the target electron.

The final angular distribution of the process provides valuable information about the structure of the target. The exchange factor between the two electrons is not negligible under these conditions; it plays a crucial role in the theoretical description of the collision mechanism.

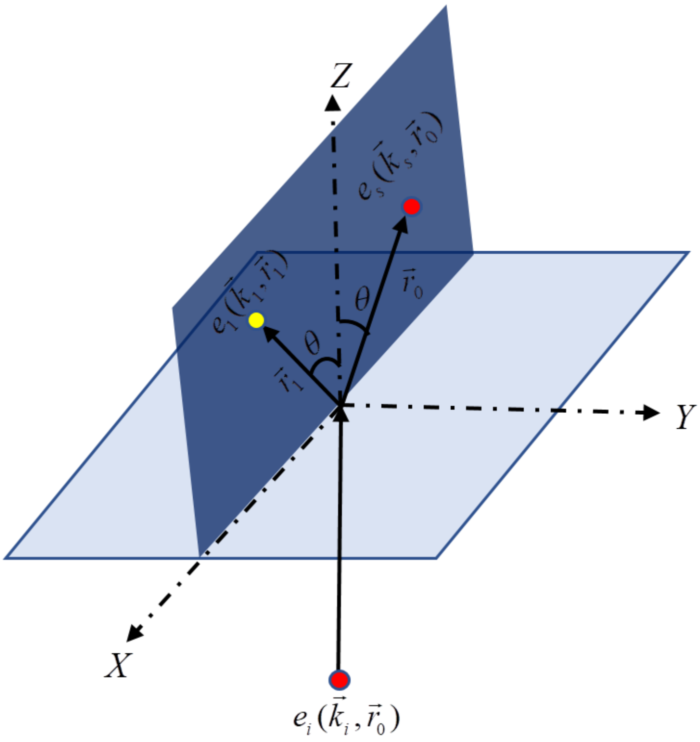

Figure 1.3: Symmetric coplanar geometry.

1.4.2.2 Non Coplanar Symmetric Geometry:

Unlike coplanar geometry, in this case, the electrons do not lie in the same plane. The triple differential cross-section (TDCS) is measured either as a function of the azimuthal angle Φ or as a function of the recoil momentum q of the target. This geometry is often used to study electronic momentum densities, a technique known as Electron Momentum Spectroscopy (EMS) [14]. It is applied under energy conditions ranging from $1-2\ keV$ and serves as a rigorous test for validating the wave functions of the target. From momentum conservation Eq (1.2), we deduce that:

$$q = \left[(2k_s\cos\theta - k_i)^2 + 4k_s^2\sin^2\theta\sin^2\left(\frac{\Phi}{2}\right)\right]^{\frac{1}{2}} \quad \text{where} \quad \Phi = \pi - |\varphi_s - \varphi_1|. \tag{1.5}$$

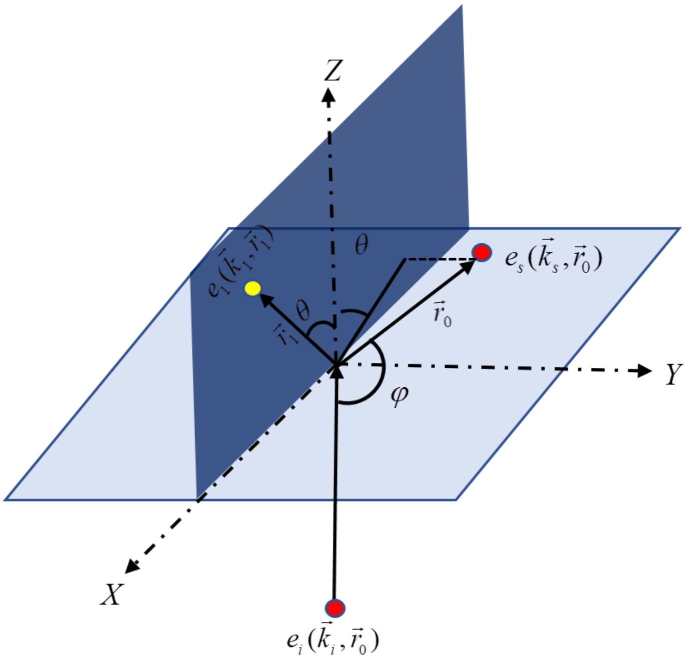

Figure 1.4: Symmetric Non-coplanar geometry.

1.5 Total Cross Section

In a collision experiment, a homogeneous flux F of incident particles, all with the same energy, interacts with target particles N_i in a gaseous state. To simplify the analysis, we assume that the density of target particles and the flux of incident particles are low enough to ensure that each incident particle undergoes only a single collision. This assumption avoids the complexity of multiple-collision effects, which would make both modeling and interpretation significantly more difficult.

A detector is placed at a suitable distance from the interaction region to measure the number N of scattered particles per unit time within a given solid angle element. These measurements are essential for evaluating the efficiency of the collision process. In experimental analysis, this efficiency is quantified using a key parameter known as the cross section.

The cross section represents the probability that an incident particle undergoes a specific interaction, such as ionization. It is proportional to the probability P_{if} of transition from an initial state i to a final state f, as well as to the number of scattered particles N per unit time. Given the flux F of incident particles and measuring both the number of scattered particles N per unit time and the total number of target particles N_f the cross section can be determined using the relation [19]:

$$\sigma = \frac{N}{FN_f} P_{if}$$

The probability P_{if} is directly linked to the scattering amplitude $\langle \psi_f | \hat{T} | \psi_i \rangle$, which characterizes the interaction between the initial and final states of the system. It encapsulates the influence of the scattering potential while ensuring the conservation of energy and momentum. Mathematically, it is expressed as [19]:

$$P_{if} = \frac{(2\pi)^4}{k_i} \delta(E_i - E_f) \delta(k_i - k_f) \left| \langle \psi_f | \hat{T} | \psi_i \rangle \right|^2 F \tag{1.6}$$

1.6 Differential Cross Section

To gain deeper insights into the interaction dynamics, it is often useful to move beyond the total cross section and examine how the scattering events are distributed in terms of energy and angle. While the total cross section provides an overall measure of the likelihood of a collision occurring, it does not reveal details about the direction in which particles are scattered or how their energy is distributed after the interaction. This is where the differential cross section becomes essential as it describes the probability of scattering into a specific solid angle or energy range, offering a more detailed characterization of the underlying physical processes.

1.6.1 Single Differential Cross Section (SDCS)

$$\sigma^{(1)} = \frac{d\sigma}{d\Omega_s} = \frac{(2\pi)^4}{k_i} \int k_s^2 dk_s d\vec{k}_1 \delta(E_i - E_f) \left| T_{if} \right|^2 \tag{1.7}$$

- $d\sigma$ represents an infinitesimal element of the cross section, meaning a small portion of the total probability of an interaction.
- $d\Omega$ is the infinitesimal solid angle element. In other words, it describes a small portion of the angular space where the particle is detected after the collision.

The singly differential cross section thus indicates the probability of detecting a particle in a certain direction after the collision [20].

1.6.2 Double Differential Cross Section (DDCS)

$$\sigma^{(2)} = \frac{d^2\sigma}{d\Omega_s dE_1} = (2\pi)^4 \frac{k_s k_1}{k_i} \int d\Omega_1 \left| T_{if} \right|^2 \tag{1.8}$$

- $d\Omega_s$, as before, is the solid angle element associated with the direction of the scattered particle.
- dE_1 is an infinitesimal energy element of the ejected particle. This cross section thus measures the probability of detecting a particle in a certain direction while having a specific energy [20].

1.6.3 Triple Differential Cross Section (TDCS)

$$\sigma^{(3)} = \frac{d^3\sigma}{d\Omega_s d\Omega_1 dE_1} = (2\pi)^4 \frac{k_s k_1}{k_i} |T_{if}|^2 \tag{1.9}$$

- $d\Omega_s$ represents the solid angle element for the scattered particle.
- $d\Omega_1$ represents the solid angle element for the ejected particle.
- dE_1 is the energy element associated with the ejected particle.

The TDCS accounts for the directions of two detected particles after the collision, as well as the energy of the ejected particle. It measures the probability that the first particle is detected with a specific energy in a certain direction while also considering the direction of the second particle.

1.7 Scattering Amplitude

The goal of the theoretical study of a collision is to model the system's dynamics in the interaction region as precisely as possible to achieve reliable experimental observations. From a quantum mechanics perspective, this is expressed in terms of what is called the scattering amplitude, Within the framework of the first Born approximation the scattering amplitude is given by

$$T_{if} = \langle \Psi_f | V | \Psi_i \rangle \tag{1.10}$$

where:

- Ψ_i is the wave function describing the initial state of the system.
- Ψ_f is the wave function corresponding to the final state after ionization.
- V represents the interaction potential between the projectile and the target.

The description of the initial and final states of the system plays a crutial role in the success of studying the ionization process depends on the theoretical model used and the available wave function of the target.

1.7.1 Description of the Initial State

The ionization process represents theoretically a three body problem which can not be exactly solved. Usually, the initial state of the system before the collision is represented by a product of the wave function of the projectile, ψ_i, and that of the target, Φ, in its fundamental state. Mathematically, this can be expressed as [20]:

$$\Psi_i(\vec{r_0}, \vec{r_1}, ..., \vec{r_n}) = \psi_i(\vec{r_0})\Phi(\vec{r_1}, ..., \vec{r_n}) \tag{1.11}$$

1.7.1.1 Representation of particles in the continuum

When describing the initial state of an ionization process, it is essential to accurately represent the projectile, the scattered particle, and the ejected electron as they evolve in the continuum. The choice of representation depends on the energy of the particles and the nature of their interactions. Several approaches exist, each with specific advantages and limitations in capturing the full complexity of the interaction.

- **Plane Wave (PW)** In this simplest approach, particles are represented as free waves, assuming no interaction with the residual ion or other particles. While computationally convenient, this approximation neglects important effects such as Coulomb attraction or repulsion, making it inaccurate for low-energy collisions where these interactions are significant [21].

- **Coulomb Wave (CW)** This method improves upon the plane wave approximation by incorporating the long-range Coulomb interaction between charged particles. The ejected electron, for example, is described using Coulomb wavefunctions that account for its attraction to the residual ion or repulsion from the scattered projectile. However, this representation do not fully describe more complex short-range interactions [22].

- **Distorted Wave (DW)**

  The distorted wave approach refines the representation by including the effects of the interaction potential throughout the collision process. Instead of treating the particles as fully free or purely Coulombic, it modifies the wavefunctions to account for distortions caused by the potential field of the residual ion. This method provides a more realistic description but comes with increased computational complexity [11].

1.7.1.2 Representation of the Target

A comprehensive description of the target in ionization processes requires addressing the many-body (N-body) problem inherent in atomic and molecular systems. In such systems, multiple interacting electrons contribute to the overall electronic structure, and electron correlation effects are essential for an accurate description.

To capture these correlations, the configuration interaction (CI) method [23] is commonly used for atomic targets, as it accounts for the various possible distributions of electrons among available orbitals, thereby improving upon the single-determinant Hartree–Fock approach [23]. For molecular targets, however, the CI method becomes extremely complex. Although CI wave functions for simple systems such as the hydrogen molecule have been successfully studied [24–26], the computational effort increases drastically with molecular size and complexity, making the application of CI methods to larger molecules practically impossible. Consequently, the Hartree–Fock single-determinant approach remains the most practical choice for describing the wave function of many molecular systems.

The single-particle picture is generally adopted to simplify the problem. This approach is typically combined with the frozen core approximation, which assumes that the inner (core) electrons remain largely unaffected during the interaction, so that only the active electron(s) need to be treated explicitly. This concept of an active electron reduces computational complexity while still capturing the essential physics of the target.

1.7.2 Description of the Final State

The final state of an ionization process represents the system's configuration after the target electron has been ejected. In a theoretical approach, it is crucial to accurately model both the ionized electron, which moves in the continuum, and the incident particle, which continues to evolve after the collision. This description is crucial for predicting the angular distribution of the reaction. Different theoretical approaches have been developed over time to describe the final wavefunction after ionization. These models vary mainly in how they account for interactions between the residual system and the ejected electron, as well as the dynamic correlations between particles.

In the next section, we will introduce some theoretical models relevant to this thesis. These models will later be used to compare with our results.

1.8 Theoretical models

1.8.1 Brauner, Briggs, and Klar Model (BBK)

Brauner, Briggs, and Klar introduced BBK (3C) model to study single ionization of the hydrogen and Helium atoms [9]. This model accounts for electron-electron correlation in the final state by using exact asymptotic description of the final-state wave function, which is defined as the product of three Coulomb waves (hence the alternative name of the model, 3C), the final state is defined as:

$$\Psi_f = \varphi_s(\vec{r_0}, \vec{k_s})\varphi_1(\vec{r_1}, \vec{k_1})C(\alpha_{01}, \vec{r_{01}}, \vec{k_{s1}}) \tag{1.12}$$

φ_s and φ_1 are Coulomb wave functions [X] given by,

$$\varphi_c(\vec{k}, \vec{r}) = \frac{1}{(2\pi)^{\frac{3}{2}}} e^{i\vec{k}\cdot\vec{r}} e^{\frac{-\pi Z}{2k}} {}_1F_1\left(-i\frac{Z}{k}, 1, -i(kr + \vec{k}\cdot\vec{r})\right)\Gamma\left(1 + i\frac{Z}{k}\right) \tag{1.13}$$

whereas the third term, $C(\alpha_{01}, \vec{r_{01}}, \vec{k_{s1}})$, represents the post-collisional interaction (PCI) between the two outgoing electrons.

$$C(\alpha_{01}, \vec{r_{01}}, \vec{k_{s1}}) = \Gamma\left(1 + i\alpha_{01}\right) e^{\frac{\pi\alpha_{01}}{2}} {}_1F_1\left(-i\alpha_{01}, 1, -i(k_{s1}r_{01} + \vec{k_{s1}}\cdot\vec{r_{01}})\right) \tag{1.14}$$

where: $\vec{k_{s1}} = \frac{1}{2}(\vec{k_s} - \vec{k_1})$ and $\alpha_{01} = -\frac{1}{2k_{s1}}$.

1.8.2 Distorted Wave Born Approximation Model (DWBA)

The Distorted Wave Born Approximation (DWBA) is an extension of the Born approximation approach, where the distortion potential that represents the short-range interaction between each incoming (or outgoing) electron and the target in the initial and final states is taken into account. Unlike the BBK model the post-collisional interactions are not treated in an exact manner and are approximated using Ward and Maceak factor [10]:

$$\Psi_f = \chi_s(\vec{r_0}, \vec{k_s})\chi_1(\vec{r_1}, \vec{k_1})C_{e-e} \tag{1.15}$$

$\chi(\vec{k}, \vec{r})$ is the distorted wave function written as:

$$\chi(\vec{k}, \vec{r}) = \frac{4\pi}{(2\pi)^{3/2}} \sum_{l,m} i^l e^{i\delta_l} \frac{F_l(k,r)}{kr} Y^*_{l,m}(\hat{k})\, Y_{l,m}(\hat{r}), \tag{1.16}$$

where δ_l is the total phase shift, and $F_l(k,r)$ is the radial wave function that satisfies the following Schrödinger equation:

$$\left[\frac{d^2}{dr^2} - \frac{l(l+1)}{r^2} - U(r) + k^2\right] F_l(k,r) = 0, \tag{1.17}$$

satisfying the initial conditions:

$$F_l(k,0) = 0 \quad \text{and} \quad F_l(k,r)_{r\to\infty} = \frac{1}{\sqrt{k}} \sin\left(kr - \frac{l\pi}{2} + \delta_l\right) \tag{1.18}$$

C_{e-e} is the Ward and Maceak facor

$$C_{e-e} = N_{ee} |{}_1F_1\left(-i\alpha_{01}, 1, -i(k_{s1}r_{01} + \vec{k_{s1}} \cdot \vec{r_{01}})\right)|^2 \tag{1.19}$$

Where N_{ee} is Gamow factor

$$N_{ee} = |\Gamma\left(1 + i\alpha_{01}\right) e^{\frac{\pi\alpha_{01}}{2}}|^2 \tag{1.20}$$

1.8.3 Molecular Three-body Distorted Waves Model (M3DW)

The Three-body Distorted waves (3DW) model for atoms [11] is an extension of the DWBA method, in which the three electrons are described by distorted waves accounting for electron-target interactions and the inclusion of the post-collisional interactions (PCI) between the two outgoing electrons in the exist channel treated in an exact manner like in BBK model.

Later the model was generalized to study molecular targets M3DW [x],resulting two methods to account for the molecular orientation, which are:

- **M3DW-OAMO Orientation Averaged Molecular Orbitals**: where the orientation dependent molecular orbitals are averaged to obtain a spherically symmetric molecular orbital to use in the cross section calculation. This average is performed once per molecule independent of the kinematics of the collision . The cross section calculations are not very time consuming but show less agreement with the experimental data [27].

- **M3DW-PA Propper Average**: the orientation-dependent cross sections are averaged, this approach is very time consuming but shows much better agreement with the experimental results [28].

1.9 Molecular Three Coulomb Waves with Variable Charge (M3CWZ) Model

The Molecular Three Coulomb Waves with Variable Charge (M3CWZ) model represents a series of improvements in the theoretical modeling of the ionization process. Over the years, various refinements have been made to better account for the interactions involved.

The first step in this development was the BBKDW model, introduced by Chinoune et al. [4], which studied the ionization of atomic targets and the CH_4 molecule in the intermediate energy regime. This model included post collisional interactions in the exit channel, describing the incident electron as a plane wave, the scattered electron as a Coulomb wave, and the ejected electron as a Coulomb wave with a variable charge.

Building on this, Attia et al. [29] extended the variable charge Coulomb wave function to both scattered and ejected electrons, leading to the BBK2DW (or BBK2CWZ) model, which was applied to atomic and molecular ionization studies in the intermediate energy regime.

Later, Bechane et al. [30] introduced the 3CWZ model to investigate the ionization of argon atoms by electron impact, while Zaidi et al. [6], applied it to positron impact in the low-energy regime. The model was further extended to the ionization of neon atoms [31], and successfully applied to the water molecule by Tamin et al. [32],

With these advances, the M3CWZ model has proven effective in describing ionization processes. In this section, we will detail the theoretical foundations of the model.

1.9.1 Concept of Variable charge

The variable charge approximation is a method used to approximately describe the distortion effects that occur during the ionization of an atomic or molecular target by electron or positron impact. It is derived analytically from the spherically averaged potential [20]:

$$U_i(r_1) = \frac{1}{4\pi}\int V_i(\vec{r}_1)d\Omega_1 = \begin{cases} -\frac{Z(r_1)}{r_1} & \text{(for electron)} \\ \frac{Z(r_1)}{r_1} & \text{(for positron)} \end{cases} \tag{1.21}$$

Where V_i is the standard Hartree potential, which is an averaged-field potential used in quantum mechanics to approximate electron (or positron)-nucleus and electron (or positron)-electron interactions in multi-electron systems. In essence, the Hartree potential represents the average electrostatic field that an electron (or positron) experiences due to the combined presence of the nucleus and all other electrons. Instead of explicitly accounting for the complex, individual interactions between each pair of electrons, it is defined for molecules as:

$$V_i\left(\vec{r}_1, \vec{R}_i\right) = \mp \sum_{N=1}^{M} \frac{Z_N}{|\vec{r}_1 - \vec{R}_N|} \pm \sum_{j=1}^{N_0} N_{ij} \int \frac{|\varphi_j(\vec{r})|^2}{|\vec{r} - \vec{r}_1|} d\vec{r} \tag{1.22}$$

The upper (lower) signs refer to the electron and positron interactions, respectively. N_0 is the number of occupied orbitals, N_{ij} the number of electrons in the orbital, M is the number of nuclei, Z_N their charges and R_N their positions with respect to the molecular center of mass. $\varphi_j(\vec{r})$ are the molecular orbitals which describe the target.

1.9.1.1 Boundary Conditions

Entrance Channel: The target is electrically neutral (the number of protons Z_p equals the number of electrons Z_e). At large distances ($r_1 \to \infty$), the projectile perceives no net charge ($Z = 0$). However, as it approaches the target, the effective charge it senses changes due to the varying distribution of the target's charge. At the center of mass ($r_1 = 0$), the projectile perceives the total charge present at that point.

Exit Channel: After ionization, the target loses one electron (resulting in $Z_e - 1$ electrons while still having Z_p protons). Consequently, at large distances ($r_1 \to \infty$) , the ejected and scattered particles experiences an effective charge of $Z = 1$.

1.9.2 Post collisional interaction

In the exit channel, the outgoing particles (electrons and positrons) interact both with each other and with the residual ion. This mutual interaction, known as post-collisional interaction (PCI), is accurately represented by the Coulomb interaction [9]:

$$C(\alpha_{01}, \vec{k}_{s1}, \vec{r}_{01}) = e^{\frac{\pi}{4k_{s1}}} {}_1F_1(-i\alpha_{01}, 1, -i(k_{s1}r_{01} - \vec{k}_{s1} \cdot \vec{r}_{01}))\Gamma\big(1 - \frac{i}{2k_{s1}}\big) \tag{1.23}$$

$$\alpha_{01} = \mp \frac{1}{2k_{s1}} \quad \text{and} \quad \vec{k}_{s1} = \frac{1}{2}(\vec{k_s} - \vec{k_1}) \tag{1.24}$$

${}_1F_1$ is the confluent hyper-geometric function and Γ is the gamma function.α_{01} is the sommerfeld parameter, with signs for electron-electron and positron-electron interactions, respectively.

1.9.3 M3CWZ Approach

In the M3CWZ model, the ionization of a diatomic molecule A by an incident electron or positron is described by the general reaction

$$e^-/e^+(\vec{k}_i, E_i) + A \to A^+ + e^-(\vec{k}_1, E_1) + e^-/e^+(\vec{k}_s, E_s) \tag{1.25}$$

where the incident projectile collides with the molecular target, leading to the ejection of one bound electron and the scattering of the projectile.

The probability of this ionization process is characterized by the triple differential cross section (TDCS), which in the laboratory frame is expressed as

$$\sigma^{(4)} = \frac{d^4\sigma}{d\Omega_{\text{Euler}} d\Omega_s d\Omega_1 dE_1} = (2\pi)^4 \frac{k_s k_1}{k_i} |T_{if}|^2 \tag{1.26}$$

where k_i, k_s, and k_1 are the momenta of the incident, scattered, and ejected particles, respectively, and T_{if} is the scattering amplitude defined as:

$$T_{if} = \langle \Psi_f | V_{\text{int}} | \Psi_i \rangle, \tag{1.27}$$

where Ψ_i and Ψ_f are the initial and final states of the system, and V_{int} represents the interaction potential between the projectile and the active electron, this potential is written as

$$V_{\text{int}} = \begin{cases} -\dfrac{1}{r_0} + \dfrac{1}{r_{01}} & \text{for electron impact} \\ +\dfrac{1}{r_0} - \dfrac{1}{r_{01}} & \text{for positron impact} \end{cases} \tag{1.28}$$

where r_0 and r_{01} denote, respectively, the distances between the projectile and the nucleus, and between the projectile and the bound electron.

The initial state of the system is expressed as

$$\Psi_i = \varphi_c^{Z(+)}(\vec{r}_0, \vec{k}_i)\Phi(\vec{r}_1) \tag{1.29}$$

where $\varphi_c^{Z(+)}$ is the incoming Coulomb wave function with a variable charge $Z(r)$ accounting for distortion effects, and $\Phi(\vec{r}_1)$ is the molecular bound-state wave function.

The incoming Coulomb wave with variable charge is given by [33]:

$$\varphi_c^{Z(+)}(\vec{k}, \vec{r}) = \frac{e^{i\vec{k}\cdot\vec{r}}}{(2\pi)^{3/2}} {}_1F_1\left(i\alpha(r), 1, i(kr - \vec{k}\cdot\vec{r})\right) e^{\frac{\pi\alpha(r)}{2}} \Gamma(1 - i\alpha(r)) \tag{1.30}$$

where $\alpha(r) = \frac{Z(r)}{k}$ is the Sommerfeld parameter.

The final state, describing both the scattered and ejected particles in the continuum, is written as

$$\Psi_f = \varphi_c^{Z(-)}(\vec{r}_0, \vec{k}_s)\varphi_c^{Z(-)}(\vec{r}_1, \vec{k}_1)C(\alpha_{01}, \vec{r}_{01}, \vec{k}_{s1}) \tag{1.31}$$

where $(C(\alpha_{01}, \vec{r}_{01}, \vec{k}_{s1}))$ accounts for the post-collision interaction (PCI) between the outgoing particles. The outgoing Coulomb wave function is defined as [33]:

$$\varphi_c^{Z(-)}(\vec{k}, \vec{r}) = \frac{e^{i\vec{k}\cdot\vec{r}}}{(2\pi)^{3/2}} {}_1F_1\left(-i\alpha(r), 1, -i(kr + \vec{k}\cdot\vec{r})\right) e^{\frac{\pi\alpha(r)}{2}}\Gamma(1 + i\alpha(r)) \tag{1.32}$$

Electron and Positron Impact

For electron impact, the total transition amplitude can be decomposed into direct and exchange components, T_{dir} and T_{exc}, respectively. The corresponding molecular TDCS is:

$$\sigma^{(4)} = \frac{d^4\sigma}{d\Omega_{Euler}d\Omega_1 d\Omega_s dE_1} = (2\pi)^4 \frac{k_1 k_s}{k_i}\left(|T_{dir}|^2 + |T_{exc}|^2 + |T_{dir} - T_{exc}|^2\right) \tag{1.33}$$

For positron impact, exchange effects are absent ($T_{\text{exc}} = 0$), leading to the simplified expression:

$$\sigma^{(4)} = (2\pi)^4 \frac{k_s k_1}{k_i}|T_{\text{dir}}|^2 \tag{1.34}$$

Within the single-particle picture approximation, the direct and exchange amplitudes are written as:

$$\begin{aligned} T_{\text{dir}} &= \left\langle \phi_c^{Z(-)}(\vec{k}_s, \vec{r}_0)\phi_c^{Z(-)}(\vec{k}_1, \vec{r}_1)C(\alpha_{01}, \vec{k}_{s1}, \vec{r}_{01}) \left| \frac{1}{r_{01}} - \frac{1}{r_0} \right| \phi_e^{Z(+)}(\vec{k}_i, \vec{r}_0)\Phi(\vec{r}_1) \right\rangle \\ T_{\text{exc}} &= \left\langle \phi_c^{Z(-)}(\vec{k}_1, \vec{r}_0)\phi_c^{Z(-)}(\vec{k}_s, \vec{r}_1)C(\alpha_{01}, \vec{k}_{s1}, \vec{r}_{01}) \left| \frac{1}{r_{01}} - \frac{1}{r_0} \right| \phi_e^{Z(+)}(\vec{k}_i, \vec{r}_0)\Phi(\vec{r}_1) \right\rangle \end{aligned} \tag{1.35}$$

The evaluation of the transition amplitudes in Eq. (1.35) is performed using the Fourier transform formalism, which allows substantial simplification of the analytical steps [34]. A detailed derivation of one of these matrix elements is provided in Appendix A.

Molecular Averaging and Computational Aspects

Since the molecule can adopt any spatial orientation, the TDCS must be averaged over all Euler angles, giving

$$\sigma_{\text{molecule}} = \frac{1}{8\pi^2} \int \sigma^{(4)} d\Omega_{\text{Euler}} \tag{1.36}$$

Where $d\Omega_{\text{Euler}} = \sin\beta d\alpha d\beta d\gamma$ are the Euler angles defining the molecular orientation. This integration over Euler angles in Eq. (1.36) can be carried out analytically [35, 36]. This combined procedure yields efficient and accurate calculations of the TDCS while significantly reducing computational time.

1.10 Conclusion

This chapter has outlined the basic theoretical framework for understanding single ionization processes by electron and positron impact. We started by discussing the fundamental conservation laws and the experimental setups used to measure ionization events. Different geometries and kinematic conditions were then examined, showing how various experimental configurations help us capture the details of the ionization process.

Next, we explained how electrons in the continuum are represented and how the target wave functions are modeled. Several theoretical models were reviewed, including the BBK, DWBA, and M3DW models, each offering unique insights into projectile-target interactions. Finally, we introduced our developed M3CWZ model. This model takes into account post-collisional interactions and distortion effects in an approximate way by using the concept of a variable charge. By incorporating these additional effects, the M3CWZ model provides an accurate description of the ionization process and improves significantly the computational efficiency.

Bibliography

[1] J. Colgan and M. S. Pindzola. Double- and triple-differential cross sections for the low-energy electron-impact ionization of hydrogen. *Phys. Rev. A*, **74**(1):012713, 2006.

[2] I Bray. Calculation of electron-impact ionization of lithium-like targets. *J. Phys. B*, **28**(7):L247, 1995.

[3] C. Champion, J. Hanssen, and P. A. Hervieux. Electron impact ionization of water molecule. *J. Chem. Phys.*, **117**(1):197–204, 2002.

[4] S. Houamer, M. Chinoune, and C. D. Cappello. Theoretical study of (e, 2e) process of atomic and molecular targets. *Eur. Phys. J. D*, **71**(17):17, 2017.

[5] A. S. Kheifets, A. Naja, E. M. Staicu Casagrande, and A. Lahmam-Bennani. Dwba-g calculations of electron impact ionization of noble gas atoms. *J. Phys. B*, **41**(14), 2008.

[6] O. Zaidi, A. Mansouri, and S. et al. Houamer. Ionization of argon atom by positron and electron impact. *Eur. Phys. J. D*, **78**(140):140, 2024.

[7] Itzik Ben-Itzhak, Eric Wells, D Studanski, Krishnamurthi, Kevin Carnes, and Helge Knudsen. Double and single ionization of hydrogen molecules by fast-proton impact. *J. Phys. B*, **34**:1143, 2001.

[8] D. S. Milne-Brownlie, S. J. Cavanagh, Birgit Lohmann, C. Champion, P. A. Hervieux, and J. Hanssen. Dynamics in electron-impact ionization of h_2O. *Phys. Rev. A*, **69**(3):032701, 2004.

[9] M. Brauner, J. S. Briggs, and H. Klar. Triply-differential cross sections for ionisation of hydrogen atoms by electrons and positrons. *J. Phys. B*, **22**(14):2265, 1989.

[10] A. L. Monzani, L. E. Machado, M. T. Lee, and A. M. Machado. Intermediate-energy electron-impact ionization of molecules. *Phys. Rev. A*, **60**(1):R21–R24, 1999.

[11] Junfang Gao, D. H. Madison, and J. L. Peacher. Distorted wave born and three-body distorted wave born approximation calculations of the fully differential cross section for electron-impact ionization of nitrogen molecules. *J. Chem. Phys.*, **123**(20):204314, 2005.

[12] Nouredine Zettili. *Quantum Mechanics: Concepts and Applications.* John Wiley & Sons, UK, 2009.

[13] F. Catoire, E. M. Staicu-Casagrande, A. Lahmam-Bennani, A. Duguet, A. Naja, X. G. Ren, B. Lohmann, and L. Avaldi. New developments for an electron impact (e,2e)(e,3e) spectrometer with multiangle collection and multicoincidence detection. *Rev. Sci. Instrum.*, **78**(1):013108, 2007.

[14] J.P.D. Cook, R. Pascual, E. Weigold, W. von Niessen, and P. Tomasello. An experimental and theoretical investigation of the valence orbital momentum distributions and binding energy spectra of nitrogen. *Chem. Phys.*, **141**(2):211–224, 1990.

[15] O. G. de Lucio, J. Gavin, and R. D. DuBois. Differential electron emission for single and multiple ionization of argon by 500 ev positrons. *Phys. Rev. Lett.*, **97**(24):243201, 2006.

[16] A. Lahmam-Bennani, H. F. Wellenstein, A. Duguet, and M. Rouault. Absolute triple differential cross sections for the 3p ionisation of argon by electron impact. *J. Phys. B*, **16**(1):121, 1983.

[17] A. Lahmam-Bennani, A. Duguet, and C. Dal Cappello. High momentum range of electron momentum distributions investigated by means of high energy (e, 2e) collisions. *J. Electron Spectrosc. Relat. Phenom.*, **40**(2):141–161, 1986.

[18] L. Avaldi, R. Camilloni, E. Fainelli, and G. Stefani. Electron momentum spectroscopy by asymmetric (e, 2e) collisions belonging to the bethe ridge. *J. Phys. B*, **20**(16):4163, 1987.

[19] Claude Cohen-Tannoudji, Bernard Diu, and Franck Laloë. *Mécanique Quantique II*. Editions Hermann, Paris, 1973.

[20] O. Zaidi. *Description des effets post-collisionnels dans les reaction d'ionisation d'atomes par impact d'electrons et de positrons*. PhD thesis, PhD thesis, University Ferhat Abbas Setif 1, 2025.

[21] M. Chinoune. *PhD thesis*. PhD thesis, University of Science and Technology Houari Boumediene, 2017.

[22] M. Attia. *PhD thesis*. PhD thesis, University Ferhat Abbas Setif 1, 2024.

[23] A. Szabo and N. S. Ostlund. *Modern Quantum Chemistry: Introduction to Advanced Electronic Structure Theory*. Dover Publications, Inc., 1996.

[24] Stanley Hagstrom and Harrison Shull. Single-center wave function for the hydrogen molecule. *J. Chem. Phys.*, **30**(5):1314–1322, 1959.

[25] S. Houamer, A. Mansouri, C. Dal Cappello, A. Lahmam-Bennani, S. Elazzouzi, M. Moulay, and I. Charpentier. Second born approximation for the ionization of h_2 by electron impact. *J. Phys. B*, **36**(14):3009, 2003.

[26] A. Mansouri, C. Dal Cappello, S. Houamer, I. Charpentier, and A. Lahmam-Bennani. Double ionization of h_2 by electron impact: a second born treatment. *J. Phys. B*, **37**(6):1203, 2004.

[27] Junfang Gao, J. L. Peacher, and D. H. Madison. An elementary method for calculating orientation-averaged fully differential electron-impact ionization cross sections of molecules. *J. Chem. Phys.*, **123**(20):204302, 2005.

[28] Hari Chaluvadi, C. G. Ning, and Don H. Madison. Theoretical triple-differential cross sections of a methane molecule by a proper-average method. *Phys. Rev. A*, **89**(6):062712, 2014.

[29] M. Attia, S. Houamer, T. Khatir, K. Bechane, and C. Dal Cappello. Electron impact ionization of atoms and molecules: an improved bbk model. *J. Phys. B*, **56**(7):075201, 2023.

[30] K. Bechane, S. Houamer, T. Khatir, A. Tamin, and C. Dal Cappello. Electron-impact ionization of argon $3p$ in asymmetric kinematics. *Phys. Rev. A*, **109**(1):012812, 2024.

[31] A. Tamin. *PhD thesis.* PhD thesis, University Ferhat Abbas Setif 1, 2025.

[32] A. Tamin, S. Houamer, T. Khatir, L. U. Ancarani, and C. Dal Cappello. Electron-impact ionization of water molecules at low impact energies. *J. Chem. Phys.*, **161**(16):164305, 2024.

[33] L. D. Landau and E. M. Lifshitz. *Quantum Mechanics: Non-Relativistic Theory.* Pergamon Press, Oxford, 1981.

[34] T. Khatir, S. Houamer, and C. Dal Cappello. Theoretical study of the collision dynamics in (e, 2e) reactions. *J. Phys. B*, **52**(24):245201, 2019.

[35] C. Champion, J. Hanssen, and P.-A. Hervieux. Electron impact ionization of water molecule. *J. Chem. Phys.*, **117**:197, 2002.

[36] C. Champion, C. Dal Cappello, S. Houamer, and A. Mansouri. Single ionization of the water molecule by electron impact: Angular distributions at low incident energy. *Phys. Rev. A*, **73**(1):012717, 2006.

Chapter 2

Double Ionization Process

2.1 Introduction

Double ionization is the process in which two electrons are removed from an atom or molecule after an interaction with an incoming particle, such as a photon, electron, or ion. This process is important in atomic and molecular physics because it involves strong electron-electron correlations, making it more complex than single ionization.

In this process, the first electron interacts with the incident particle and is ejected. The second electron is then released in a subsequent interaction, which may proceed through different underlying mechanisms.

Theoretical models aim to describe these mechanisms and predict measurable quantities such as cross sections and angular distributions of the ejected electrons. These models help interpret experimental results and improve our understanding of how electrons interact.

In this chapter, we will discuss double ionization in diatomic molecules. We will cover *(e,3e)* and *(e,3-1e)* experiments, differential cross sections, and key ionization mechanisms such as *Shake-Off* (SO) and *Two-Step* processes (*TS1* and *TS2*). We will also introduce some of the main theoretical models used to describe this phenomenon.

2.2 Description of The Double Ionization Process

We consider the double ionization of an atomic or molecular target B, initially in its ground state, induced by the impact of an incident electron with energy E_i and momentum $\vec{k_i}$. This process, denoted as (e, 3e), results in the scattering of the projectile with energy E_s and momentum $\vec{k_s}$, accompanied by the emission of two electrons with energies and momenta $(E_1, \vec{k_1})$ and $(E_2, \vec{k_2})$, and a residual ion B^{2+}.

$$e_i(\vec{k}_i, E_i) + B \rightarrow B^{2+} + e_s(\vec{k}_s, E_s) + e_1(\vec{k}_1, E_1) + e_s(\vec{k}_2, E_2) \tag{2.1}$$

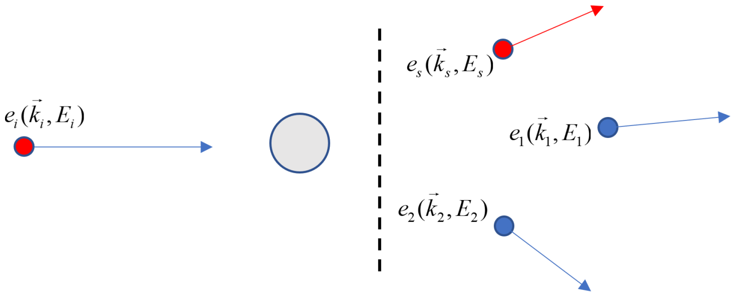

Figure 2.1: The *(e,3e)* Double ionization reaction.

this reaction obeys the following energy and momentum conservation laws:

$$\begin{aligned} E_i &= E_1 + E_2 + E_s + E_{ion} \\ \vec{k}_i &= \vec{k}_1 + \vec{k}_2 + \vec{k}_s + \vec{q} \end{aligned} \tag{2.2}$$

$\vec{q}$ is the recoil momentum of the ionized target; E_{ion} is the energy necessary for ionization, and $\vec{K}$ represents the momentum transfer.

$$\vec{K} = \vec{k}_i - \vec{k}_s \tag{2.3}$$

2.3 Experimental Measurements

The study of electron-impact double ionization relies on advanced experimental techniques capable of resolving the full kinematics of the outgoing particles. Depending on the level of detail and the experimental constraints, several types of coincidence measurements are employed. In this section, we describe two widely used setups: the $(e, 3e)$ and the $(e, 3-1e)$ experiments. Each method provides distinct levels of information on the dynamics of the double ionization process and is suited to different experimental challenges and objectives.

2.3.1 $(e, 3e)$ Experiment

The $(e, 3e)$ experiment offers a complete kinematic characterization of the double ionization process. In this technique, all three outgoing electrons, the scattered projectile and the two electrons ejected from the target, are detected in coincidence. Their energies and emission angles are simultaneously measured, enabling full reconstruction of the final state.

Such measurements provide access to the five-fold differential cross section (5DCS), which gives detailed insights into the energy and angular distributions of the electrons involved in the ionization event. This experimental approach makes it possible to investigate fundamental electron-electron correlation effects and to test theoretical models of double ionization with high precision [1–3].

2.3.2 $(e, 3-1e)$ Experiment

The $(e, 3-1e)$ experiment, in which two out of the three outgoing electrons are detected in coincidence, was developed as an alternative due to the technical challenges and lengthy acquisition times associated with $(e, 3e)$ experiments. These difficulties arise primarily from the small double ionization (DI) cross sections, which are smaller than those for single ionization (SI) processes. As a result, an intermediate coincidence method between the $(e, 2e)$ and $(e, 3e)$ configurations was introduced. The energy of the undetected electron is determined through the energy conservation law (**??**). This technique provides access to the four fold differential cross sections (4DCS), offering valuable insights into the underlying ionization dynamics [4–6].

2.4 Differential Cross Section

2.4.1 Five Fold Differential Cross Section (5DCS)

In $(e, 3e)$ experiments, three electrons are present in the exit channel with nine kinematic parameters. By applying the law of energy conservation before and after the collision, these nine kinematic parameters are reduced to five: the energies of the two ejected electrons E_1, E_2, and the directions of the three outgoing electrons Ω_s, Ω_1, and Ω_2. If these five parameters are determined during DI, the experiment is considered complete: the corresponding cross section is denoted as the Five Fold differential cross section (5DCS) [7].

$$\sigma^{(5)} = \frac{d^5\sigma}{dE_1 dE_2 d\Omega_s d\Omega_1 d\Omega_2} = (2\pi)^4 \frac{k_s k_1 k_2}{k_i} |T_{fi}|^2 \tag{2.4}$$

With $T_{fi} =< \Psi_f|V|\Psi_i >$ is the transition matrix element from the initial state to the final state.

- $\Psi_i = \varphi_i(\vec{r}_0)\Phi(\vec{r}_1, \vec{r}_2)$ is the initial state
- $\Psi_f = \varphi_f(\vec{r}_0)\chi_f(\vec{r}_1, \vec{r}_2)$ is the final state
- V is the interaction potential

Note that the detection of the scattered electron and the two ejected electrons is performed using a coincidence technique (e, 3e), ensuring that the detected electrons originate from the same ionizing event. This experiment provides the most detailed information about the double ionization process and can be considered as a direct test of the different theoretical models describing this process.

2.4.2 Four Fold Differential Cross Section (4DCS)

The four-fold differential cross section (4DCS) for the $(e, 3-1e)$ reaction is obtained by integrating the five-fold differential cross section (5DCS) over the solid angle of the undetected electron. In the case where the scattered electron is not detected, the 4DCS is expressed as [7]:

$$\sigma^{(4)} = \int \sigma^{(5)} d\Omega_s = \frac{d^4\sigma}{dE_1 dE_2 d\Omega_1 d\Omega_2} \tag{2.5}$$

Alternatively, if the scattered electron and one of the ejected electrons are detected, the integration is carried out over Ω_2, resulting in:

$$\sigma^{(4)} = \int \sigma^{(5)} d\Omega_2 = \frac{d^4\sigma}{dE_1 dE_s d\Omega_1 d\Omega_s} \tag{2.6}$$

The 4FDCS is considered incomplete because it describes the angular distribution of one selected pair among the three electrons resulting from a double ionization process.

2.5 Mechanisms of Double Ionization Process

From a phenomenological perspective, based on many-body perturbation theory, three main mechanisms have been proposed to explain the double ionization (DI) of an atomic or molecular target. These mechanisms are known as Shake-Off (SO) and the two-step processes (TS1) and (TS2). The first two mechanisms (SO and TS1) result from a single interaction between the projectile and the target, corresponding to a first-order perturbative process in terms of the projectile's interaction. In contrast, (TS2) is a second-order mechanism with respect to the projectile [8–11].

2.5.1 *Shake-off (SO)*

The Shake-Off (SO) mechanism is a first-order process. It begins with an initial ionization caused by a binary collision between an incident electron and a target electron, leading to the ejection of the latter. The second electron is then ejected as a result of an electronic relaxation triggered by the sudden change in its internal potential, which occurs due to the reduction of the target's charge by one unit [12, 13] .

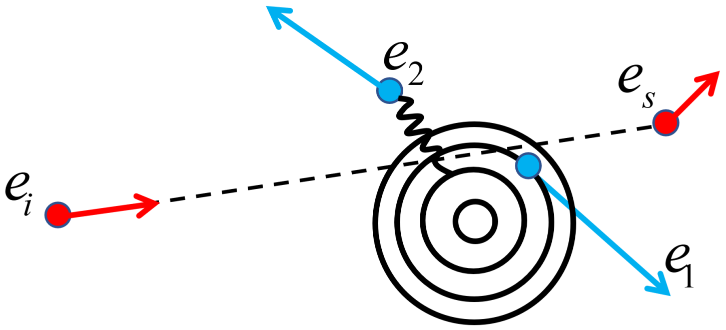

Figure 2.2: The *Shake-Off (SO)* mechanism.

The transition amplitude for this process can be described as a direct transition from the initial to the final state under the influence of the potential V, the expression for this amplitude is given by [11]:

$$f_{SO} = -\frac{1}{2\pi}\left\langle e^{i\vec{k}_s\cdot\vec{r}_0}\chi_f(\vec{k}_1,\vec{k}_2,\vec{r}_1,\vec{r}_2)\right| -\frac{2}{r_0}+\frac{1}{|\vec{r}_0-\vec{r}_1|}+\frac{1}{|\vec{r}_0-\vec{r}_2|}\left| e^{i\vec{k}_i\cdot\vec{r}_0}\Phi(\vec{r}_1,\vec{r}_2)\right\rangle \tag{2.7}$$

2.5.2 *Two Step 1 (TS1)*

The TS1 mechanism, proposed by [14], is a two-step double ionization process that remains first-order in terms of the interaction between the projectile and the target. In the first step, the incident electron ejects a target electron. This ejected electron then collides with a second target electron, leading to its subsequent ejection. This process is therefore referred to as Two-Step 1 (TS1).

The scattering amplitude for this mechanism corresponds to the second term in the Born series expansion and can be expressed in the context of helium double ionization [11].

$$\begin{aligned} f_{TS1} = &-\frac{1}{\pi}\sum_n\int\frac{d\vec{k}_m}{(2\pi)^3[k_i^2-k_m^2-k_s^2-2I_n]}\left\langle\psi_f(\vec{k}_1,\vec{k}_2,\vec{r}_1,\vec{r}_2)\right|\frac{1}{|\vec{r}_1-\vec{r}_2|}\left|\psi_n^+(\vec{k}_m,\vec{r}_1,\vec{r}_2)\right\rangle \\ &\times\left\langle e^{i\vec{k}_s\cdot\vec{r}_0}\psi_n^-(\vec{k}_m,\vec{r}_1,\vec{r}_2)\right| -\frac{2}{r_0}+\frac{1}{|\vec{r}_0-\vec{r}_2|}+\frac{1}{|\vec{r}_0-\vec{r}_2|}\left| e^{i\vec{k}_i\cdot\vec{r}_0}\psi_i(\vec{r}_1,\vec{r}_2)\right\rangle \end{aligned} \tag{2.8}$$

- $\psi_n^\pm$ represent an intermediate state of the first ejected electron, with wave vector $\vec{k}_m$.

- The summation $\sum_n$ runs over all possible intermediate states, where I_n is the energy required to remove an electron from the residual ion in its ground state or an excited state.
- The interaction potential between the incident electron and the two ejected electrons, given by:
$$V = -\frac{2}{r_0} + \frac{1}{|\vec{r}_0 - \vec{r}_1|} + \frac{1}{|\vec{r}_0 - \vec{r}_2|}$$
- Additionally, $V^{'} = \frac{1}{|\vec{r}_1 - \vec{r}_2|}$ represents the interaction potential between the two electrons in the second step of the process.

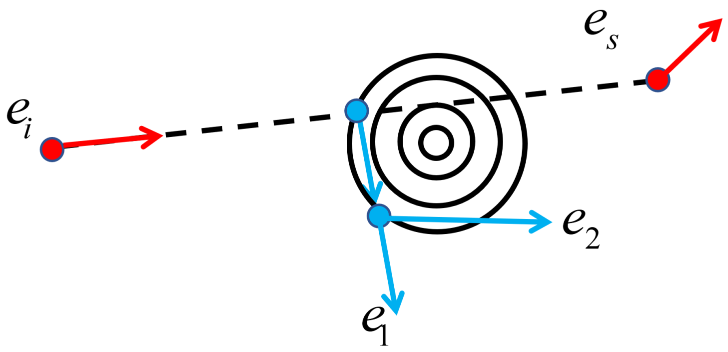

Figure 2.3: The « *Two-Step 1*» *(TS1)* mechanism.

2.5.3 *Two Step 2 (TS2)*

The third mechanism, known as Two-Step 2 (TS2), is a second-order process in the framework of the Born expansion, in which the incident electron interacts twice with the target.

In the first step, the initial interaction of the incident electron leads to the ionization of the target. Subsequently, the incident electron interacts again with the now-ionized target, causing the ejection of a second electron. This TS2 mechanism is illustrated in Figure (2.4).

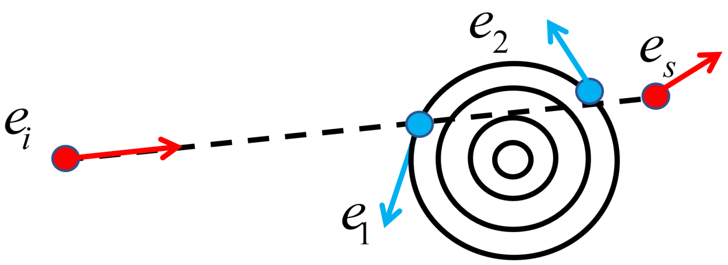

Figure 2.4: The « *Two-Step 2*» *(TS2)* mechanism.

The scattering amplitude associated with this process corresponds to the second term in the Born series expansion and is expressed as follows for the double ionization [11].

$$
\begin{aligned}
f_{TS2} = & -\frac{1}{\pi}\sum_n \int \frac{d\vec{k}_m}{(2\pi)^3[k_i^2 - k_m^2 - k_1^2 - 2I_n]} \left\langle e^{i\vec{k}_s\cdot\vec{r}_0}\psi_f(\vec{k}_2,\vec{r}_2) \middle| \frac{1}{|\vec{r}_0-\vec{r}_2|} \middle| e^{i\vec{k}_m\cdot\vec{r}_0}\psi_n^+(\vec{r}_2) \right\rangle \\
& \times \left\langle e^{i\vec{k}_m\cdot\vec{r}_0}\psi_n^-(\vec{k}_1,\vec{r}_1,\vec{r}_2) \middle| -\frac{2}{r_0} + \frac{1}{|\vec{r}_0-\vec{r}_1|} + \frac{1}{|\vec{r}_0-\vec{r}_2|} \middle| e^{i\vec{k}_i\cdot\vec{r}_0}\psi_i(\vec{r}_1,\vec{r}_2) \right\rangle \\
& -\frac{1}{\pi}\sum_n \int \frac{d\vec{k}_m}{(2\pi)^3[k_i^2 - k_m^2 - k_2^2 - 2I_n]} \left\langle e^{i\vec{k}_s\cdot\vec{r}_0}\psi_f(\vec{k}_1,\vec{r}_1) \middle| \frac{1}{|\vec{r}_0-\vec{r}_1|} \middle| e^{i\vec{k}_m\cdot\vec{r}_0}\psi_n^+(\vec{r}_1) \right\rangle \\
& \times \left\langle e^{i\vec{k}_m\cdot\vec{r}_0}\psi_n^-(\vec{k}_2,\vec{r}_1,\vec{r}_2) \middle| -\frac{2}{r_0} + \frac{1}{|\vec{r}_0-\vec{r}_1|} + \frac{1}{|\vec{r}_0-\vec{r}_2|} \middle| e^{i\vec{k}_i\cdot\vec{r}_0}\psi_i(\vec{r}_1,\vec{r}_2) \right\rangle
\end{aligned}
\tag{2.9}
$$

This equation describes the successive interactions between the incident electron and the two target electrons.

2.6 Theoretical Models

To accurately describe the double ionization process and capture the essential electron-electron correlations, several theoretical models have been developed. These models vary in how they represent the electron wave functions and the treatment of interactions between particles, as well as in the complexity of their mathematical formulations. In the context of the first Born approximation and applied to diatomic molecular targets, the following section details two adopted approaches: the Brauner-Briggs-Klar (BBK) model and the Two-Center Continuum (TCC) model.

2.6.1 Brauner, Briggs, and Klar Model (BBK)

The BBK model, developed by Brauner, Briggs, and Klar, was originally proposed to describe single ionization of hydrogen and helium atoms by electron and positron impact [15–17]. It was later extended to the double ionization of helium by electron [18] and photon impact [19]. The model provides an accurate asymptotic description of the final-state wavefunction, effectively representing electron-electron correlation effects in the double continuum.

At the core of the BBK model is the correlated two-electron continuum wavefunction, constructed as a product of three two-body Coulomb continuum wavefunctions, commonly referred to as the three-Coulomb (3C) wavefunction. Two of these describe the interaction of each ejected electron with the residual ion, while the third accounts for the post-collisional interaction (PCI) between the two ejected electrons.

The final-state wavefunction, symmetrized with respect to electron exchange, is given by:

$$\Phi_f^-(\vec{k}_1, \vec{k}_2 | \vec{r}_1, \vec{r}_2) = \mathcal{P}_{12}\, \psi_c^-(\vec{k}_1; \vec{r}_1)\, \psi_c^-(\vec{k}_2; \vec{r}_2)\, D^-(\alpha_{12}, \vec{k}_{12}; \vec{r}_{12}), \tag{2.10}$$

where $\mathcal{P}_{12} = (1 + P_{21})/\sqrt{2}$ is the exchange operator, and ψ_c^- is the Coulomb continuum wavefunction for a single ejected electron:

$$\psi_c^-(\vec{k}; \vec{r}) = \frac{e^{i\vec{k}\cdot\vec{r}}}{(2\pi)^{3/2}}\, e^{-\pi\alpha/2}\Gamma(1 - i\alpha)\, {}_1F_1(i\alpha, 1, -i(kr + \vec{k}\cdot\vec{r})), \tag{2.11}$$

with $\alpha = Z/k$, and $Z = 2$ is the effective charge seen by the ejected electron.

The post-collisional interaction term is:

$$D^-(\alpha_{12}, \vec{k}_{12}; \vec{r}_{12}) = e^{-\pi\alpha_{12}/2}\Gamma(1 - i\alpha_{12})\, {}_1F_1(i\alpha_{12}, 1, -i(k_{12}r_{12} + \vec{k}_{12}\cdot\vec{r}_{12})), \tag{2.12}$$

where

$$\vec{r}_{12} = \vec{r}_1 - \vec{r}_2, \quad \vec{k}_{12} = \frac{\vec{k}_1 - \vec{k}_2}{2}, \quad \alpha_{12} = \frac{1}{2k_{12}}. \tag{2.13}$$

The BBK model offers a robust and physically realistic description of the double continuum, particularly in representing long-range Coulomb correlations. However, it is computationally demanding due to the complexity of the post-collisional interaction term D^-. To address this, several simplified versions of the model have been proposed, which we will discuss and apply in the following sections.

2.6.2 Two Coulomb Waves with Gamow Factor (2CWG)

This model proposed by Dal Cappello et al. [20] consists of normalizing the function $D^-(\alpha_{12}, \vec{k}_{12}, \vec{r}_{12})$ by arbitrarily imposing the unit value on ${}_1F_1(i\alpha_{12}, 1, -i(k_{12}r_{12} + \vec{k}_{12}\cdot\vec{r}_{12}))$ while retaining the factor $e^{-\frac{\pi\alpha_{12}}{2}}\Gamma(1 - i\alpha_{12})$. This appears sufficient to express the strong correlation between the two ejected electrons in the final state. As a result, the third Coulomb wave describing the post-collisional interaction will be replaced by the so-called Gamow factor $F_G(k_{12})$ and will be written as:

$$F_G(k_{12}) = \left| e^{-\frac{\pi\alpha_{12}}{2}}\Gamma(1 - i\alpha_{12}) \right|^2 = \frac{\pi}{k_{12}\left(e^{\frac{\pi}{k_{12}}} - 1\right)} \tag{II.29}$$

Among the different characteristics provided by this factor, the most significant is the prohibition for electrons to be emitted in the same direction.

This new version of the BBK makes the calculations much simpler and reduces the computation time without losing the physical aspect of the Coulomb repulsion between the two continuum electrons. However, this approximation leads to an underestimation of the amplitude.

2.6.3 Two Coulomb Waves with Ward and Macek Factor (2CWWM)

This model is based on the evaluation of the distortion $D^{-}(\alpha_{12}, \vec{k}_{12}, \vec{r}_{12})$ at a fixed distance different from zero. But setting a point in space that satisfies the appropriate conditions can be a difficult task. Ward and Macek [21] tackled this issue by analyzing asymptotic situations for the problem of two electrons. The distance that Ward and Macek found as a function of the energies between the two electrons was:

$$\bar{x}_{12} = \frac{\pi^2}{16\epsilon}\left[1 + \frac{0.627}{\pi}\sqrt{\epsilon}\ln\epsilon\right]^2 \vec{k}_{12} \tag{II.31}$$

where $\epsilon = (k_1^2 + k_2^2)/2$ is the total kinetic energy of the two electrons. The insertion of this distance in the function $D^{-}(\alpha_{12}, \vec{k}_{12}, \vec{r}_{12})$ gives the factor:

$$F_{WM}(k_{12}) = \frac{\pi}{k_{12}\left(e^{\frac{\pi}{k_{12}}} - 1\right)} \left|{}_1F_1\left(i\alpha_{12}, 1, -2ik_{12}\bar{x}_{12}\right)\right|^2 \tag{II.30}$$

It is noted that this factor depends on the electronic momentum k_{12}, the first term represents the Gamow factor, while the second designates the hypergeometric function evaluated at a fixed distance $\bar{x}_{12}$.

2.6.4 Two-Centre Continuum Model (TCC)

The Two-Centre Continuum (TCC) model is a theoretical framework developed to describe the state of two electrons ejected from a diatomic molecule following impact by a fast incident electron. In the context of $(e, 3e)$ and $(e, 3{-}1e)$ processes, where double ionization occurs, the TCC model accounts for the interaction of the ejected electrons with the Coulomb fields of both nuclei. This dual interaction is especially significant in diatomic molecules such as H_2 and N_2 [22], where the molecular geometry strongly influences the electronic dynamics.

In this approach, the incident and scattered electrons are modeled as plane waves, while the final state of the two slow ejected electrons is constructed using a symmetrized product of modified two-centre Coulomb wavefunctions. These wavefunctions reflect the two-centre character of the molecular potential and ensure the correct asymptotic behavior. In its correlated form, referred to as TCC-C, the model explicitly incorporates electron–electron correlation through a Gamow factor and a confluent hypergeometric function of the inter-electronic distance. This enhancement significantly improves agreement with experimental data, particularly for fully differential cross sections (FDCS).

The correlated two-electron continuum wavefunction is defined as:

$$\chi_f(\vec{r}_1, \vec{r}_2) = \frac{1}{\sqrt{2}} \left[\phi_f(\vec{k}_1, \vec{r}_1, \vec{k}_2, \vec{r}_2) + \phi_f(\vec{k}_1, \vec{r}_2, \vec{k}_2, \vec{r}_1) \right], \tag{2.14}$$

with the correlated product:

$$\phi_f(\vec{k}_1, \vec{r}_1, \vec{k}_2, \vec{r}_2) = T(\vec{k}_1, \vec{r}_1)\, T(\vec{k}_2, \vec{r}_2)\, D^-(\alpha_{12}, \vec{k}_{12}, \vec{r}_{12}), \tag{2.15}$$

where D^- is the electron–electron correlation factor defined in Eq.(2.12), and

$$\vec{r}_{12} = \vec{r}_1 - \vec{r}_2,\ \vec{k}_{12} = \frac{1}{2}(\vec{k}_1 - \vec{k}_2),\ \alpha_{12} = \frac{1}{2k_{12}}$$

Each ejected electron is described by a two-centre Coulomb continuum function:

$$\begin{aligned} T(\vec{k}_i, \vec{r}_j) = {} & \left| \exp\left(-\frac{\pi\alpha_i}{2}\right) \Gamma(1 - i\alpha_i) \right|^2 \frac{e^{i\vec{k}_i \cdot \vec{r}_j}}{(2\pi)^{3/2}} \\ & \times {}_1F_1(i\alpha_i, 1, -i(\vec{k}_i \cdot \vec{r}_{ja} + \vec{k}_i \cdot \vec{r}_{ja}))\, {}_1F_1(i\alpha_i, 1, -i(\vec{k}_i \cdot \vec{r}_{jb} + \vec{k}_i \cdot \vec{r}_{jb})), \end{aligned} \tag{2.16}$$

where

$$Z = 2, \quad \alpha_i = \frac{Z}{k_i}, \quad \vec{r}_{ja} = \vec{r}_j + \frac{\vec{\rho}}{2}, \quad \vec{r}_{jb} = \vec{r}_j - \frac{\vec{\rho}}{2}, \quad i, j = 1, 2. \tag{2.17}$$

This formulation allows the TCC model to accurately represent the dynamics of molecular double ionization, reflecting both the two-centre nature of the potential and the essential correlation effects between the ejected electrons.

2.7 Conclusion

In this chapter, we have presented a detailed theoretical background for the double ionization process induced by electron impact on molecular targets. We discussed the kinematic descriptions, conservation laws, and experimental techniques essential for characterizing these events. The main ionization mechanisms, namely Shake-Off (SO), Two-Step 1 (TS1), and Two-Step 2 (TS2), were introduced, providing insight into the electron correlation dynamics inherent in double ionization. Furthermore, we reviewed several theoretical models, including the BBK and TCC models, which serve as essential tools for interpreting experimental data and predicting cross sections. These models, while differing in complexity, all aim to accurately describe the intricate interactions in the double ionization process. This foundational framework will be critical for the analysis and interpretation of our results in subsequent chapters.

Bibliography

[1] F. Catoire, E. M. Staicu-Casagrande, A. Lahmam-Bennani, A. Duguet, A. Naja, X. G. Ren, B. Lohmann, and L. Avaldi. New developments for an electron impact spectrometer with multiangle collection and multicoincidence detection. *Rev. Sci. Instrum.*, **78**(1):013108, 2007.

[2] A. Lahmam-Bennani, A. Duguet, C. Dal Cappello, H. Nebdi, and B. Piraux. Importance of non-first-order effects in the $(e, 3e)$ double ionization of helium. *Phys. Rev. A*, **67**(1):010701, 2003.

[3] O. Chuluunbaatar, A. A. Gusev, and B. B. Joulakian. The correlated two-centre double continuum and the double ionization of h_2 and n_2 by fast electron impact. *J. Phys. B*, **45**(1):015205, 2012.

[4] C. Li, A. Lahmam-Bennani, E. M. Staicu Casagrande, and C. Dal Cappello. Electron impact double ionization of neon, argon and molecular nitrogen: role of the two-step mechanism. *J. Phys. B*, **44**(11):115201, 2011.

[5] A. Lahmam-Bennani, E. M. Staicu Casagrande, A. Naja, C. Dal Cappello, and P. Bolognesi. Predominance of the second-order, two-step mechanism in the electron impact double ionization of helium at intermediate impact energy. *J. Phys. B*, **43**(10):105201, 2010.

[6] E. M. Staicu Casagrande, C. Li, A. Lahmam-Bennani, C. Dal Cappello, M. Schulz, and M. Ciappina. Experimental and theoretical confirmation of the role of higher order mechanisms in the electron impact double ionization of helium. *J. Phys. B*, **44**(5):055201, 2011.

[7] O. Zaidi. Description des effets post-collisionnels dans les reaction d'ionization d'atomes part impact d'electrons et de positrons. *PhD thesis, Université de Sétif1*, 2025.

[8] R. E. Olson. Collisional mechanisms for single and double ionization of he by protons and antiprotons. *Phys. Rev. A*, **36**(4):1519–1522, 1987.

[9] J. H. McGuire. Double ionization of helium by protons and electrons at high velocities. *Phys. Rev. Lett.*, **49**(17):1153–1156, 1982. Erratum: Phys. Rev. Lett. **51**, 1108 (1983).

[10] F. W. Jr. Byron and C. J. Joachain. Multiple ionization processes in helium. *Phys. Rev.*, **164**(1):1–14, 1967.

[11] C. Dal Cappello, R. El Mkhanter, and P. A. Hervieux. Mechanisms of double ionization of atoms by electron impact. *Phys. Rev. A*, **57**(R):R693–R696, 1998.

[12] R. J. Tweed. Double processes in e——he collisions. *Z. Phys. D*, **23**:309–320, 1992.

[13] A. Duguet and A. Lahmam-Bennani. Double ionization mechanisms from e,(3–1) e and (e, 3 e) experiments. *Z. Phys. D*, **23**:383–388, 1992.

[14] T. A. Carlson and M. O. Krause. Atomic readjustment to vacancies in the k and l shells of argon. *Phys. Rev.*, **137**:A1655–A1662, 1965.

[15] M. Brauner, J. S. Briggs, and H. Klar. Triply-differential cross sections for ionisation of hydrogen atoms by electrons and positrons. *J. Phys. B*, **22**(14):2265–2287, 1989.

[16] B. Brauner, J. S. Briggs, H. Klar, J. T. Broad, T. Rosel, K. Jung, and H. Ehrhardt. Triply differential cross sections for ionization of hydrogen atoms by electrons: the intermediate and threshold energy regions. *J. Phys. B*, **24**(3):657–676, 1991.

[17] M. Brauner, J. S. Briggs, and J. T. Broad. Triply-differential cross sections for ionization of helium by electrons. *J. Phys. B*, **24**(1):287–305, 1991.

[18] B. Joulakian, C. Dal Cappello, and M. Brauner. Double ionization of helium by fast electrons: use of correlated two electron wavefunctions. *J. Phys. B*, **25**(12):2863–2875, 1992.

[19] M. A. Kornberg and J. E. Miraglia. Double photoionization of helium: Use of a correlated two-electron continuum wave function. *Phys. Rev. A*, **48**(5):3714–3724, 1993.

[20] C. Dal Cappello, B. Joulakian, and J. Langlois. Calculations for (e,3e) and (,2e). In *Proc. Int. Symp. on (e,2e) Collisions, Double Photoionization and Related Processes*, volume 3, pages 125–134, 1993. Conference paper.

[21] S. J. Ward and J. H. Macek. Wave functions for continuum states of charged fragments. *Phys. Rev. A*, **49**(2):1049–1054, 1994.

[22] O. Chuluunbaatar, A. A. Gusev, and B. B. Joulakian. The correlated two-centre double continuum and the double ionization of h_2 and n_2 by fast electron impact. *J. Phys. B*, **45**(1):015205, 2012.

Part II

Results and Discussions

Chapter 3

Description of Nitrogen Molecule

3.1 Introduction

The primary objective of this thesis is to investigate the single and double ionization of the nitrogen molecule N_2 induced by electron and positron impact. In order to accurately model and interpret the underlying collision processes, it is essential to first understand the structural and quantum mechanical properties of the N_2 molecule itself.

This chapter provides a detailed theoretical description of the nitrogen molecule, including its molecular structure, symmetries, electronic configuration, and wavefunction construction. These elements serve as the necessary foundation for the subsequent analysis of ionization dynamics presented in later chapters.

3.2 General description of Nitrogen molecule N_2

The nitrogen molecule N_2 is a fundamental chemical substance consisting of two nitrogen nuclei bound together by a shared cloud of electrons. Each nucleus typically contains 7 protons, giving it a nuclear charge of $Z_N = +7$ and, most commonly, 7 neutrons (isotope $^{14}\mathrm{N}$). Therefore, the N_2 molecule contains a total of 14 protons and, in its neutral state, 14 electrons.

The total mass of the N_2 molecule (primarily $^{14}N_2$) is approximately $M_{N_2} \approx 28\ m_p$, with most of it concentrated in the two compact nuclei. These nuclei are separated by an equilibrium internuclear distance of about 1.098 Å, which corresponds to the minimum of the system's potential energy, determined by electromagnetic interactions. The molecule is held together by strong covalent interactions arising from the overlap of atomic electron wavefunctions that form molecular orbitals.

The symmetry properties of the nitrogen molecule (N_2) are considered to be a homonuclear diatomic system with the two nuclei aligned along the z-axis of a Cartesian coordinate system. The origin is conveniently placed at the center of mass of the molecule, which, due to its homo-nuclear nature, coincides with the midpoint of the bond, which is characterized by the following symmetry elements:

- The internuclear (bond) axis, taken as the z-axis, serves as an axis of continuous rotational symmetry (C_∞), reflecting the molecule's cylindrical symmetry.
- Any plane that includes the bond axis (such as the yOz and xOz planes) acts as a vertical reflection plane (σ_v).
- Since N_2 is homonuclear, the center of mass at the bond midpoint also functions as a center of inversion (i), making the molecule centrosymmetric.

The N_2 molecule exhibits discrete, quantized energy levels that originate from three types of motion: electronic, vibrational, and rotational. Electronic energy levels arise from the configuration and excitation of electrons within the molecule. The vibrational motion corresponds to the oscillation of the nuclei about their equilibrium separation, while the rotational motion arises from the overall rotation of the molecule.

3.3 Molecular Hamiltonian and Schrodinger Equation

Considering the system of N_2 composed of two nuclei, labeled A and B, with charges Z_A and Z_B, separated by a distance R. The internuclear vector $\vec{R}$ is given by the difference between the position vectors of each nuclei: $\vec{R} = \vec{R}_A - \vec{R}_B$. As well as N electrons located at positions $\vec{r}_1, \vec{r}_2, \ldots, \vec{r}_N$, with the origin being at the center of mass of the molecule.

Neglecting spin interactions, the time-independent Schrödinger equation for the system is written as

$$H\Psi(\vec{R}, \vec{r}_1, \ldots, \vec{r}_N) = [T_N + T_e + V]\Psi(\vec{R}, \vec{r}_1, \ldots, \vec{r}_N) = E\Psi(\vec{R}, \vec{r}_1, \ldots, \vec{r}_N) \tag{3.1}$$

where $T_N = -\frac{1}{2}\nabla^2_{\vec{R}}$ and $T_e = -\sum_{i=1}^{N} \frac{1}{2}\nabla^2_{\vec{r}_i}$ are the kinetic energy operators of the nuclei and electrons, respectively. V is the total potential energy of the system, i.e., the sum of all Coulomb interactions between all pairs of particles constituting the molecule, expressed as

$$V = -\sum_{i=1}^{N} \left(\frac{Z_A}{|\mathbf{r}_i - \mathbf{R}_A|} + \frac{Z_B}{|\mathbf{r}_i - \mathbf{R}_B|} \right) + \sum_{i<j}^{N} \frac{1}{|\mathbf{r}_i - \mathbf{r}_j|} + \frac{Z_A Z_B}{R}. \tag{3.2}$$

where:

- The 1st term is the electron-nucleus attraction potentials for nuclei A and B, respectively.
- The 2nd term is the electron-electron repulsion potential.
- The 3rd term is the constant nucleus-nucleus repulsion potential.

The Schrödinger equation (3.1) cannot be solved exactly. Therefore, it is necessary to rely on approximation methods to find the best possible solutions for the system.

3.4 Born-Oppenheimer Approximation

The Born-Oppenheimer approximation, introduced in 1927 by Max Born and J. Robert Oppenheimer, is a foundational concept in molecular quantum mechanics. It provides a powerful simplification for solving the Schrödinger equation for molecular systems.

Because nuclei are much heavier than electrons, the dynamics of a molecule can be separated into two distinct parts: the motion of electrons and the motion of nuclei. This separation simplifies the problem significantly and transforms a complex many-body problem into two more manageable steps.

Under the Born-Oppenheimer approximation, the total molecular wave function $\Psi(\vec{r}, \vec{R})$ is written as a product:

$$\Psi(\vec{r}, \vec{R}) = \Psi_n(\vec{R})\Psi_e(\vec{r}; \vec{R}),$$

where $\Psi_e(\vec{r}; \vec{R})$ is the electronic wave function that depends explicitly on $\vec{r}$ and only parametrically on $\vec{R}$, and $\Psi_n(\vec{R})$ is the nuclear wave function.

1. **Solving the Electronic Structure Problem:** For a *fixed* set of nuclear positions $\vec{R}$, the electronic Schrödinger equation is solved, neglecting the kinetic energy of the nuclei. This typically looks like:

$$\left[T_e + V(\vec{r}_1, \ldots, \vec{r}_N, \vec{R})\right] \, \Psi_e(\vec{r}_1, \ldots, \vec{r}_N, ; \vec{R}) = E_e(\vec{R})\Psi_e(\vec{r}_1, \ldots, \vec{r}_N, ; \vec{R})$$

Solving this yields the electronic wave function $\Psi_e(\vec{r};\vec{R})$ and the electronic energy $E_e(\vec{R})$ for that specific nuclear geometry.

2. **Solving the Nuclear Motion Problem:** The electronic energy $E_e(\vec{R})$ obtained from step 1 serves as the potential energy governing the motion of the nuclei. The nuclear Schrödinger equation is then solved using this potential:

$$[T_n + E_e(\vec{R})]\Psi_n(\vec{R}) = E_{\text{total}}\Psi_n(\vec{R})$$

The solution $\Psi_n(\vec{R})$ describes the vibrational and rotational states of the molecule, and E_{total} is the total energy of the system.

3.5 The Construction of Molecular Orbitals

In the formation of the nitrogen molecule (N_2), the atomic orbitals (AOs) of the two nitrogen atoms combine according to the principles of Molecular Orbital (MO) theory. Each nitrogen atom has the electronic configuration $1s^2 2s^2 2p^3$.

According to the Linear Combination of Atomic Orbitals (LCAO) approach, the atomic orbitals overlap to form an equal number of molecular orbitals. Specifically:

- The two $1s$ AOs combine to form a bonding σ_{1s} MO and an antibonding σ^*_{1s} MO.
- The two $2s$ AOs combine to form a bonding σ_{2s} MO and an antibonding σ^*_{2s} MO.
- The six $2p$ AOs (three from each N atom) combine to form six MOs:
  - One bonding σ_{2p} MO (from end-on overlap of $2p_z$ orbitals).
  - Two degenerate bonding π_{2p} MOs (from side-on overlap of $2p_x$ and $2p_y$ orbitals).
  - Two degenerate antibonding π^*_{2p} MOs.
  - One antibonding σ^*_{2p} MO.

Crucially, for N_2, due to s-p mixing, the π_{2p} bonding orbitals are lower in energy than the σ_{2p} bonding orbital.

The 14 electrons (7 from each nitrogen atom) occupy the molecular orbitals in order of increasing energy, following the Pauli exclusion principle and Hund's rule. Since N_2 is a homonuclear molecule, it possesses a center of inversion symmetry; therefore, its molecular orbitals are labeled using the gerade (g) and ungerade (u) notation, indicating symmetry and antisymmetry, respectively, with respect to inversion through the molecular center. Orbitals labeled g remain unchanged upon inversion ($\psi(-\vec{r}) = +\psi(\vec{r})$), whereas those labeled u change sign ($\psi(-\vec{r}) = -\psi(\vec{r})$). The ground-state electronic configuration of N_2 is (see Fig. 3.1):

$$1\sigma_g^2\ 1\sigma_u^2\ 2\sigma_g^2\ 2\sigma_u^2\ 1\pi_u^4\ 3\sigma_g^2. \tag{3.3}$$

Note: $1\pi_u^4$ represents two electrons in each of the degenerate π_{2p_x} and π_{2p_y} orbitals. Excluding the core orbitals ($1\sigma_g^2\,1\sigma_u^2$), the valence configuration ($2\sigma_g^2\,2\sigma_u^2\,1\pi_u^4\,3\sigma_g^2$) contains eight bonding and two antibonding electrons, yielding a bond order of

$$\text{Bond Order} = \frac{N_{\text{bonding}} - N_{\text{antibonding}}}{2} = \frac{8-2}{2} = 3,$$

which corresponds to the well-known triple bond in N_2.

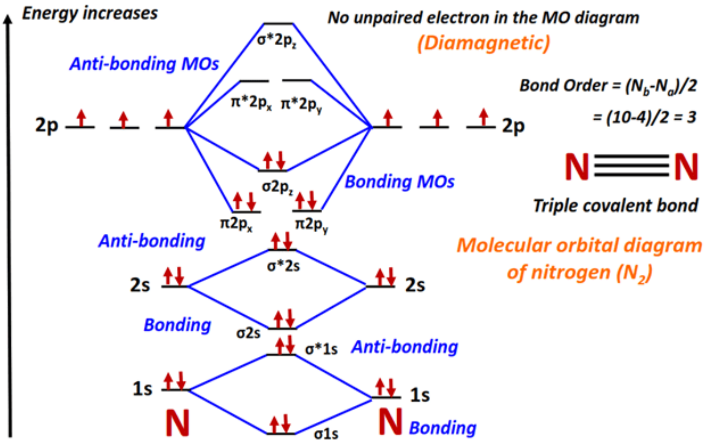

Figure 3.1: Molecular orbitals for Nitrogen (N_2).

3.5.1 Linear Combination of Atomic Orbitals-Molecular orbitals Method (LCAO-MO)

The Linear Combination of Atomic Orbitals-Molecular orbitals Method (LCAO-MO) method is employed to construct the molecule's electrons wave function $\Psi_i(\vec{r})$. It is a variational method that involves expanding the MOs as a linear combination of a limited number of atomic orbitals, known as a basis set (φ_k)

$$\Psi_i(\vec{r}) = \sum_{k=1}^{N_i} a_{ik}\varphi_k(\vec{r}) \tag{II.35}$$

The term corresponding to each atomic orbital basis function (φ_k) in the expansion is multiplied by a weighting coefficient (a_{ik}). Using a larger number of terms (i.e., a larger basis set) generally improves the accuracy of the calculation and brings the calculated energy of the orbital closer to the experimentally determined value.

3.5.2 Atomic Orbital Basis Sets

The atomic orbitals basis functions (φ_k) can be Slater-Type Orbitals, Gaussian-Type Orbitals or Numerical basis functions. The choice of this basis set is very important as it directly affects the quality and accuracy of the calculated molecular wave function. The most frequently utilized basis functions in the construction of these orbitals include:

3.5.2.1 Slater Basis Sets (STO)

Slater-Type Orbitals (STOs) are functions inspired by the exact solutions for hydrogenic atoms. However, compared to true hydrogenic orbitals, the nuclear charge Z is replaced by an effective nuclear charge α (where typically $\alpha < Z$) to account for electron screening. In spherical coordinates (r, θ, ϕ), they have the general form:

$$\phi^{\mathrm{S}}_{n,l,m}(r,\theta,\phi) = N r^{(n-1)} e^{-\alpha r} Y_{lm}(\theta,\phi) \tag{II.36}$$

Where:

- $N = \frac{(2\alpha)^{n+\frac{1}{2}}}{\sqrt{(2n)!}}$ is a normalization factor.
- α is the orbital exponent, often treated as a variational parameter.
- n, l, m are the usual quantum numbers known in atomic physics.
- $Y_{lm}(\theta, \phi)$ are the spherical harmonics.

The advantage of these single-centered STOs in atomic and molecular physics lies in their ability to enable analytical evaluation of the differential cross sections.

3.5.2.2 Gaussian Basis Sets (GTO)

Gaussian-Type Orbitals (GTOs) are widely used in quantum chemistry software packages. They offer faster convergence compared to Slater-Type Orbitals (STOs) and are expressed as:

$$\phi^{\mathrm{G}}_{P}(r,\theta,\phi) = N\, r^{(2n-2-l)} e^{-\alpha r^2} Y_{lm}(\theta,\phi) \tag{II.37}$$

where:

- N is a normalization constant.
- α is the orbital exponent, treated as a variational parameter.
- n, l, m are the principal, angular momentum, and magnetic quantum numbers, respectively.
- $Y_{lm}(\theta, \phi)$ are the spherical harmonics.

This type of function is particularly convenient for purely numerical calculations due to the simplicity of evaluating products and integrals of Gaussian functions.

3.6 Construction of Nitrogen Molecule Wave function

The construction of the initial state wavefunction for the N_2 molecule began with a standard quantum chemical calculation at the Hartree-Fock (HF) self-consistent field level. This calculation utilized the large and flexible augmented, correlation-consistent, quadruple-zeta (aug-cc-pVQZ) basis set, composed of Gaussian-Type Orbitals (GTOs). Executed with the Gaussian 03 software package [1] at the fixed experimental geometry, this initial step produced the conventional multi-center molecular orbitals (MOs) via the Linear Combination of Atomic Orbitals (LCAO) approach. A crucial subsequent step for the scattering formalism involved converting these delocalized, multi-center MOs into a single-center expansion (SCE), employing methods described in previous studies [2, 3]. Although originating from a GTO-based computation, the final working representation of the specific single-center Molecular Orbitals was expressed as a linear combination of Slater-Type Functions (STOs) (further details in reference [4, 5]), written as follows: as .

$$\begin{aligned} \varphi_j(\vec{r}) &= \sum_{k=1}^{N_j} a_{jk} R^{\alpha_{jk}}_{n_{jk} l_{jk}}(r) Y_{l_{jk} m_{jk}}(\Omega) \\ R^{\alpha_{jk}}_{n_{jk} l_{jk}}(r) &= r^{n_{jk}-1} \exp(-\alpha_{jk} r) \end{aligned} \tag{3.4}$$

The following tables show the single center Slater-Type Function expansions for the N_2 valence molecular orbitals: $2\sigma_g$ (table 3.1), $2\sigma_u$ (table 3.2), $3\sigma_g$ (table 3.3), and $1\pi_u$ (table 3.4), obtained using the method described above.

Table 3.1: Slater Type Orbital contributions to the $2\sigma_g$ molecular orbital of N_2.

n	l	m	$2\sigma_g$	
			α	a
1	0	0	9.77984531	2.81429939
2	0	0	1.92926356	4.81208629
3	0	0	6.18681500	50.05765810
3	2	0	2.22208532	24.10688610
4	2	0	2.82640137	-176.735249
5	2	0	2794.75304	-1435.87524
6	2	0	6.85332419	2855.131960
7	2	0	3.76875326	73.49167090
8	2	0	5.84895716	1206.33016
9	2	0	7.98416357	-1478.14459
5	4	0	4.96234226	218.7195140
6	4	0	4.83384734	-2085.54992
7	4	0	6.65495477	7101.259230
8	4	0	5.53463280	2153.084170
9	4	0	2652.92595	5047.056430
10	4	0	7.17480781	-14257.2770
11	4	0	7.83529313	20419.85950
7	6	0	5.48612866	-170.821448
8	6	0	4.52950867	583.280194
9	6	0	17164.4743	4035.99953
10	6	0	5.16456754	-845.327976
11	6	0	9.06478977	-16290.4840
12	6	0	5.81139749	319.230396
9	8	0	6.52725644	887.0807200
10	8	0	13.6737104	-49.3299082
11	8	0	9.37767128	-11617.5139
12	8	0	7.61608403	-808.675759

Table 3.2: Slater Type Orbital contributions to the $2\sigma_u$ molecular orbital of N_2.

n	l	m	$2\sigma_u$	
			α	a
2	1	0	1.43849226	17.012082
3	1	0	2.81609837	-249.470865
4	1	0	5.86281604	1129.853620
5	1	0	4.01209113	439.193313
6	1	0	2.15106265	-0.73906265
4	3	0	2.28164978	1.10103508
5	3	0	4.99150516	-638.197761
6	3	0	5.95471421	4262.62694
7	3	0	6.94995977	-7339.1812
8	3	0	5783.72404	3800.98996
6	5	0	4.66626940	-1441.05936
7	5	0	8.05339638	10560.77580
8	5	0	5.42174521	3046.09258
9	5	0	1787.32625	4953.70034
10	5	0	6.20124571	-1704.10996
8	7	0	4.66496849	718.5806
9	7	0	5.15606393	-2404.75187
10	7	0	337.158269	1082.88492
11	7	0	6.53731218	6402.29177
12	7	0	6.96971175	-2973.07139
13	7	0	6.23459097	249.170464

Table 3.3: Slater Type Orbital contributions to the $3\sigma_g$ molecular orbital of N_2.

n	l	m	$3\sigma_g$	
			α	a
1	0	0	10.1276241	-0.10344542
2	0	0	10.2718374	-29.1389776
3	0	0	1.82430732	-16.9262459
4	0	0	1.95456966	8.17812708
5	0	0	3.38166581	38.4760416
3	2	0	1.35934321	0.27249854
4	2	0	3.49716417	-142.970191
5	2	0	6.63391233	1090.61543
6	2	0	6.05748994	-122.367679
7	2	0	4.43912862	605.493439
8	2	0	4.81930956	-499.911138
5	4	0	5.11682883	-127.216131
6	4	0	8.66361037	1100.69342
7	4	0	4.28206877	115.15899
8	4	0	4.66170074	-110.57076
9	4	0	309.916138	-87.9511709
10	4	0	233.986702	-38.9423390
7	6	0	9.04221801	1317.66684
8	6	0	9.12922698	-2743.27941
9	6	0	7.256453	147.551805
10	6	0	658.071799	885.032137
9	8	0	2.16125345	1.08575573
10	8	0	2.41501217	-3.91045322
11	8	0	3.53751433	5.21578763
12	8	0	2.75070237	1.43951056
13	8	0	2.91000367	-0.34932313

Table 3.4: Slater Type Orbital contributions to the $1\pi_u$ molecular orbital of N_2.

n	l	m	$1\pi_u$	
			α	a
2	1	1	5.70823623	-1.64549523
2	1	-1	5.70823623	1.64549523
3	1	1	1.60776749	-0.78024047
3	1	-1	1.60776749	0.78024047
4	1	1	3.38873270	-9.26959523
4	1	-1	3.38873270	9.26959523
4	3	1	2.49335380	-4.63244487
4	3	-1	2.49335380	4.63244487
5	3	1	3.11229164	12.7476209
5	3	-1	3.11229164	-12.7476209
6	3	1	5.13843605	47.3117996
6	3	-1	5.13843605	-47.3117996
7	3	1	4.62818504	-174.517096
7	3	-1	4.62818504	174.517096
8	3	1	5.13216696	177.954584
8	3	-1	5.13216696	-177.954584
6	5	1	4.10864939	-119.767610
6	5	-1	4.10864939	119.767610
7	5	1	7.18999394	850.901069
7	5	-1	7.18999394	-850.901069
8	5	1	4.61761964	53.44504640
8	5	-1	4.61761964	-53.44504640
9	5	1	6.35725543	415.8064840
9	5	-1	6.35725543	-415.8064840
10	5	1	226.470067	-237.663417
10	5	-1	226.470067	237.663417
8	7	1	5.58860747	138.502089
8	7	-1	5.58860747	-138.502089
9	7	1	6.15706624	-517.215928
9	7	-1	6.15706624	517.215928
10	7	1	6.69787362	440.683957
10	7	-1	6.69787362	-440.683957

3.7 Laboratory Frame and Molecular Frame - Euler Angles

A collision system is typically described in the laboratory frame (OXYZ). However, the molecular orbitals wave functions, which contribute to the transition amplitude, are usually provided in the molecule's mass center frame ($Oxyz$). The transformation between these two reference frames is accomplished using the Euler angles (α, β, γ). These angles relate the laboratory frame to the molecule-fixed frame via a composite rotation, denoted $\mathcal{R}(\alpha, \beta, \gamma)$. This rotation can be expressed as a sequence of three elementary rotations (using the $z-y-z$ convention often employed in molecular physics):

$$\mathcal{R}(\alpha, \beta, \gamma) = \mathcal{R}_z(\gamma)\mathcal{R}_y(\beta)\mathcal{R}_z(\alpha)$$

where the individual rotation matrices are:

$$\mathcal{R}_z(\alpha) = \begin{bmatrix} \cos\alpha & -\sin\alpha & 0 \\ \sin\alpha & \cos\alpha & 0 \\ 0 & 0 & 1 \end{bmatrix} \mathcal{R}_y(\beta) = \begin{bmatrix} \cos\beta & 0 & \sin\beta \\ 0 & 1 & 0 \\ -\sin\beta & 0 & \cos\beta \end{bmatrix} \mathcal{R}_z(\gamma) = \begin{bmatrix} \cos\gamma & -\sin\gamma & 0 \\ \sin\gamma & \cos\gamma & 0 \\ 0 & 0 & 1 \end{bmatrix}$$

In the laboratory frame (OXYZ), the wave function of the molecule is written as a function of the Euler angles as:

$$\Psi_{i(\mathrm{lab})}(\vec{r}, \alpha, \beta, \gamma) = \sum_{k=1}^{N_i} a_{ik} R^{\xi}_{n_{ik}}(r) \sum_{\mu=-l_{ik}}^{l_{ik}} D^{l_{ik}}_{\mu,m_{ik}}(\alpha, \beta, \gamma) Y_{l_{ik},\mu_{ik}}(\hat{r}) \tag{3.5}$$

The evaluation of the differential cross sections require an averaging over all possible orientations of the molecule, and it can be carried out analytically thanks to the following property of the rotation matrix $D^l_{\mu,m}(\alpha, \beta, \gamma)$ [6]

$$\frac{1}{8\pi^2} \int d\Omega_{\mathrm{Euler}} D^l_{\mu,m}(\alpha, \beta, \gamma) D^{l^*}_{\mu,m}(\alpha, \beta, \gamma) = \frac{1}{2l+1} \delta_{ll'} \delta_{mm'} \delta_{\mu\mu'} \tag{3.6}$$

3.8 Summary

In this chapter, we have presented the fundamental properties and quantum mechanical description of the nitrogen molecule (N_2), which serves as the target system in this thesis. We discussed its structural and symmetry characteristics, constructed its molecular orbitals using the LCAO-MO method, and detailed the computational approaches used to obtain accurate wavefunctions. These elements form the theoretical basis required for analyzing electron and positron impact ionization processes, which are the central focus of the following chapters.

Bibliography

[1] M. J. et al. Frisch. *Gaussian 03, Revision B.05.* Gaussian, Inc., Wallingford, CT, 2004.

[2] H. Hafied, A. Eschenbrenner, C. Champion, M. F. Ruiz-Lopez, C. Dal Cappello, I. Charpentier, and P. A. Hervieux. Electron-impact ionization of the water molecule: A theoretical study of the triple differential cross sections. *Chem. Phys. Lett.*, **439**(1-3):55–59, 2007.

[3] K. Kaufmann, W. Baumeister, and M. Jungen. Universal Gaussian basis sets for an optimum representation of Rydberg and continuum wavefunctions. *J. Phys. B: At. Mol. Opt. Phys.*, **22**(14):2223–2240, 1989.

[4] C. Dal Cappello, Z. Rezkallah, S. Houamer, I. Charpentier, P. A. Hervieux, M. F. Ruiz-Lopez, R. Dey, and A. C. Roy. Double ionization of N_2 by electron impact. *Phys. Rev. A*, **84**(3):032711, 2011.

[5] P. Lamy, C. Dal Cappello, I. Charpentier, M. F. Ruiz-Lopez, and P. A. Hervieux. The second Born approximation for the double ionization of N_2 by electron impact. *J. Phys. B*, **49**(13):135203, 2016.

[6] Nouredine Zettili. *Quantum Mechanics: Concepts and Applications.* Wiley, Chichester, UK, 2nd edition, 2009.

Chapter 4

Single Ionization of Molecular Nitrogen by Electron and Positron Impact

4.1 Introduction

Theoretical investigation of the triple differential cross section (TDCS) in the nitrogen molecule ionization by electron and positron impact [1] is performed using the M3CWZ model for both the inner $2\sigma_g$ and the outer $2\sigma_u$, $1\pi_u$, and $3\sigma_g$ orbitals of the molecule at intermediate impact energies (up to 700 eV) as well as at a lower impact energy of 250 eV. This study aims to provide a detailed description of the ionization dynamics over a wide range of kinematical conditions, thereby offering insight into the influence of projectile type on the observed cross sections.

In this chapter, we present and discuss the results of our calculations in detail, highlighting the trends revealed by the M3CWZ model. The TDCS calculations are systematically compared with previous theoretical approaches and with available experimental data obtained in asymmetric geometries at both large and low recoil momenta, enabling a critical assessment of the model and contributing to a broader understanding of electron– and positron–molecule collision processes.

---

[1] Part of this chapter (in particular section II.3) is reproduced from: S. Mekhalfa, S. Houamer, A. Mansouri, I. Khiat, A. Tamin, C. Dal Cappello, and P.-A. Hervieux. Theoretical investigation of the triple differential cross section in the nitrogen molecule ionization by electron and positron impact. Journal of Electron Spectroscopy and Related Phenomena, **281**:147545, 2025, with the permission of ELSEVIER Publishing.

4.2 Application of M3CWZ model to the ionization of Nitrogen molecule

The positron (electron) impact ionization of nitrogen molecule, in its ground state, is expressed as:

$$e^-/e^+(\vec{k}_i, E_i) + N_2 \to N_2^+ + e_1^-(\vec{k}_1, E_1) + e^-/e^+(\vec{k}_s, E_s).$$

The triple differential cross section (TDCS) is calculated using the M3CWZ model, where all continuum wave functions are described by Coulomb waves with variable charges. We study complete experiments in which an incident particle (electron or positron) with momentum $\vec{k}_i$ and energy E_i is scattered with momentum $\vec{k}_s$ and energy E_s, and an ejected electron with momentum $\vec{k}_1$ and energy E_1 is detected in coincidence. The energies and momenta of all particles satisfy the laws of energy and momentum conservation.

The variable charge $Z(r)$ is evaluated by using the spherically averaged potential:

$$U(\vec{r}_1) = \frac{1}{4\pi}\int V(\vec{r}_1, \vec{R}_i)\, d\Omega_1 = \mp\frac{Z(\vec{r}_1)}{r_1} \tag{4.1}$$

where $V(\vec{r}_1, \vec{R}_i)$ is the standard Hartree potential defined for molecules by:

$$V_i(\vec{r}_1, \vec{R}_i) = \mp\sum_{N=1}^{M}\frac{Z_N}{|\vec{r}_1 - \vec{R}_N|} \pm \sum_{j=1}^{N_0} N_{ij}\int\frac{|\phi_j(\vec{r})|^2}{|\vec{r} - \vec{r}_1|}\, d\vec{r} \tag{4.2}$$

The upper (lower) signs refer to the electron (positron) impact reactions respectively. N_0 is the number of occupied orbitals, N_{ij} is so that $N_{ij} = 2$ if $i \neq j$ and $N_{ij} = 1$ if ij, M is the number of nuclei, Z_N their charges and R_N their positions with respect to the molecular center of mass. $\phi_j(\vec{r})$ are the set of molecular orbitals which describe the target.

The ground state configuration of nitrogen molecule is given by:

$$1\sigma_g^2\ 1\sigma_u^2\ 2\sigma_g^2\ 2\sigma_u^2\ 1\pi_u^4\ 3\sigma_g^2 \tag{4.3}$$

For N_2, the molecular orbitals are centered in the middle of the inter-nuclear axis, Eq. (4.2) becomes hence:

$$V_i(\vec{r}_1, \vec{R}) = \mp\frac{7}{|\vec{r}_1 - \vec{R}/2|} \mp \frac{7}{|\vec{r}_1 + \vec{R}/2|} \pm \sum_{j=1}^{14} N_{ij}\int\frac{|\phi_j(\vec{r})|^2}{|\vec{r} - \vec{r}_1|}\, d\vec{r} \tag{4.4}$$

In the present investigation we consider that the inner orbitals $1\sigma_g$ and $1\sigma_u$ are strongly bound to the core and can be considered as part of the core. As a result, only the orbitals $2\sigma_g$, $2\sigma_u$, $1\pi_u$, and $3\sigma_g$ are considered to calculate of $V_i(\vec{r}_1, \vec{R})$, this leads therefore to the following expression:

$$V_i(\vec{r}_1, \vec{R}) = \mp \frac{5}{|\vec{r}_1 - \vec{R}/2|} \mp \frac{5}{|\vec{r}_1 + \vec{R}/2|} \pm \sum_{j=1}^{10} N_{ij} \int \frac{|\phi_j(\vec{r})|^2}{|\vec{r} - \vec{r}_1|} d\vec{r} \tag{4.5}$$

After averaging over $d\Omega_1$, the spherical potential $U(\mathbf{r})$ given by Eq. (4.1), is then written as:

$$U_i(\vec{r}_1) = \mp 10 \begin{cases} 1/r_1 & \text{if } r_1 > R_1 \\ 1/R_1 & \text{if } r_1 < R_1 \end{cases} \pm \frac{1}{4\pi} \int \left(\sum_{j=1}^{10} N_{ij} \int \frac{|\phi_j(\vec{r})|^2}{|\vec{r} - \vec{r}_1|} d\vec{r} \right) d\Omega_1 = \mp \frac{Z(r_1)}{r_1} \tag{4.6}$$

Where $R_1 = R/2 = 1.06\ a.u.$, R is the bond length of the molecule. $\phi_j(\vec{r})$ are the single center molecular orbitals (See Section 3.6)

The variable charge $Z(r)$ is finally written in an analytical form, as a series expansion, enabling the calculation of the matrix elements in a very convenient way.

Figure 4.1 presents the variable charge functions $Z_i(r)$, $Z_1(r)$, and $Z_2(r)$ as functions of the distance r for the $3\sigma_g$ orbital corresponding to the incident, scattered, and ejected particles, respectively. In our model, the molecular wave functions are centered at the midpoint of the internuclear axis. The ejected and scattered electrons experience an effective charge of $Z = 0$ at the center of the target and $Z = 1$ at large distances, while the incident electron (or positron) feels a charge of $Z = 0$ both at the center and asymptotically. As shown in the figure, the asymptotic values of $Z(r)$ are reached rapidly, around $r = 3$ a.u.. The function $Z(r)$ increases from $r = 0$ to a maximum at $r = R_1$, then decreases asymptotically to $Z = 0$ or $Z = 1$. A sharp peak appears at $r = R_1 = R/2$, where R is the bond length defined earlier. This sharp peak is a distinctive feature of molecular targets and is not observed for atomic ones [1,2].

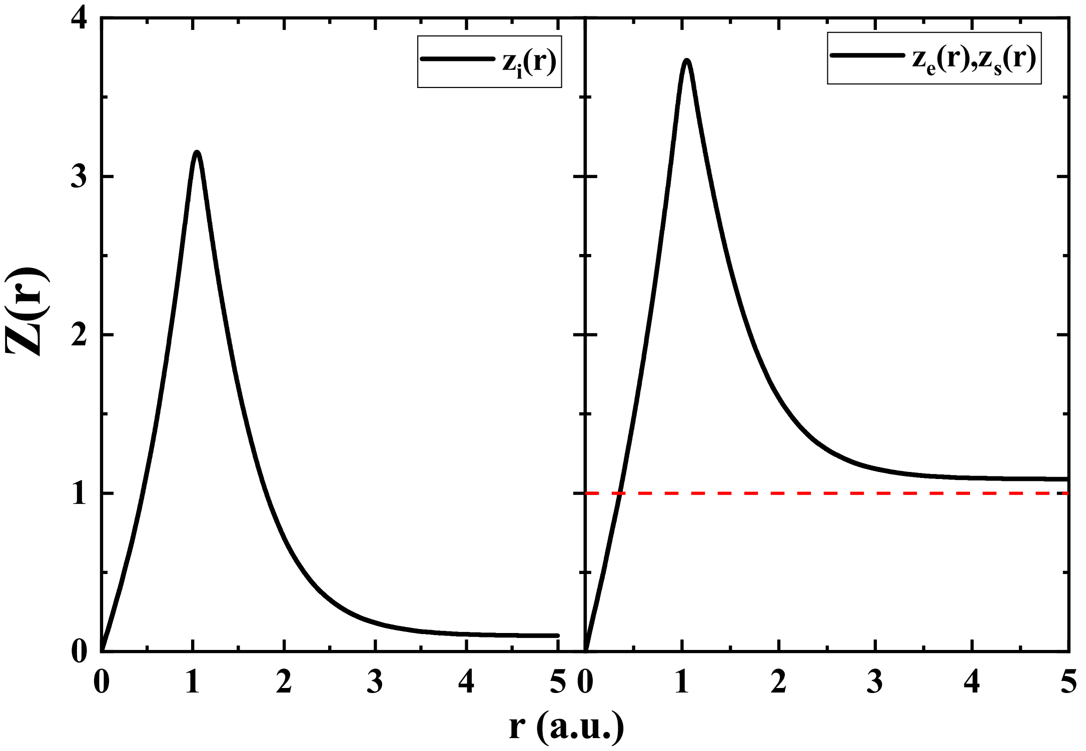

Figure 4.1: Variable charge $Z(r)$ felt by (a) the incident electron and (b) the outgoing electrons during the ionization process for the $3\sigma_g$ molecular orbital of N_2.

The aim of this work is to use the M3CWZ model to study the details of the ionization reaction of nitrogen molecule by electron and positron impact. Theoretical results are then discussed and compared with TDCS measurements available for both positron and electron impact ionization performed in asymmetric coplanar kinematics and with other theories.

4.3 Results and Discussion

The triple differential cross section has been calculated for the ionization of nitrogen molecule by electron and positron impact within the M3CWZ theoretical model, where single center molecular orbitals have been used to describe the target. Prior to assessing the M3CWZ model, the target molecular orbitals used in this work should be probed beforehand. Electron momentum spectroscopy (EMS) represents the best commonly used technique for testing molecular orbitals, it has even become a powerful tool for the design of high quality wave functions in quantum chemistry.

4.3.1 Electron momentum spectroscopy (EMS) study

Electron momentum spectroscopy is used to probe the wave functions of any target [3], since it measures directly the square of the momentum space overlap function between the initial ground state of the molecule and the ion in its final state. The theoretical background of EMS can be found in our previous work [4] and references therein, we present here only the main aspects of the technique. EMS experiments are carried out at intermediate impact energies ($1-2\ keV$), with the two outgoing electrons sharing equal energies. As a result, the reaction mechanism is simple enough and the projectile as well as the ejected electron can be described by plane waves, the TDCS in EMS studies is hence calculated in the so called PWBA model, the calculated TDCSs are called momentum profiles. In the frozen-core approximation, the measured electron impact cross sections in EMS are directly related to the square of the momentum space wave function, constituting as such a sensitive probe of distributions of electrons in atomic and molecular targets. In EMS experiments, the two outgoing electrons are detected at polar angles ($\theta_1 = \theta_2 = 45°$). The non-coplanar symmetric geometry is used, the TDCS is then displayed as a function of the recoil momentum which is written as:

$$q = \left[(k_1\sqrt{2} - k_i)^2 + 2k_1^2 \sin^2\left(\frac{\Phi}{2}\right) \right]^{1/2} \tag{4.7}$$

where $\Phi = \pi - |\phi_2 - \phi_1|$, ϕ_1 and ϕ_2 are the azimuthal angles of the scattered and ejected electrons.

Generally, ϕ_1 is kept to be zero and ϕ_2 is varied from 0° to 30°. Our theoretical momentum profiles for nitrogen molecule are compared with EMS experiments performed at $\sim$ 1500 eV impact energy [5], in order to test the molecular orbitals used to describe the target.

Figure 4.2 shows PWBA theoretical results for the ionization of the $2\sigma_g$, $2\sigma_u$, $1\pi_u$, and $3\sigma_g$ orbitals, experiments as well as other theoretical results are also displayed. Note that the EMS data are given on a relative scale, experiments and theories have been placed on a common intensity scale, by normalizing to our theoretical results. It is seen that comparison between our theoretical results with experiments in the outer valence region is quite promising and leads to good agreement with the data. Furthermore, we would also note that our description of the target provides results that are quasi similar to rather sophisticated SCF calculations of the ADC(4) many body model [5, 6]. This agreement reveals that the molecular single centred molecular orbitals used in this work in order to investigate the ionization dynamics are of good quality and constitute an accurate description of the molecular target.

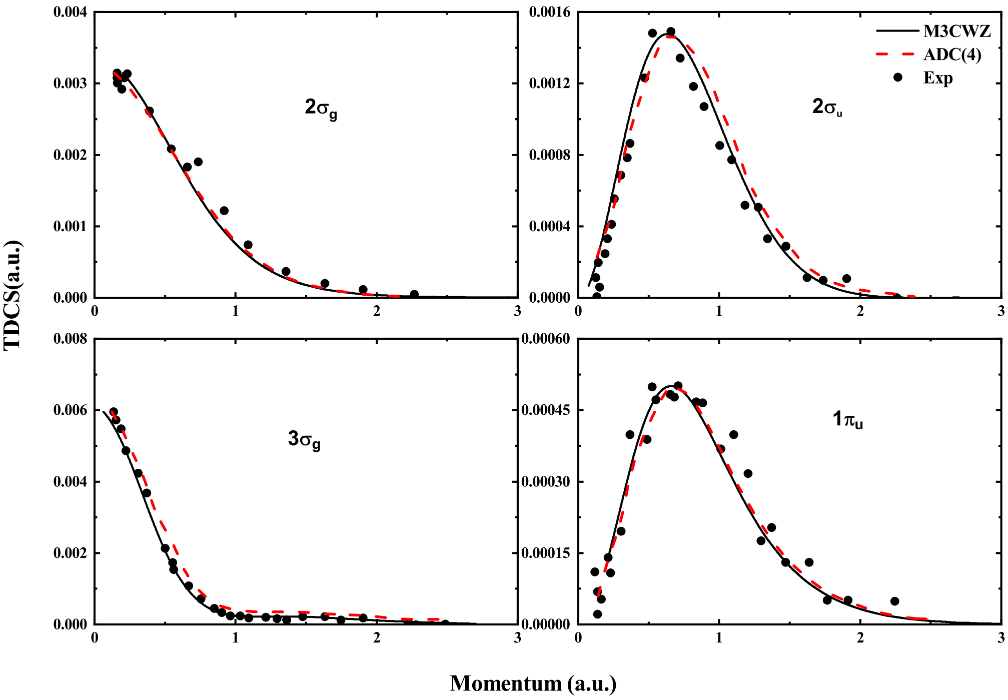

Figure 4.2: EMS momentum profile reported in a non coplanar symmetric geometry at 1500 eV impact energy as a function of the recoil momentum, the outgoing electrons are detected at 45° polar angles sharing the same energy. Theoretical PWBA results (black solid line) are compared with experimental data (black full circles) taken from [5] and ADC(4) calculations [6]. Theory and experiments have been normalized to present theoretical results for the best visual fit.

4.3.2 Collision dynamics study

We discuss now the dynamics of the ionization reaction by comparing the calculated TDCS's with experiments performed in asymmetric coplanar kinematics. We consider then a comprehensive set of data for electron and positron impact ionization, all performed in asymmetric coplanar geometry, in order to benchmark our calculations with these data as well as other available theories.

The first situation deals with the (e,2e) measurements of Lahmam bennani et al [7] for nitrogen molecule where the projectile is scattered with energy $E_1 = 500\ eV$ and an angle $\theta_1 = 6°$, while the ejected electron is detected with energies $(E_2 = 37,\ 74 \text{ and } 205\ eV)$. These experiments are characterized by large recoil momentum q which means an important participation of the residual ion in the reaction, the TDCS exhibits thereby a large intensity in the recoil region. The investigated data correspond to the ionization of the inner valence orbital $2\sigma_g$ and the outer valence orbitals ($2\sigma_u$, $1\pi_u$ and $3\sigma_g$). As stated in [7], the inner $2\sigma_g$ orbital whose ionization potential is $I = 37.9\ eV$ is well isolated while the outer orbitals $2\sigma_u$ ($I = 18.75\ eV$), $1\pi_u$ ($I = 16.7\ eV$) and $3\sigma_g$ ($I = 15.6\ eV$) are not resolved, this is related to the close spacing between electronic states faced usually by molecular targets. As a result, the (e,2e) data are provided with a 100% efficiency for $3\sigma_g$,78% for $1\pi_u$ and 32% for $2\sigma_u$, our TDCS for the outer orbitals will hence be presented as a weighted sum ($3\sigma_g + 0.78 \times 1\pi_u + 0.32 \times 2\sigma_u$). Our theoretical results are displayed in figures 4.3 and 4.4 and compared with experiments and other theories. The weighted sum of TDCS is presented in Fig. 4.3 as a function of the ejection angle for the outer orbitals ($2\sigma_u$, $1\pi_u$ and $3\sigma_g$) for ejection energies $E_2 = 37\ eV$ (panel a), $E_2 = 74\ eV$ (panel b) and $E_2 = 205\ eV$ (panel c). As the data are given on a relative scale all results are normalized to the M3CWZ model in the binary region. Comparison is also made with M3DW and DWBA models [7,8] where the PCI is included via Ward-Macek factor [9] for DWBA and exactly treated for M3DW. Note that results are also available with a rather poor First Born model (FBA-TCC) using bicentric Slater-type molecular orbitals [7]. In this model no PCI is taken into account and the projectile is described by a plane wave, results within this model are rather poor, results on FBA-TCC model have not been used in this work due to large observed discrepancies with experiments.

The first observation is that the data present a two lobe structure in the whole angular range, the first lobe in the binary region and the second one in the recoil region, this two lobes structure is qualitatively better exhibited by M3CWZ. Indeed, it is shown that in the binary region the shape of the TDCS is better reproduced by M3CWZ for kinematics of panels (a) and (c) especially for lower ejection angles $\theta_2 \inf 30°$ while for panel (b) M3CWZ and DWBA predictions are overall similar (M3DW are available only for kinematics of panel b). In the recoil region the best agreement with experiments is illustrated by M3CWZ in all cases, the DWBA model is not able at all to reproduce the peak for ejection energies $E_2 = 37\ eV$ and $74\ eV$ but does better for $E_2 = 205\ eV$, M3CWZ results remain still closer to the data that those of DWBA even at $E_2 = 205\ eV$.

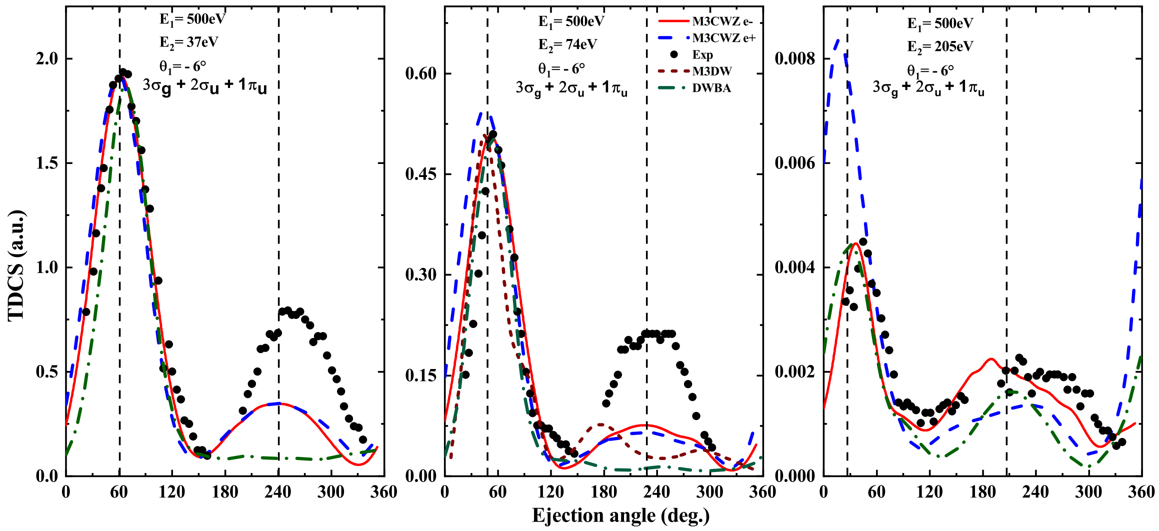

Figure 4.3: Weighted sum (see text) of the TDCS for the ionization of N_2 from the ($3\sigma_g$, $1\pi_u$ and $2\sigma_u$) outer valence orbitals by electron impact. The projectile is scattered with energy $E_1 = 500eV$ at fixed angle $\theta_1 = 6°$ and detected in coincidence with the ejected electron with energy (a) $E_2 = 37eV$, (b) $E_2 = 74eV$ and (c) $E_2 = 205eV$. Electron impact calculations of M3CWZ represented by red solid line, are compared with the experimental data for electron impact (black full squares) taken from [7], M3DW (wine short dashed line) [7] and DWBA (green dashed dotted line) [8]. The blue dashed lines represent M3CWZ calculations for positron impact. Experiments and theory have been normalized to M3CWZ results in the binary region for electron impact. Positron impact calculations (blue dashed line) are represented on their absolute scale. The dashed vertical lines indicate the momentum transfer $\vec{K}$ and its opposite direction $-\vec{K}$.

In addition, we should note that kinematics of panels (a) and (b) correspond to a recoil momentum 2.4 au and 3.2 au respectively while for panel (c) the recoil momentum gets even bigger and reaches nearly 5.4 au, this explains the amplitude of the recoil peak which is more important in this case than that in the binary region. This is in fact markedly illustrated in Fig. 4.3 if we look to details of the data, it is indeed seen that the recoil-to-binary ratio (RB) increases with increasing ejection energies, the ratio becomes much more important for $E_2 = 205$ eV which means a stronger interaction between the electron and the residual ion. The M3CWZ model reproduces rather well this features, we can see that the RB ratio increases with ejection energy to reach the value (≈ 0.5) at 205 eV ejection energy in perfect agreement with experiments. When we consider the inner $2\sigma_g$ orbital in Fig. 4.4, it is still observed that the TDCS exhibits a binary and a recoil peaks, the recoil peaks are now much stronger for all ejection energies, revealing a more significant participation of the residual ion to the reaction. It is shown that for this orbital, theoretical results reproduce more or less the shape of the angular distribution but underestimate substantially the data in the recoil region. Furthermore, the binary region is somewhat fairly described by theory while in the recoil region M3CWZ model predicts better the data for all energies, the recoil peak is qualitatively reproduced but underestimates clearly the data. DWBA results show clear discrepancies with the data except at $E_2 = 205\ eV$ where a recoil peak is somewhat reproduced but remains quite far from experiments. When we look at the RB ratio, M3CWZ results show that the RB is increasing with growing ejection energy in a qualitative agreement with the data. Quantitatively speaking, this ratio is nevertheless more important experimentally than theoretically, it reaches about 1.6 experimentally at 205 eV ejection energy while M3CWZ provides nearly 0.6. It's worth noting that the deficiencies observed for the inner orbital in the recoil region could be attributed to the use of the single picture approximation, in which the valence electrons are treated as part of the frozen nucleus and are then inactive; it would be interesting to take into account the other electrons of the target, especially for inner rbitals. Unfortunately, the situation for the theory turns out to be more dramatic if we consider the other electrons, since matrix elements become computationally very expensive to evaluate. Another alternative to improve the agreement with experiments is to use Second Born models, where the projectile undergoes a double interaction during the collision with the target.

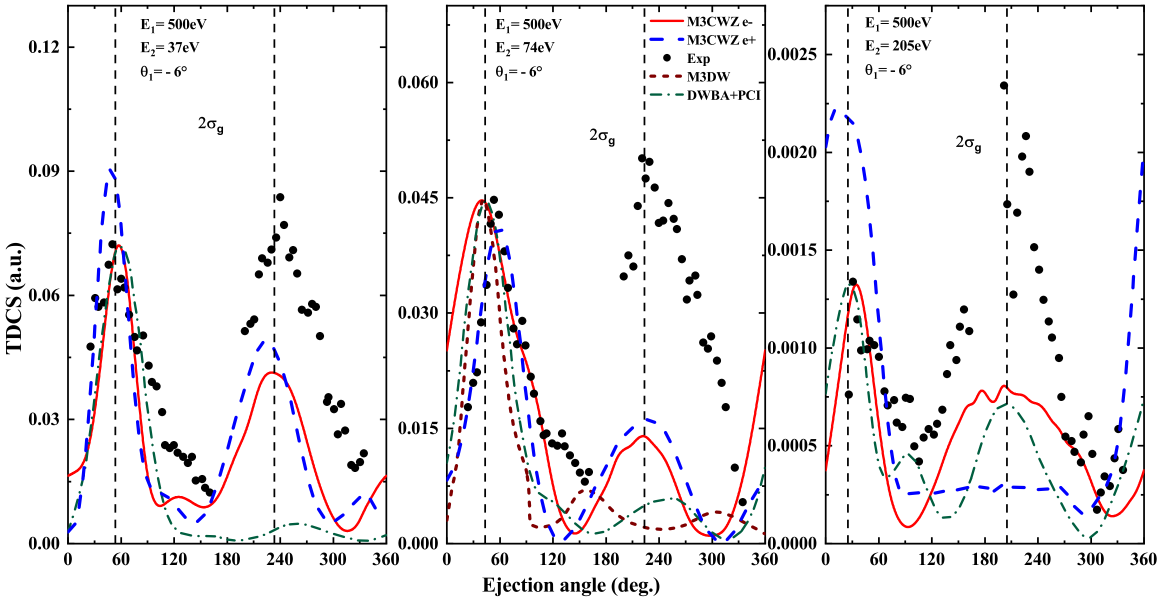

Figure 4.4: Triple differential cross section for the ionization of the inner $2\sigma_g$ orbital of N_2. Kinematics and symbols are the same as in 4.3.

For deeper insight to the ionization reaction we have presented theoretical calculations of the ionization process by positron impact based on the M3CWZ model in the same kinematics, our results are displayed as blue dashed lines for all situations in Figs 4.3 and

4.4, bearing in mind that for the present kinematics no experimental data are available for positrons for these kinematics to our knowledge. For a comprehensive study the directions of the momentum transfer $\vec{K}$ and its opposite $-\vec{K}$ have also been represented by vertical dashed lines. Overall, it is observed that the amplitude of the TDCS is enhanced for positron impact reaction in the binary region while in the recoil region the opposite occurs, this feature is better exhibited at 205 eV (panels c , Fig. 4.3 and 4.4) . When we look at the position of the peaks (with respect to the direction of the momentum transfer $\vec{K}$ and its opposite $-\vec{K}$), we can see in most cases (except kinematics of Fig. 4.4 , panel c) that, in the binary region the peaks are shifted in the backward directions for positrons and in the forward directions for electrons, in the recoil region we observe rather the opposite. Furthermore, this shift is more visible in both Fig. 4.3 and 4.4 at 205 eV ejection energy (panel c). All these features have been predicted by Dubois and de Lucio [10] and confirmed by Zaidi et al. [2] for argon atom, the present findings illustrate manifestations of projectile charge effects in the structure of the angular distribution of the TDCS. The features observed in the TDCS for positron and electron impact ionization reaction are attributed to the post collision interaction which is considered in our modeling and exactly treated. It's worth noting that the difference in the amplitude and the shift in positions for positron and electron impact are clearly more visible at 205 eV ejection energy (panel c) than for lower ejection energies (panels a and b), because in kinematics of panel(c) the PCI is much more important playing therefore a more significant role in the ionization reaction. We should note however that for the inner $2\sigma_g$ orbital, these features are unfortunately not clearly exhibited at 74 eV ejection energy (panel b, Fig. 4.4).

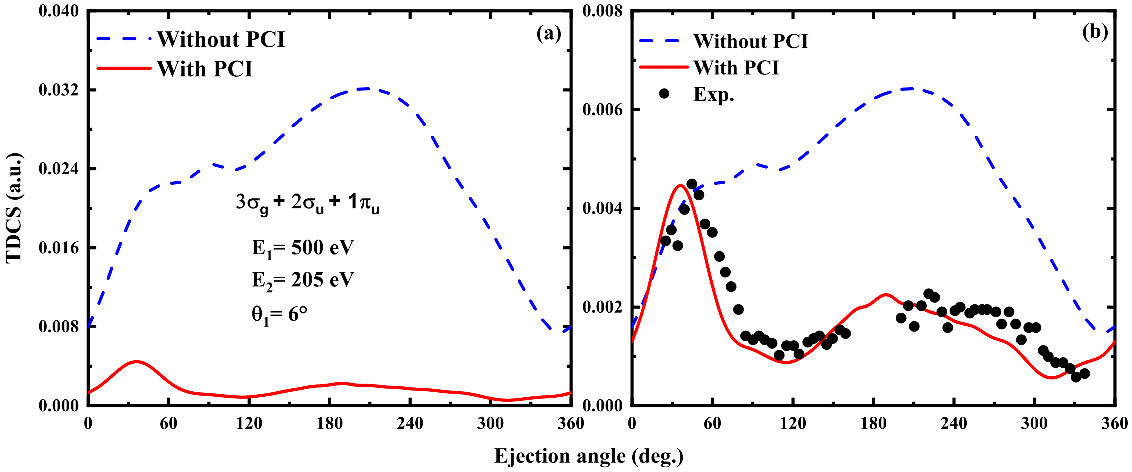

Figure 4.5: Weighted sum of the TDCS for the ionization of N_2 from the ($3\sigma_g$, $1\pi_u$ and $2\sigma_u$) outer valence orbitals by electron and positron impact. The projectile is scattered with energy $E_1 = 500\ eV$ at a fixed angle $\theta_1 = 6°$ and detected in coincidence with the ejected electron with energy $E_2 = 205\ eV$. Electron impact calculations of M3CWZ with PCI (by red solid line) and without PCI (blue dashed line) are presented in their absolute scales in panel (a). Panel (b) shows the same results with a comparison to experiments [7], where the data and theoretical predictions have been normalized to M3CWZ results in the binary region.

To conclude this part of discussion we make a comprehensive study for M3CWZ model where the investigation focuses on the role of the PCI for these particular kinematics. In Fig.4.5, theoretical TDCS calculations are displayed for M3CWZ with and without PCI, for kinematics of Fig. 4.3-c where the ejected electron is detected with an energy $E_2 = 205\ eV$ rather close to that of the ejected electron $E_1 = 500\ eV$, for this situation the PCI is expected to be more important. In panel (a) obtained results are exhibited on their absolute scales for a more comprehensive study, it is seen that calculations performed without PCI overestimate dramatically those with PCI in the binary as well as the recoil regions. In addition, calculations without PCI show a very strong peak in the recoil region, larger than the peak in the binary region. To provide a comprehensive study, theoretical calculations are compared with experiments [7] and shown in panel (b). Since experiments are relative, theory and experiment have been normalized to the M3CWZ calculation with PCI in the binary region. It is clearly observed that the calculations with PCI agree quite well with the experiments, as shown above, while those without PCI show strong discrepancies when compared with the data in the recoil region. We can state that our model, which includes and treats the PCI exactly, is able to well predict the data for this particular situation. In all situations considered in this work, the PCI is systematically taken into account.

In the following part, we investigate the ionization reaction by positron and electron impact at lower 250 eV impact energy, where experimental data are now provided for both electron and positron projectiles [11]. Measurements have been reported in asymmetric kinematics, for the outermost $3\sigma_g$ orbital at a scattering angle $\theta_1 = 3°$ and three ejection energies,$E_2 = 6,\ 12.4$ and $24.7\ eV$. Furthermore, in contrast with situations investigated in Fig. 4.3 and 4.4 at large momentum transfer, present kinematics are performed in the dipolar regime with a low momentum transfer ranging between 0.29 and 0.42 au.

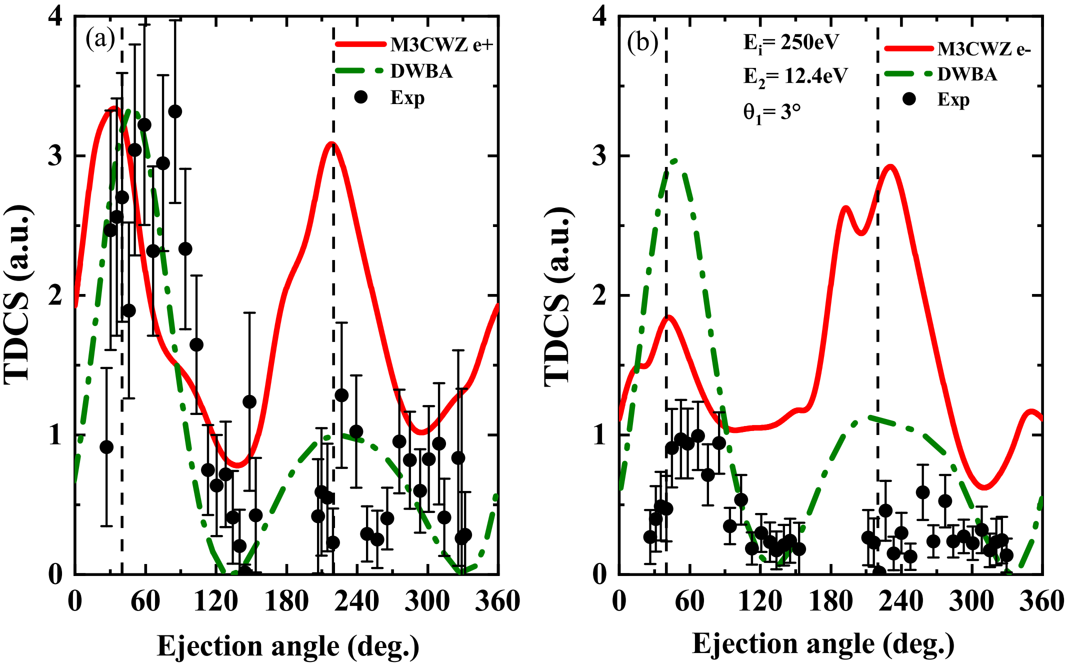

Figure 4.6: Triple differential cross section for the ionization of the $3\sigma_g$ orbital of N_2 by positron (panel a) and electron (panel b) impact at 250 eV projectile energy. The projectile is scattered at a fixed scattering angle $\theta_1 = 3°$ and detected in coincidence with the ejected electron with energy $E_2 = 12.4\ eV$. Theoretical calculations of the M3CWZ model (red solid lines) are compared with experiments [11] and DWBA results (green dashed dotted line) [12]. Experiments and theory have been cross normalized to the positron curve in the binary region (see text). The dashed vertical lines indicate the momentum transfer $\vec{K}$ and its opposite direction $-\vec{K}$.

In Figure 4.6, the calculated TDCSs are displayed as a function of the ejection angle for an ejection energy $E_2 = 12,4\ eV$ corresponding to a momentum transfer $K \approx 0.33\ au$. Since the data are given on a relative scale, they have been normalized to M3CWZ results in the binary region for positron impact in panel (a), the normalization factor has subsequently been kept for electron impact data in panel (b), M3CWZ results are represented and compared with experiments [11] as well as DWBA calculations [12]. It is seen that M3CWZ model exhibit trends which are similar to those observed in the previous situation at 500 eV scattering energy (Figs 4.3 and 4.4) say, the peak in the binary region is shifted in the backward direction for positrons (panel a) and in the forward direction for electrons (panel b) as expected. Moreover the peak is stronger in magnitude for positrons than for electrons in the binary region while in the recoil region the amplitudes are somewhat close. It is also observed that for electron impact (panel b) the shape of the TDCS shows a two lobe structure in both binary and recoil regions. When we make comparison with the data and the DWBA model, it is observed that unlike for M3CWZ, the peaks in the binary region are shifted in the forward direction for both electrons and positrons for DWBA. Similarly, the data are closer in magnitude to DWBA for both positrons and electrons in the recoil region, while M3CWZ better reproduces experiments for electrons in the binary region. It should also be noted that M3CWZ shows a strong peak in the recoil region for both positrons and electrons, in contrast to the data.

Finally, it is observed that the experimental data for positrons in the binary region seem to be surprisingly shifted in the forward direction in contradiction with theoretical predictions. It should be noted that for the present data [11], it has been stated that the statistical uncertainties can be significant because their experiments were carried out with beams considerably weaker than usually used, this naturally leads to strong influence on the detected electron emission. The uncertainties associated with the range of emission angles are rather important in the experimental setup, which could significantly affect the accuracy of measurements.

We consider now the two other sets of data at ejection energies 6 eV and 24.7 eV, displayed in Figs.4.7 and 4.8 respectively, for this kinematics no statistical uncertainties for the data are provided. At 6 eV ejection energy, M3CWZ significantly better agreement with the experimental data than DWBA calculations (Fig. 4.7). It is shown that DWBA presents two strong binary and recoil peaks similar in amplitudes in disagreement with the data for positron (panel a) as well as for electron impact (panel b). In contrast, at 24.7 eV ejection energy (Fig. 4.8), results are much better in magnitude for DWBA while M3CWZ displays strong recoil peaks for both positron and electron projectiles in disagreement with the data and DWBA results. When we look to the positions of the peaks, it is still observed for these kinematics (Figs. 4.7 and 4.8), M3CWZ results exhibit a peak in the binary region which is shifted to the backward direction for positron (panels a) and to the forward direction for electron (panels b), as it was observed at 12.4eV ejection energy (Fig.4.6) in perfect agreement with theoretical predictions. Also seen, the peaks exhibited by DWBA results and the data are shifted to the forward direction for both positron and electron impact. The comparison between amplitudes also shows that an enhancement of the amplitude for positrons with respect to electrons in the binary region, this feature is overall reproduced by the two theoretical models.

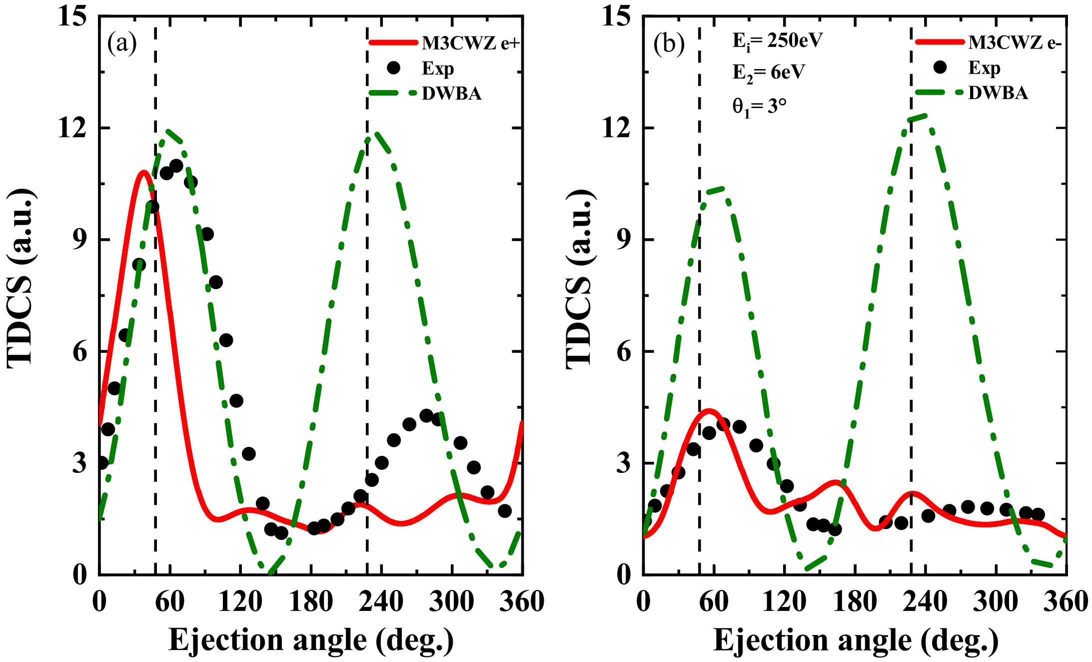

Figure 4.7: Same as Figure 4.6 but for $E_2 = 6eV$.

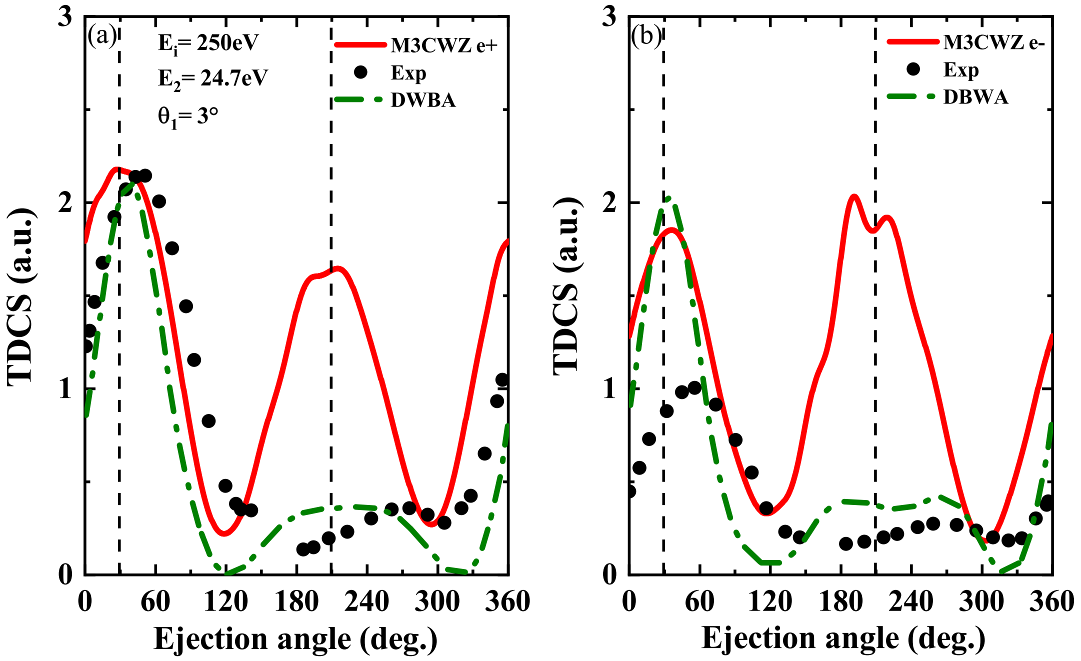

Figure 4.8: Same as Figure 4.6 but for $E_2 = 24.7eV$.

4.4 Summary and conclusions

This chapter presents, a comprehensive study of the ionization of the nitrogen molecule in its ground state by electron-positron collisions is reported within a model called M3CWZ, which has been previously applied to study the ionization of the water molecule by electron collisions at low collision energies [13]. a wide range of experimental kinematics has been considered in order to get an insight into the ionization reaction. In a first step, we considered (e,2e) measurements performed at 500 eV scattering energies and large recoil momentum, where the residual ion contributes strongly in the reaction, it has been found that M3CWZ model reproduces quite better the (e,2e) data than DWBA in all kinematics. A reasonable agreement was shown for the outermost orbitals ($2\sigma_u$, $1\pi_u$ and $3\sigma_g$) while for the inner $2\sigma_g$ orbital some discrepancies remain unfortunately observed, for this inner orbital M3CWZ reproduces qualitatively the shape of the TDCS angular distribution but underestimates markedly the magnitude of the recoil peak. In addition, the theoretical TDCS has also been plotted for the case of positron impact ionization in the same kinematics, an enhancement of the binary peak with respect to electron impact situation and a shift towards backward direction have been observed in practically all kinematics. These features are in quite good agreement with theoretical predictions, attesting a priori the validity of our modeling which includes and treats exactly the PCI.

Overall, the M3CWZ model predicts quite well the TDCS for the outer orbitals especially for high recoil momentum kinematics (Fig. 3, panel c), where the residual ion participates strongly to the reaction. Nevertheless, for the inner $2\sigma_g$ orbital severe discrepancies are observed between theory and experiments, this issue already observed for other molecular targets in similar kinematics [14], remains unsolved yet by available theories. Moreover we have investigated the same processes in completely different kinematics at lower impact energy (250 eV), corresponding this time to dipolar regimes where the momentum transfer is rather low. Measurements performed for the outer $3\sigma_g$ orbital have been compared to M3CWZ as well as to DWBA calculations. Theoretical results based on M3CWZ and DWBA models were rather mixed, as clear discrepancies with the data remain observed for the two models, The process should be further investigated to fix the origin of the observed discrepancies. It's worth noting that M3CWZ results for positron impact were shown to agree better with theoretical predictions and previous measurement [2, 10] when we look to the positions of the binary and recoil peaks. Moreover, we should indicate that experiments performed at 250 eV impact energies for both positron and electron impact seem to present some shortcomings related to the uncertainties in the measurements as stated in [11]. Calculations based on the M3CWZ and DWBA models show some good points and some weak points for each model, further experimental and theoretical investigations are needed for more accurate study of the Nitrogen molecule ionization.

Bibliography

[1] K. Bechane, S. Houamer, T. Khatir, A. Tamin, and C. Dal Cappello. Electron-impact ionization of argon in asymmetric kinematics. *Phys. Rev. A*, **109**(1):012812, 2024.

[2] O. Zaidi, A. Mansouri, S. Houamer, A. Tamin, T. Khatir, and C. Dal Cappello. Ionization of argon atom by positron and electron impact. *Eur. Phys. J. D*, **78**(11):65, 2024.

[3] M. A. Coplan, J. H. Moore, and J. P. Doering. (e,2e) spectroscopy. *Rev. Mod. Phys.*, **66**(3):985–1014, 1994.

[4] C. Champion, C. Dal Cappello, S. Houamer, and A. Mansouri. Single ionization of the water molecule by electron impact: Angular distributions at low incident energy. *Phys. Rev. A*, **73**(1):012717, 2006.

[5] J. P. D. Cook, R. Pascual, E. Weigold, W. von Niessen, and P. Tomasello. An experimental and theoretical investigation of the valence orbital momentum distributions of n_2. *Chem. Phys.*, **141**(2-3):211–223, 1990.

[6] J. Schirmer, L. S. Cederbaum, and O. Walter. New approach to the one-particle green's function for finite fermi systems. *Phys. Rev. A*, **28**(3):1237–1259, 1983.

[7] A. Lahmam-Bennani, E. M. Staicu Casagrande, and A. Naja. Dynamics of electron-impact ionization of the outer valence orbitals of co_2: (e,2e) study. *J. Phys. B*, **42**(23):235205, 2009.

[8] A. Pandey and G. Purohit. Tdcs calculation for the ionization of nitrogen molecule by electron impact. *Atoms*, **10**(2):50, 2022.

[9] S. J. Ward and J. H. Macek. Wave functions for continuum states of charged fragments. *Phys. Rev. A*, **49**(2):1049–1056, 1994.

[10] R. D. DuBois and O. G. de Lucio. Triply differential positron and electron impact ionization of argon: systematic features and scaling. *Atoms*, **9**(4):78, 2021.

[11] O. G. de Lucio and R. D. DuBois. Differential studies and projectile charge effects in ionization of molecular nitrogen by positron and electron impact. *Phys. Rev. A*, **93**(3):032710, 2016.

[12] G. Purohit and D. Kato. Projectile charge effects on the differential cross sections for the ionization of molecular nitrogen by positrons and electrons. *J. Phys. B*, **51**(13):135202, 2018.

[13] A. Tamin, S. Houamer, T. Khatir, L. U. Ancarani, and C. Dal Cappello. Electron-impact ionization of water molecules at low impact energies. *J. Chem. Phys.*, **161**(16):164305, 2024.

[14] A. Lahmam-Bennani, A. Naja, E. M. Staicu Casagrande, N. Okumus, C. Dal Cappello, I. Charpentier, and S. Houamer. Dynamics of electron impact ionization of the outer and inner valence (1t2 and 2a1) molecular orbitals of ch_4 at intermediate and large ion recoil momentum. *J. Phys. B*, **42**:165201, 2009.

Chapter 5

Investigation of Electron impact Double Ionization of Nitrogen Molecule

5.1 Introduction

Electron-impact double ionization of molecular targets provides a powerful tool for investigating the dynamics and electronic correlations within molecular structures. The work of the Orsay group (Lahmam-Bennani *et al.* [1, 2]) demonstrated that such experiments can be performed by detecting all three outgoing electrons in coincidence. This type of experiment, known as (e,3e), enables the measurement of the five-fold differential cross section (5DCS). An alternative approach, referred to as (e,3-1e), involves detecting only two of the three outgoing electrons in coincidence, allowing for the measurement of the four-fold differential cross section (4DCS).

In this chapter, we investigate the double ionization of the outermost $3\sigma_g$ orbital of the N_2 molecule by electron impact, using the Two Coulomb Waves with Gamow factor (2CWG) theoretical model developed within the First Born Approximation. Calculations of the 5DCS and 4DCS for the (e,3e) and (e,3-1e) processes, respectively, are carried out in a coplanar geometry for an incident energy of approximately 600 eV and for both equal and unequal energy sharing between the ejected electrons. Our aim is to examine the influence of first-order double ionization mechanisms (SO, TS1) on the double ionization process.

5.2 Theory

In the DI process (e, 3e), an incident beam of electrons collide with Nitrogen molecule in its fundamental state, the reaction is:

$$e^- + N_2 \to N_2^{2+} + e_s^- + e_1^- + e_2^- \tag{5.1}$$

The six-fold differential cross section (6DCS) for the DI can be expressed as

$$\begin{aligned}\sigma^{(6)}(\alpha,\beta) &= \frac{d^6\sigma}{d\Omega_{\text{Euler}} d\Omega_s d\Omega_1 d\Omega_2 dE_1 dE_2} \\ &= (2\pi)^4 \, \frac{k_s k_1 k_2}{k_i} \, |T_{if}(\alpha,\beta)|^2\end{aligned} \tag{5.2}$$

where $\sigma^{(6)}(\alpha,\beta)$ refers to a molecular orientation defined by two Euler angles (α, β) such as $d\Omega_{\text{Euler}} = \sin(\beta) d\beta d\alpha$.

The two ejected electron energies are denoted by E_1 and E_2. The scattered and the two ejected electrons are defined by their solid angles ($d\Omega_s$, $d\Omega_1$, $d\Omega_2$), and momenta ($\vec{k}_s$, $\vec{k}_1$, $\vec{k}_2$), respectively. The conservation of the energy and momentum in the (e, 3e) reaction is written as

$$\begin{aligned} E_i &= E_1 + E_2 + E_s + I \\ \vec{k}_i &= \vec{k}_1 + \vec{k}_2 + \vec{k}_s + \vec{q} \end{aligned} \tag{5.3}$$

I_i is the energy required for the double ionization of Nitrogen molecule. $\vec{q}$ represents the residual ion momentum.

Working in the frozen core approximation with two active electrons, the wave function of the initial state is given by

$$\Psi_i = \varphi_i(\vec{k_i}, \vec{r}_0)\Phi(\vec{r}_1, \vec{r}_2) \tag{5.4}$$

where $\varphi_i(\vec{k_i}, \vec{r}_0)$ is the incident electron wavefunction and $\Phi(\vec{r}_1, \vec{r}_2)$ is the wave function of the two bound electrons that will be ejected after the collision.

In the exit channel, the final state wave function is written as

$$\Psi_f = \varphi_f(\vec{k_s}, \vec{r}_0)\phi_f(\vec{k_1}, \vec{r}_1, \vec{k_2}, \vec{r}_2) \tag{5.5}$$

the incident and scattered electrons wave functions are represented by plane waves, since they have high kinetic energies

$$\varphi_{plane}(\vec{k_j}, \vec{r_0}) = \frac{e^{i\vec{k_j}\cdot\vec{r_0}}}{(2\pi)^{3/2}} \quad j = \{i, s\} \tag{5.6}$$

In the firt Born approximation frame work, the transition amplitude is:

$$T_{if} =< \Psi_f|V|\Psi_i > \tag{5.7}$$

V is the interaction potential between the incident electron and the two active electrons in the target, given by

$$V = -\frac{2}{r_0} + \frac{1}{|\vec{r_0} - \vec{r_1}|} + \frac{1}{|\vec{r_0} - \vec{r_2}|} \tag{5.8}$$

where $|\vec{r_0} - \vec{r_j}|$ the distance between the incident electron and each of the two ejected electrons.

In this study, we focus on the double ionization process of the outermost orbital $3\sigma_g^2$, the initial wave function of the two active electrons is given by

$$\Phi(\vec{r_1}, \vec{r_2}) = \phi(\vec{r_1})\phi(\vec{r_2}) \tag{5.9}$$

$\phi(\vec{r_j})$ are the single center molecular wave function expressed as a linear combination of Slater type functions:

$$\begin{gathered}\varphi(\vec{r}) = \sum_{k=1}^{N_j} a_{jk} R_{n_{jk}}^{\alpha_{jk}}(r) Y_{l_{jk}m_{jk}}(\Omega) \\ R_{n_{jk}}^{\alpha_{jk}}(r) = b_{n_{jk}} \; r^{n_{jk}-1} \; \exp(-\alpha_{jk} r)\end{gathered} \tag{5.10}$$

Using the 2CWG model, in the final state, both ejected electrons are represented by a coulomb wave and their mutual interaction is expressed by the repulsive Gamow factor $F_{Gamow}(k_{12})$, as

$$\phi_f(\vec{k_1}, \vec{r_1}, \vec{k_2}, \vec{r_2}) = \frac{1}{\sqrt{2}}(\phi_c(\vec{k_1}, \vec{r_1}, \vec{k_2}, \vec{r_2}) + \phi_c(\vec{k_1}, \vec{r_2}, \vec{k_2}, \vec{r_1})) \times F_{Gamow}(k_{12}) \tag{5.11}$$

where

$$\begin{gathered}\phi_c(\vec{r}) = \frac{e^{i\vec{k}\cdot\vec{r}}}{(2\pi)^{3/2}} e^{(-\pi\alpha/2)}\Gamma(1 - i\alpha)\, {}_1F_1(i\alpha, 1, -(ikr + i\vec{k}\cdot\vec{r})) \\ F_{Gamow}(k_{12}) = \exp(-\frac{\pi\alpha_{12}}{2})\Gamma(1 - i\alpha_{12}), \quad \text{with} \quad \alpha_{12} = \frac{1}{2k_{12}}\end{gathered} \tag{5.12}$$

The transition amplitude T_{if} in equation (5.7) is written as

$$T_{if}(\alpha,\beta) = \frac{1}{(2\pi)^3}\langle \phi_f(\vec{k_1},\vec{r_1},\vec{k_2},\vec{r_2})| - 2\frac{e^{i(\vec{k_i}-\vec{k_s})\cdot\vec{r_0}}}{r_0} + \frac{e^{i(\vec{k_i}-\vec{k_s})\cdot\vec{r_0}}}{|\vec{r_0}-\vec{r_1}|} + \frac{e^{i(\vec{k_i}-\vec{k_s})\vec{r_0}}}{|\vec{r_0}-\vec{r_2}|}|\Phi(\vec{r_1},\vec{r_2})\rangle \tag{5.13}$$

The integration over the projectile coordinate $\vec{r_0}$ in equation (5.13) is performed analytically using the Bethe relation:

$$\int \frac{e^{i\vec{K}\cdot\vec{r}}}{|\vec{r}-\vec{r_j}|}d\vec{r} = \frac{4\pi}{K^2}e^{i\vec{K}\cdot\vec{r_j}} \quad \text{with} \quad \vec{K} = \vec{k_i} - \vec{k_s}; \quad j = \{1,2\}$$

Equation (5.13) becomes

$$T_{if}(\alpha,\beta) = \frac{1}{(2\pi)^2}\frac{2}{k^2}\langle \phi_f(\vec{k_1},\vec{r_1},\vec{k_2},\vec{r_2})| - 2 + e^{i\vec{K}\cdot\vec{r_1}} + e^{i\vec{K}\cdot\vec{r_2}}|\Phi(\vec{r_1},\vec{r_2})\rangle \tag{5.14}$$

where $\vec{K}$ is the momentum transfer vector.

Finally the six-fold differential cross section 6DCS is then averaged over the two Euler angles to account for all possible orientations of the molecule.

$$\begin{aligned}\sigma^{(5)} &= \frac{d^5\sigma}{d\Omega_s\, d\Omega_1\, d\Omega_2\, dE_1\, dE_2} \\ &= \frac{1}{4\pi}\iint d\beta\, \sin\beta d\alpha[\sigma^{(6)}(\alpha,\beta)]\end{aligned} \tag{5.15}$$

Furthermore, integrating the 5DCS equation (5.15) over $d\Omega_2$ we obtain the four fold differential cross section corresponding to (e,3-1e) process where only the scattered electron and one of the ejected electron are detected in coincidence,

$$\begin{aligned}\sigma^{(4)} &= \frac{d^4\sigma}{d\Omega_s\, d\Omega_1\, dE_1\, dE_2} \\ &= \iint \frac{d^5\sigma}{d\Omega_s\, d\Omega_1\, d\Omega_2\, dE_1\, dE_2}d\Omega_2\end{aligned} \tag{5.16}$$

5.3 Results and Discussion

Five-fold (5DCS) and four-fold (4DCS) differential cross sections have been calculated for the electron impact ionization of the outermost $3\sigma_g$ orbital of the nitrogen molecule (N_2) within the first born approximation framework using the 2CWG theoretical model, in which the final state of the electrons emerging into the continuum is described using two Coulomb waves with a constante effective charge, the post collisional interaction between the two ejected electrons is represented by Gamow factor. The same single-center molecular wave function described previously in section 3.6 is employed here. These wave functions were previously validated by Electron Momentum Spectroscopy (EMS) measurements [3–6], confirming their high quality and their ability to provide an accurate description of the molecular target.

The dynamics of $(e, 3e)$ and $(e, (3{-}1)e)$ double ionization are investigated by comparing the calculated 5DCS and 4DCS with experimental measurements and other theoretical results, namely the Second-Born Aproximated Three coulomb waves (B2-A3C) [7] and the Two Center Continuum with correlation (TCC-C) [8] models. Experimental data from Li *et al.* [9–11] are used for the 4DCS $(e, (3{-}1)e)$ reaction in coplanar equal and unequal energy sharing conditions, and for the 5DCS $(e, 3e)$ reaction in coplanar equal energy sharing configurations.

5.3.1 The $e, (3-1)e$ reaction study

In the $(e, (3{-}1)e)$ reaction, the scattered electron of 500 eV is detected at an angle of $\theta_s = -6^\circ \pm 3^\circ$ with respect to the incident electron beam. For the ejected electrons we consider two cases in the equal energy sharing setup, $E_1 = E_2 = 12$ eV and $E_1 = E_2 = 37$ eV, and two cases in the unequal energy sharing setup, $E_1 = 72$ eV with $E_2 = 12$ eV, and $E_1 = 144$ eV with $E_2 = 12$ eV. The angular positions of the ejected electrons are measured with a tolerance of $\pm 8^\circ$, and their energies with a tolerance of ± 3 eV. The necessary incident electron energy is then obtained from the energy–conservation law (5.3), taking $I_i = 43$ eV as the double–ionization potential.

The 4DCS calculations are performed under the condition that, for unequal energy sharing, the slower ejected electron $e^-(\vec{k}_2, E_2)$ remains undetected, while the faster ejected electron $e^-(\vec{k}_1, E_1)$ is detected in coincidence with the scattered electron. In the case of equal energy sharing, one of the two ejected electrons is left undetected.

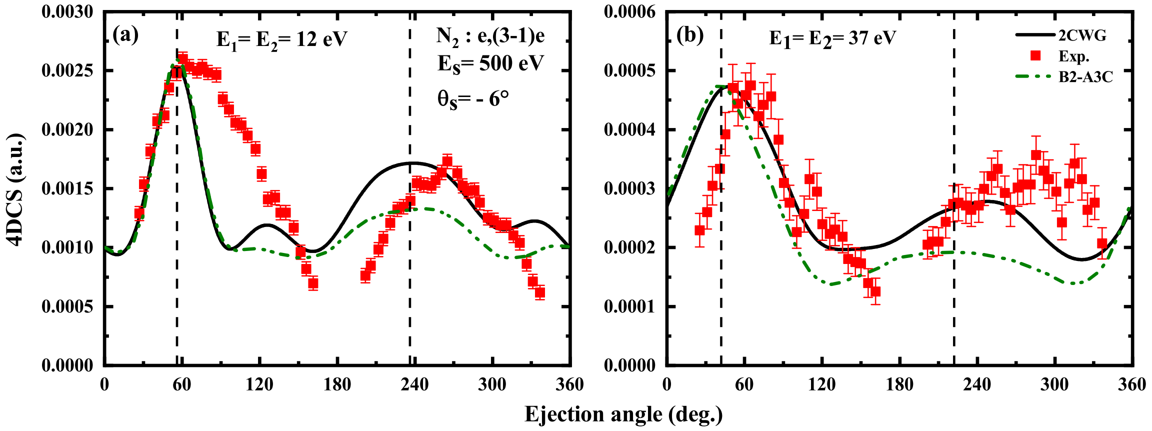

Figure 5.1: Four-fold differential cross sections (4DCS) for double ionization of $3\sigma_g$ of N_2. The scattered electron with energy $E_a = 500$ eV is detected at an angle $\theta_a = -6°$ in coincidence with one of the ejected electrons, while the second electron remains undetected. Panel (a): $(E_1 : E_2) = (12 : 12)$ eV; Panel (b): $(E_1 : E_2) = (37 : 37)$ eV. Red full squares are experimental data. The dashed vertical lines indicate the direction of momentum transfer (θ_K) and its opposite (θ_{-K}). The theoretical results of 2CWG are in solid black line while those of B2-A3C in green dash dotted line.

Figure 5.1 presents the $4DCS$ as function of the ejection angle θ_1 for $E_1 = E_2 = 12eV$ (panel a); $E_1 = E_2 = 37eV$ (panel b) corresponding to momentum transfer $K \approx 0.8\ au, 0.95\ au$ respectively. The experimental data is given in relative scale thus it has been normalized to 2CWG results in the forward lobe region. 2CWG results are represented and compared with B2-A3C [7] model as well as the experimental data [10]. We observe for both energy cases the same general structure, that is all angular distributions display a two lobes structure. A forward lobe is roughly around the momentum transfer direction ($+K$) and a backward lobe in the opposite direction ($-K$), respectively. These two directions are indicated by vertical dashed lines. Both 2CWG and B2-A3C models are able to reproduce the forward lobe in the given two equal energy sharing kinematics, the backward peak is better illustrated by 2CWG model in both cases than B2-A3C model. The theoretical calculations are somewhat symmetrically distributed about the $\pm K$ axis with a very slight shift which might be due to the uncertainty of $\sim 10°$ in the momentum transfer direction, although this uncertainty is very small to explain the large shifts seen in the experimental results, but we observe that the experimental maxima exhibit a shift from this axis direction as the ejection energy increases.

In addition, the experimental distributions exhibit additional structures for both the forward and backward lobes which are located at larger angles with respect to the momentum transfer direction.

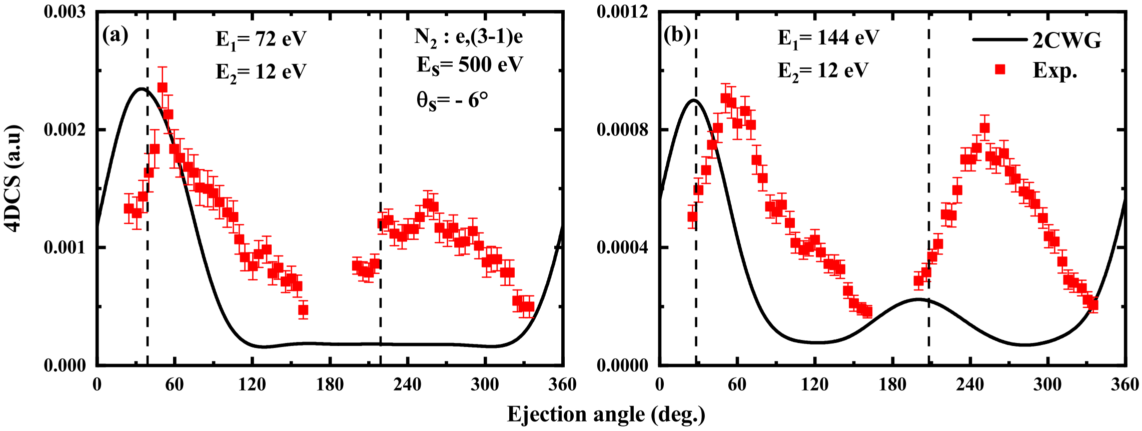

Figure 5.2: Same as Fig. 5.1 but for Panel (a): $(E_1 : E_2) = (72 : 12)$ eV; Panel (b): $(E_1 : E_2) = (144 : 37)$ eV. The scattered electron is detected in coincidence with the faster electron, while the slower electron remains undetected

Similarly Figure 5.2 represents $4DCS$ as function of the ejection angle θ_1 for $E_1 = 72\ eV, E_2 = 12\ eV$ (panel a) and $E_1 = 144\ eV, E_2 = 12\ eV$ (panel b) corresponding to momentum transfer $K \approx 0.99\ au; 1.3\ au$ respectively. To the best of our knowledge there is no available theoretical results for these kinematical conditions so our 2CWG results will be compared only with the experimental data. Again the measured angular distributions display a two lobes structure that are not symmetrically distributed about the momentum transfer direction $(+K)$ and its opposite $(-K)$ and a significant shifts of both forward and backward maxima can be observed. For the unequal energy sharing setup, the 2CWG model reproduces the the forward region peak around the momentum transfer direction $(+K)$ but it fails to reproduce the backward region peak.

5.3.2 The $e, 3e$ reaction study

In the $(e, 3e)$ reaction, the scattered electron with an energy of 500 eV is detected at an angle of $\theta_s = -6° \pm 3°$ relative to the incident beam. The two ejected electrons are subsequently analyzed for both energy and emission angle in coplanar symmetric energy conditions.

Figs. 5.3 and 5.4 present the Five-fold differential cross section (5DCS) calculations as function of both ejection angles θ_1 and θ_2 for the e,3e reaction using 2CWG model for outermost $3\sigma_g$ orbital of N_2 for $(E_1, E_2) = (12, 12)$ eV and $(37, 37)$ eV, respectively. We note that all the angular distributions of these cross sections exhibit two symmetric regions with respect to the direction $\theta_1 = \theta_2$. Consequently, we focus only on the description and analysis of one part of each figure, the other part being simply deduced by symmetry with respect to the axis $\theta_1 = \theta_2$.

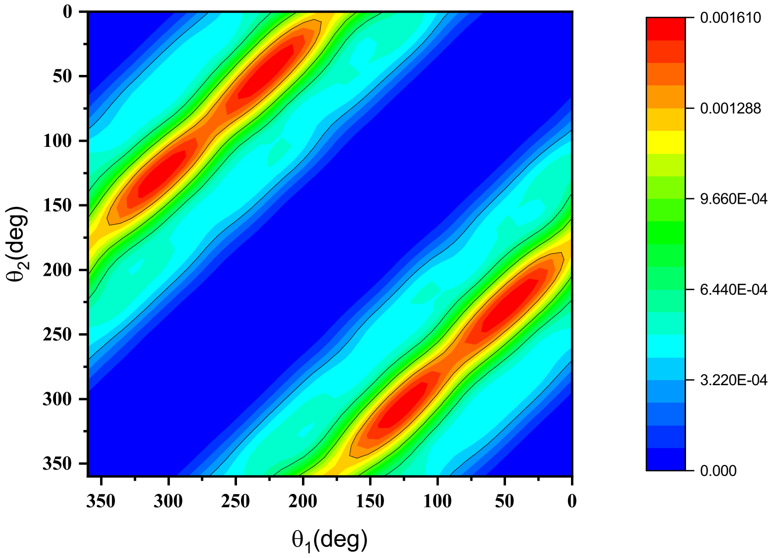

Figure 5.3: Five-fold differential cross sections (5DCS) calculated using the 2CWG model for the double ionization of the $3\sigma_g$ orbital of N_2. The scattered electron, with an energy of $E_s = 500$ eV, is detected at a scattering angle of $\theta_s = -6°$, in coincidence with two ejected electrons of equal energies $(E_1, E_2) = (12, 12)$ eV.

In Fig. 5.3, the angular distributions display a long wing lobe located in the ranges $\theta_1 \in [80°, 280°]$ and $\theta_2 \in [80°, 280°]$ with two prominent maxima at $(\theta_1, \theta_2) = (120°, 300°)$ and $(\theta_1, \theta_2) = (45°, 225°)$. Similarly in Fig. 5.4 the angular distributions display a long wing lobe located in the ranges $\theta_1 \in [60°, 300°]$ and $\theta_2 \in [60°, 300°]$ with two prominent maxima at $(\theta_1, \theta_2) = (40°, 220°)$ and $(\theta_1, \theta_2) = (135°, 320°)$.

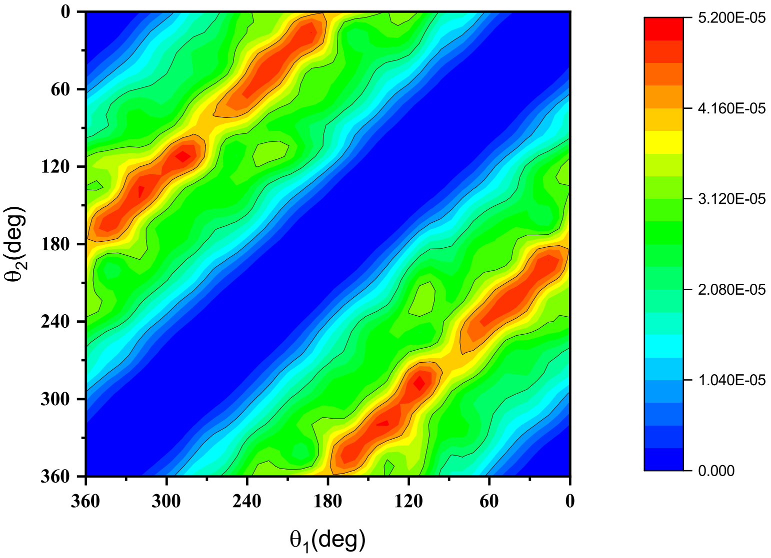

Figure 5.4: Same as Fig. 5.3 but for equal energies $(E_1, E_2) = (37, 37)$ eV.

Figs. 5.5(a) and 5.6(a) present the Five-fold differential cross section (5DCS) calculations as function of both ejection angles θ_1 and θ_2 for the e,3e reaction using 2CWG model for outermost $3\sigma_g$ orbital of N_2 for $(E_1, E_2) = (12, 12)$ eV and $(37, 37)$ eV, respectively. We also display in figs. 5.5(b) and 5.6(b) the only experimental measurement available to the best of our knowledge by Li et al [9]. Due to the fact that the experimental data is within a very limited angular ranges which are $200° < \theta_1 < 340°$ and $20° < \theta_2 < 160°$, we present our theoretical results in the same intervals for the sake of comparison.

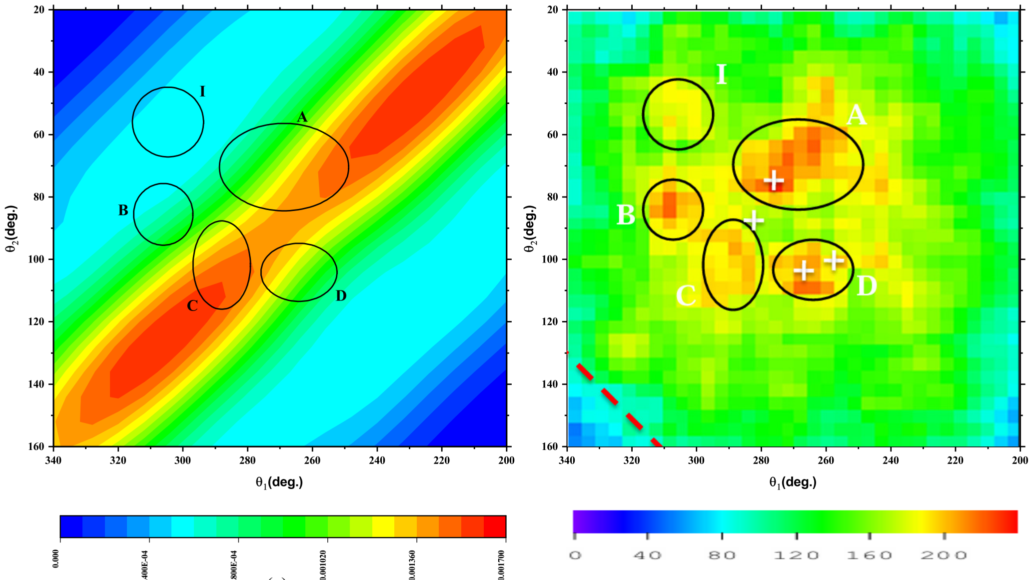

(a) (b)

Figure 5.5: panel (a): Same as Fig. 5.3, panel (b): the experimental results. The most prominent structures in the experimental results are encircled and labeled A, B, C, D, and I, respectively.

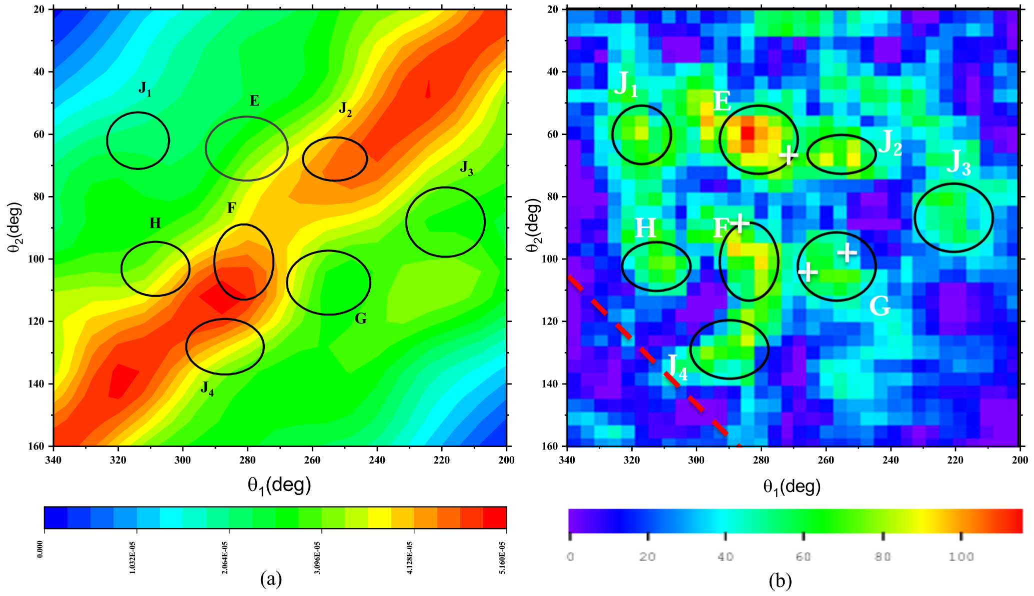

(a) (b)

Figure 5.6: panel (a): Same as Fig. 5.4, panel (b): the experimental results. The most prominent structures in the experimental results are encircled and labeled E, F, G, H, J_1, J_2, J_3, and J_4, respectively.

5.3.2.1 Discussion of 2D diagrams

The experimental two-dimensional (2D) diagrams exhibit a rich and intricate structure characterized by several pronounced maxima, reflecting the complex interaction between the incident electron and the target at low ejected-electron energies. For ease of comparison with our theoretical calculations, these prominent features are highlighted and labeled in the figures: regions A, B, C, D, and I in Fig. 5.5 correspond to the (12:12) eV case, while regions E, F, G, H, J_1, J_2, J_3, and J_4 in Fig. 5.6 correspond to the (37:37) eV case.

In Fig. 5.5(a), structures A (defined by $\theta_1 \in [244, 287]$, $\theta_2 \in [57, 84]$) and C (defined by $\theta_1 \in [278, 298]$, $\theta_2 \in [88, 118]$) show qualitative agreement with experiment, suggesting a possible contribution from first-order (first-Born) processes to the measured 5DCS distribution. However, since the first-order approximation alone fails to account for the remaining experimental features, we infer that, under the present kinematical conditions, the double-ionization process is primarily driven by second- and higher-order mechanisms such as the TS2 process. Structures B (defined by $\theta_1 \in [297, 315]$, $\theta_2 \in [74, 94]$) and D (defined by $\theta_1 \in [246, 277]$, $\theta_2 \in [94, 116]$) exhibit partial agreement with experiment, possibly indicating interference effects between first- and second-order mechanisms. The structure I (defined by $\theta_1 \in [294, 315]$, $\theta_2 \in [44, 67]$) appears weak and will be discussed in a later section.

A similar pattern is observed in Fig. 5.6(a). Structures F (defined by $\theta_1 \in [271, 290]$, $\theta_2 \in [88, 113]$), J_2 (defined by $\theta_1 \in [242, 262]$, $\theta_2 \in [60, 74]$), and J_4 (defined by $\theta_1 \in [275, 298]$, $\theta_2 \in [118, 136]$) show limited correspondence with experiment and may likewise stem from first-order contributions. Structures E ($\theta_1 \in [267, 292]$, $\theta_2 \in [54, 75]$), G ($\theta_1 \in [242, 268]$, $\theta_2 \in [97, 117]$), and H ($\theta_1 \in [297, 319]$, $\theta_2 \in [94, 112]$) partially reproduce the experimental behavior, which might again point to interference between first- and second-order mechanisms. Finally, structures J_1 ($\theta_1 \in [304, 323]$, $\theta_2 \in [52, 71]$) and J_3 ($\theta_1 \in [206, 230]$, $\theta_2 \in [76, 99]$), although less prominent, will be examined in detail in the following sections.

5.3.2.2 Discussion of different cuts

The 2D experimental diagrams shown in Figs. (5.5 (b)) and (5.6 (b)) provide an overall view of the data. Since the experiment collects data over many variable angles of both θ_1 and θ_2, the results can be sorted in different ways. Each choice corresponds to a different cut through the 2D angular distribution (5DCS) shown in Figs. 5.5 and 5.6. This allows the generation of many different angular distributions. To analyze the (e,3e) results in more detail, we now consider several specific cuts of these 2D diagrams. Many different cuts have been employed in previous works [12–16]. In this study, we restrict our investigation of the (e,3e) angular distribution to the geometrical cuts used by Li et al. [11]. These cuts are:

1. **θ-Variable mode**: θ_1 is fixed along the momentum transfer direction or its opposite, $\theta_{\pm K}$, while θ_2 is varied. In this particular geometry, first-order theoretical calculations are expected to produce a symmetric angular distribution around the momentum transfer direction. Thus, this mode serves as a useful tool to probe higher-order double ionization (DI) mechanisms, such as the two-step-2 (TS2) process.

2. **Fixed mutual angle mode**: Both ejection angles are varied while maintaining a fixed mutual angle $\theta_{12} = \pi$, corresponding to the back-to-back emission configuration. This setup highlights the contribution of the shake-off (SO) mechanism to the reaction.

3. **Symmetric geometry**: Both ejection angles are varied under the condition $\theta_1 = -\theta_2$.

Figures 5.7 and 5.8 show theoretical 5DCS calculations based on the 2CWG model for both energy cases $(E_1, E_2) = (12, 12)$ eV and $(37, 37)$ eV given in the θ-Variable mode cut, and compared with experimental measurements and results from B2-A3C model [7] as well as the two-center continuum model with electronic correlation in the final state within the first Born approximation (TCC-C) [8]. It should be noted that in the work of Chuub et al. [8], calculations were also performed using the two-center continuum model without electronic correlations in the final state (TCC-OC). However, in this study, we restrict our comparison to the TCC-C model.

Experimental data and theoretical results of TCC-C and B2-A3C models have been normalized to the maximum value of the 2CWG model, since the experimental measurements are given on a relative scale.

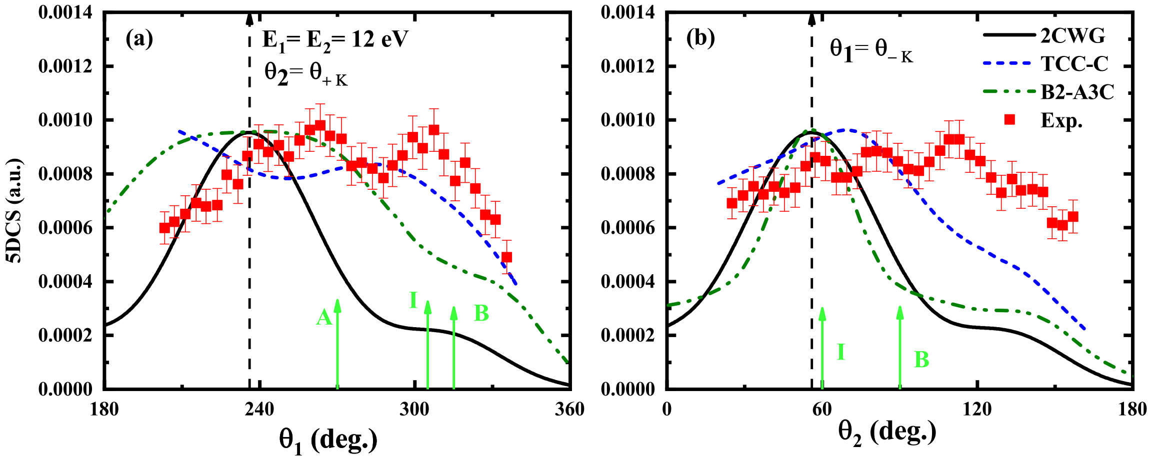

Figure 5.7: The variation of 5DCS of the (e,3e) DI of N_2 for $E_s = 500$ eV, $E_1 = E_2 = 12$ eV, $\theta_s = -6°$, the second ejected electron is along the momentum transfer θ_K in panel (a) and along opposite of momentum transfer θ_{-K} in panel (b). The results of 2CWG are represented by a solid black line, Experimental data are represented by full red squares. Green dash dotted line represents results of B2-A3C model and dashed blue is Two center continuum with correlation model. Vertical dashed lines indicate the direction of momentum transfer and its opposite.

For the $(E_1, E_2) = (12, 12)$ eV case, Fig. 5.7(a) corresponding to $\theta_2 = \theta_K = 56°$, the 2CWG model predicts an angular distribution that is symmetric around the opposite of the momentum transfer direction, $-\vec{K}$, exhibiting two distinct lobes. The first lobe, with the highest intensity, is centered around the $-\vec{K}$ direction, i.e., $\theta_1 = \theta_{-K} = 236°$, where $\theta_{12} = |\theta_1 - \theta_2| = 180°$. This configuration corresponds to a back-to-back electron emission characteristic of the first-order Shake-Off (SO) mechanism. The second, less intense lobe appears around $\theta_1 = 309°$, with $\theta_{12} = 107°$, suggesting an interaction associated with the first-order TS1 mechanism.

The experimental peak indicated by arrow A, located near $\theta_1 = 270°$ where $\theta_{12} = 146°$, is not fully reproduced by the theoretical calculations. This feature may result from interference between the SO and TS1 mechanisms. Additionally, since $\theta_{1s} = |\theta_1 - \theta_s| = 90°$, it strongly suggests the contribution of the second-order TS2 mechanism. The structure I, located near $\theta_1 = 305°$ with $\theta_{12} = 111°$, partially corresponds to the less prominent theoretical lobe, indicating interference between SO and TS1 processes. Similarly, structure B, located around $\theta_1 = 315°$ where $\theta_{2s} = 90°$, may also signify the presence of the TS2 mechanism.

The theoretical B2-A3C model exhibits a shape similar to that of the 2CWG calculation, although with a broader main peak. It reasonably reproduces the experimental peak denoted by arrow A; however, for Structure I, neither the position nor the amplitude is well reproduced. In contrast, the TCC-C model shows a general disagreement with the experimental data, failing to predict both the correct peak amplitudes and their corresponding angular positions.

For Fig. 5.7(b), corresponding to $\theta_1 = \theta_{-K} = 236°$, the 5DCS exhibits a symmetric distribution around the momentum transfer direction $\vec{K}$, again showing two main lobes. The first, more intense lobe is centered around $\vec{K}$, where $\theta_{12} = 180°$, consistent with back-to-back emission dominated by the SO mechanism. The second, weaker lobe appears at $\theta_2 = 124°$ with $\theta_{12} = 112°$, indicative of a TS1-type interaction. The structure I, marked by an arrow and located around $\theta_2 = 60°$, lies close to the momentum transfer direction $\vec{K}$, with $\theta_{12} = 176° \approx 180°$, again pointing to the dominance of the first-order SO mechanism through back-to-back emission. Finally, structure B, located at $\theta_2 = 90°$, where $\theta_{12} = 146°$ and $\theta_{2s} \approx 90°$, suggests a significant contribution from the second-order TS2 mechanism, which may compete with or dominate over the first-order SO and TS1 processes.

The B2-A3C model again follows a trend similar to that of the 2CWG calculation but fails to reproduce the experimental structures. The TCC-C model shows a reasonable agreement with the experimental data at lower ejection angles; however, it fails to reproduce the measurements at larger angles.

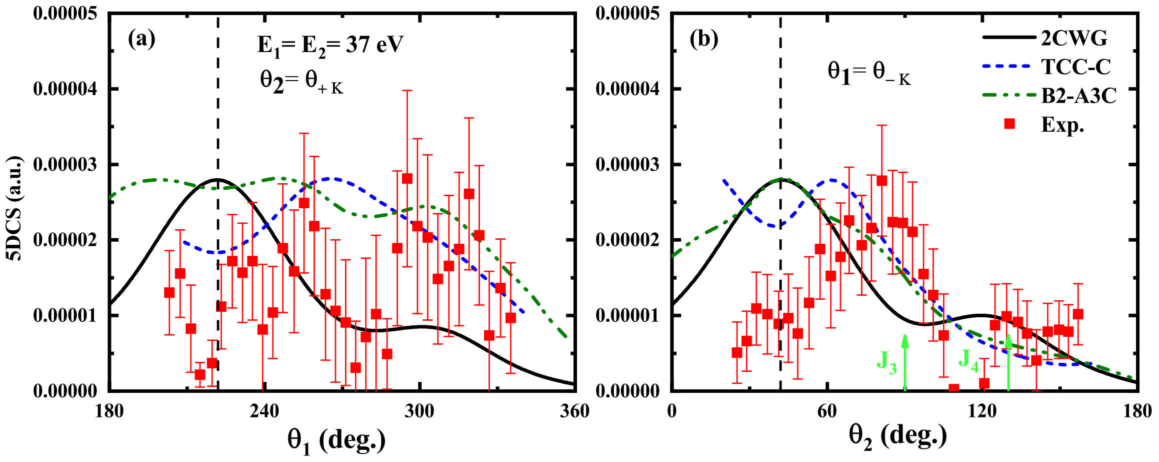

Figure 5.8: Same as Fig. 5.7 but for $E_1 = E_2 = 37$ eV.

For the $(E_1, E_2) = (37, 37)$ eV case, Fig. 5.8(a) corresponding to $\theta_2 = \theta_K = 42°$, the 2CWG model predicts an angular distribution exhibiting a symmetrical peak around the $-\vec{K}$ direction, located at $\theta_1 = 222°$ where $\theta_{12} = 180°$. This configuration suggests the dominance of the first-order Shake-Off (SO) mechanism, characterized by back-to-back electron emission. A second, less pronounced peak appears at $\theta_1 = 300°$ with $\theta_{12} = 102°$, indicating the presence of the first-order TS1 mechanism. However, due to the limited experimental statistics, it is difficult to make a detailed and reliable comparison between theory and experiment.

In Fig. 5.8(b), corresponding to $\theta_1 = \theta_{-K} = 222°$, the angular distribution again exhibits a symmetric pattern around the momentum transfer direction $\vec{K}$. The main maximum, centered at $\theta_2 = 42°$ with $\theta_{12} = 180°$, confirms the predominance of the back-to-back SO emission. A secondary peak of lower intensity is observed at $\theta_2 = 119°$ with $\theta_{12} = 103°$, which may be attributed to the TS1 mechanism. Furthermore, structure J_3 corresponds to a local maximum near $\theta_2 = 90°$ where $\theta_{12} = 132°$. This region suggests contributions from the TS1 mechanism; however, since $\theta_{2s} = 90°$, it also indicates a strong influence of the second-order TS2 process, likely overshadowing the first-order effects. Similarly to the $(E_1, E_2) = (12, 12)$ eV case, the B2-A3C model follows almost the same trend as the 2CWG calculation but fails to reproduce the experimental results. The TCC-C model shows limited agreement with the experimental data around the region where $\theta_2 = \theta_K$, although it overestimates the corresponding amplitude.

Figures 5.9 and 5.10 show theoretical 5DCS calculations based on the 2CWG model for both energy cases $(E_1, E_2) = (12, 12)$ eV and $(37, 37)$ eV given in the back-to-back configuration and the symmetric geometry cuts, and compared with experimental measurements and the two-center continuum model with electronic correlation in the final state within the first Born approximation (TCC-C) [8]. The results of the B2-A3C model for these kinematical conditions are not available.

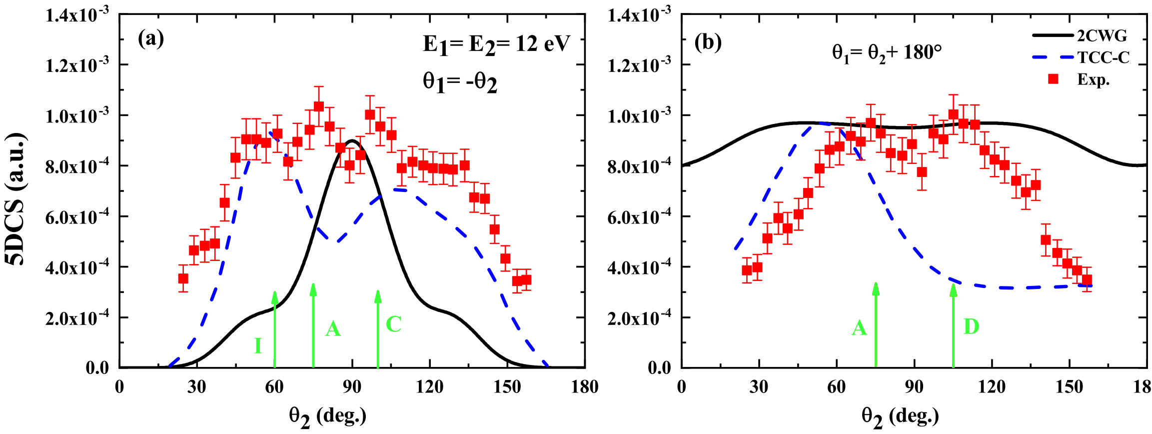

Figure 5.9: The variation of 5DCS of the (e,3e) DI of N_2 for $E_s = 500$ eV, $E_1 = E_2 = 12$ eV, $\theta_s = -6°$, the second ejected electron is along $\theta_1 = \theta_2 + 180°$ in panel (a) and along $\theta_1 = -\theta_2$ in panel (b). The results of 2CWG are represented by a solid black line, Experimental data are represented by full red squares. Dashed blue represents the Two center continuum with correlation model TCC-C.

For the $(E_1, E_2) = (12, 12)$ eV case, Fig. 5.9(a) (symmetric geometry mode), both the 2CWG model and the experimental results display a symmetric structure with respect to $\theta_2 \approx 90°$. The 2CWG calculation exhibits a main peak at $\theta_2 \approx 90°$, where $\theta_{12} = |\theta_1 - \theta_2| = 180°$. This peak roughly corresponds to structures A and C, which have previously been attributed to an interference pattern between the Shake-Off (SO) and TS1 mechanisms. Additionally, two less prominent peaks appear at $\theta_{1,2} = \pm 50°$ and $\theta_{1,2} = \pm 125°$, corresponding to $\theta_{12} = 100°$ and $110°$, respectively. The first of these may correspond to structure I, previously associated with first-order mechanisms, although the theoretical intensity is noticeably underestimated.

The TCC-C model exhibits two peaks that are, overall, in good agreement with the experimental data within the limits of the available angular interval.

Similarly, in Fig. 5.9(b) (back-to-back geometry mode), both the 2CWG and experimental data reveal a double-peak structure that is symmetric with respect to $\theta_2 \approx 90°$. Although the peaks are less distinct in the theoretical distribution, they are located near $\theta_2 = 47°$ and $119°$, corresponding to back-to-back emission configurations. The experimental peaks, observed at $\theta_2 = 73°$ and $105°$, are in reasonable agreement with the theoretical predictions and suggest a possible interference between the SO and TS2 mechanisms, particularly for structure D indicated by an arrow.

The TCC-C model exhibits only a single peak structure, which is roughly consistent with the left-hand peak observed in the experimental data, while the right-hand peak present in the experiment is completely absent in the theoretical prediction.

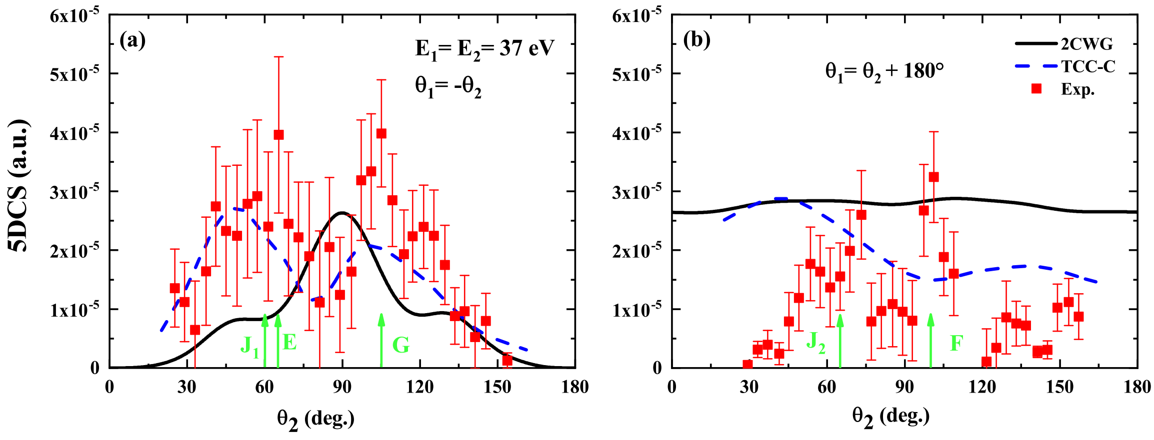

Figure 5.10: Same as Fig. 5.9 but for $E_1 = E_2 = 37$ eV.

For the $(E_1, E_2) = (37, 37)$ eV case, Fig. 5.10(a) presents the results for the symmetric geometry. The 2CWG model predicts a symmetric angular distribution about $\theta_2 \approx 90°$, with a maximum located at this angle where $\theta_{12} = 180°$, indicating the dominance of the Shake-Off (SO) mechanism. Two additional, less intense peaks appear at $\theta_2 = 49°$ and $128°$, corresponding to $\theta_{12} = 98°$ and $104°$, respectively, which can be attributed to contributions from the first-order TS1 mechanism.

Regarding the experimental data, despite the relatively large statistical uncertainties, two distinct peaks can be identified. Structure J_1, located around $\theta_2 \approx 60°$ where $\theta_{12} \approx 120°$, suggests the presence of the TS1 mechanism. Structure G, centered near $\theta_2 \approx 100°$ with $\theta_{12} \approx 160°$, indicates an interference pattern between the SO and TS1 mechanisms. Furthermore, since $\theta_{2s} \approx 90°$, this structure may also imply a contribution from the second-order TS2 mechanism.
The TCC-C model exhibits two peaks whose maxima are aligned with the positions of the experimental maxima. However, due to the significant statistical uncertainties in the experimental data, it is difficult to draw any definitive conclusions.

Figure 5.10(b) shows the results for the back-to-back geometry. The 2CWG model predicts a two-peak distribution symmetric about $\theta_2 \approx 85°$. Although the peaks are not very pronounced, their positions correspond closely to those observed experimentally. The first, structure J_2, appears around $\theta_2 \approx 70°$ where $\theta_{12} \approx 140°$, suggesting an interference pattern between the SO and dominant TS1 mechanisms. The second, structure F, is located near $\theta_2 \approx 105°$, where $\theta_{12} \approx 180°$ and $\theta_{2s} \approx 90°$, indicating an interference between the TS2 and dominant SO mechanisms. The TCC-C model exhibits two peaks, with the second one having a smaller amplitude compared to the first. However, the positions of these peaks do not align with those observed in the experimental data.

5.4 Summary and Conclusions

In this chapter, we conducted a theoretical investigation of double ionization (DI) processes in molecular nitrogen N_2, focusing on the $(e, 3e)$ and $(e, 3{-}1e)$ reactions induced by electron impact. The calculations focused on the ionization of the outermost molecular orbital, $3\sigma_g$, within the framework of the first Born approximation.

We employed the two Coulomb waves with Gamow factor (2CWG) model, where the incident and scattered electrons were treated as plane waves, while the two ejected electrons were represented by Coulomb waves. Post-collisional interaction effects between the two ejected electrons were incorporated using the Gamow factor, which is an approximation to the BBK model. For the initial state, a frozen core approximation was applied, considering only two active electrons described by a single-center wave function derived from a self-consistent field Hartree-Fock calculation using the LCAO-MO approach with Slater-type orbitals.

Our calculations included five-fold and four-fold differential cross sections (5DCS and

4DCS) under coplanar geometry conditions. For the $(e, 3-1e)$ process, both equal and unequal energy sharing configurations were considered, whereas only equal energy sharing was explored for the $(e, 3e)$ process.

The obtained theoretical results were compared with available experimental data and alternative theoretical models, namely the B2-A3C with Gamow factor model for both reaction channels, and the two-center continuum with correlation (TCC-C) model for the $(e, 3e)$ reaction.

These comparisons provided valuable insight into the reliability and limitations of the 2CWG model in describing correlated three-electron dynamics in DI processes.

Bibliography

[1] A. Lahmam-Bennani et al. Identification of mechanisms of electron impact double ionizing collisions by e,(3-1)e experiments. *J. Phys. B: At. Mol. Opt. Phys.*, **24**:9, 1991.

[2] A. Lahmam-Bennani, C. Dupré, and A. Duguet. Electron-impact double ionization of argon studied by double and triple coincidence techniques: The first (e,3e) experiment. *Phys. Rev. Lett.*, **63**:1582–1585, 1989.

[3] S. Mekhalfa, S. Houamer, A. Mansouri, I. Khiat, A. Tamin, C. Dal Cappello, and P.-A. Hervieux. Theoretical investigation of the triple differential cross section in the nitrogen molecule ionization by electron and positron impact. *J. Electron Spectrosc. Relat. Phenom.*, **281**:147545, 2025.

[4] M. A. Coplan, J. H. Moore, and J. P. Doering. (e,2e) spectroscopy. *Rev. Mod. Phys.*, **66**(3):985–1014, 1994.

[5] J. P. D. Cook, R. Pascual, E. Weigold, W. von Niessen, and P. Tomasello. An experimental and theoretical investigation of the valence orbital momentum distributions of n_2. *Chem. Phys.*, **141**(2-3):211–223, 1990.

[6] J. Schirmer, L. S. Cederbaum, and O. Walter. New approach to the one-particle green's function for finite fermi systems. *Phys. Rev. A*, **28**(3):1237–1259, 1983.

[7] P. Lamy, C. Dal Cappello, I. Charpentier, M. F. Ruiz-Lopez, and P.-A. Hervieux. The second born approximation for the double ionization of n_2 by electron impact. *J. Phys. B: At. Mol. Opt. Phys.*, **49**:135203, 2016.

[8] O. Chuluunbaatar, A. A. Gusev, and B. B. Joulakian. The correlated two-centre double continuum and the double ionization of h_2 and n_2 by fast electron impact. *J. Phys. B: At. Mol. Opt. Phys.*, **45**:015205, 2012.

[9] C. Li, A. Lahmam-Bennani, E. M. Staicu Casagrande, and C. Dal Cappello. Electron impact double ionization of neon, argon and molecular nitrogen: role of the two-step mechanism. *J. Phys. B: At. Mol. Opt. Phys.*, **44**:115201, 2011.

[10] C. Li, E. M. Staicu Casagrande, A. Lahmam-Bennani, and A. Naja. Identification of first order and non-first order contributions in the (e,3–1e) and (e,3e) double ionization of molecular nitrogen. *J. Phys. B: At. Mol. Opt. Phys.*, **45**:135201, 2012.

[11] C. Li. *Experimental study on electron impact double ionization dynamics for atomic and small molecular targets at intermediate incident energy.* Phd thesis, Université Paris-Sud, Institut des Sciences Moléculaires d'Orsay, 2013.

[12] C. C. Jia, A. Lahmam-Bennani, C. Dal Cappello, A. Duguet, and L. Avaldi. Deviations between experimental and theoretical results in ar (e, 3e) double ionization. *J. Phys. B: At. Mol. Opt. Phys.*, **36**:L17, 2003.

[13] C. Dal Cappello and H. Le Rouzo. Angular distributions in the double ionization of helium by electron impact. *Phys. Rev. A*, **43**:1395–1404, 1991.

[14] H. Hda, C. Dal Cappello, and J. Langlois. Angular distributions of electrons in the (e, 3e) reaction. *Z. Phys. D At. Mol. Clust.*, **29**:25–29, 1994.

[15] C. Schröter et al. Dynamics of the double-ionization process from (e, 3e) experiments: Ii. fivefold differential cross sections for neon. *J. Phys. B: At. Mol. Opt. Phys.*, **31**:131, 1998.

[16] A. Lahmam-Bennani et al. Complete experiments for the double ionization of he: (e,3e) cross sections at 1 kev impact energy and small momentum transfer. *J. Phys. B: At. Mol. Opt. Phys.*, **34**:3073, 2001.

General Conclusion

This thesis has presented a comprehensive theoretical investigation of single and double ionization processes induced by electron and positron impact on atomic and molecular targets, with particular emphasis on molecular nitrogen. The work integrates fundamental theoretical frameworks, detailed modeling, and extensive comparisons with available experimental data to advance our understanding of electron-target interactions.

The study began with an analysis of single ionization, establishing the essential conservation laws, kinematic descriptions, and experimental configurations required to characterize such reactions. Several established theoretical approaches, including BBK, DWBA, and M3DW, were reviewed, and a new model, M3CWZ, was introduced. By incorporating distortion effects and post-collisional interactions through a variable-charge scheme, the M3CWZ model demonstrated improved accuracy and computational efficiency for electron- and positron-impact ionization.

Building on this foundation, the thesis explored double ionization of both atomic and molecular systems, highlighting the greater complexity of these processes and the importance of electron-electron correlation. The main mechanisms Shake-Off, Two-Step 1, and Two-Step 2 were described, and the relevant experimental methods and theoretical models, including BBK and TCC, were examined. Molecular nitrogen was chosen as the primary target for detailed investigation. Calculations of five-fold and four-fold differential cross sections for the $(e, 3e)$ and $(e, 3\text{–}1e)$ reactions were performed using the two Coulomb waves with Gamow factor (2CWG) model and compared with advanced second Born and TCC-based theories as well as with experimental data. These comparisons provided insight into the role of electron correlation and the validity of different approximations across a range of kinematic conditions.

Overall, the results demonstrate that models incorporating post-collisional interactions and distortion effects, such as M3CWZ and 2CWG, are capable of reproducing many key experimental features, particularly for outer-shell ionization and high-recoil kinematics. Nonetheless, persistent discrepancies remain, especially for inner-shell ionization and in low-energy or strongly correlated regimes, where available theories show limitations.

This work underscores the continuing need for improved theoretical descriptions of multi-electron dynamics and for high-precision experimental measurements to guide and validate such models. By clarifying the mechanisms of single and double ionization and assessing the predictive capabilities of several theoretical approaches, the thesis contributes to the broader understanding of fundamental collision processes relevant to atomic, molecular, and plasma physics as well as related fields in applied science.

Appendix A

Calculation of Matrix Element for M3CWZ Model

The initial and final wavefunctions, denoted respectively by Ψ_i and Ψ_f, are expressed as follows:

$$\begin{aligned}\Psi_i(\vec{k}_i, \vec{r}_0, \vec{r}_1) &= \phi_c^{Z_i}(\vec{k}_i, \vec{r}_0)\Phi_(\vec{r}_1) \\ \Psi_f(\vec{k}_s, \vec{k}_1, \vec{r}_0, \vec{r}_1, \vec{r}_{01}) &= \phi_c^{Z_s}(\vec{k}_s, \vec{r}_0)\phi_c^{Z_e}(\vec{k}_1, \vec{r}_1)C(\alpha_{01}, \vec{k}_{s1}, \vec{r}_{01})\end{aligned} \tag{A.1}$$

Here, ϕ_c represents a Coulomb wavefunction characterized by a variable effective charge $Z(r)$, while C accounts for the post-collisional interaction (PCI) between the outgoing electrons:

$$\begin{aligned}\phi_c &= \frac{e^{i\vec{k}\cdot\vec{r}}}{(2\pi)^{3/2}} e^{\pi\alpha(r)/2}\Gamma(1 - i\alpha(r))_1F_1(-i\alpha(r), 1, -i(k_{01}r_{01} + \vec{k_{01}} \cdot \vec{r_{01}})) \\ C(\alpha_{01}, \vec{k}_{01}, \vec{r}_{01}) &= e^{\pi\alpha_{01}/2}\Gamma(1 - i\alpha_{01})_1F_1(-i\alpha_{01}, 1, -i(\vec{k}_{01}r_{01} + \vec{k}_{01} \cdot \vec{r}_{01}))\end{aligned} \tag{A.2}$$

Such that:

$$\vec{r}_{01} = (\vec{r}_0 - \vec{r}_1), \quad \vec{k}_{s1} = \frac{1}{2}(\vec{k}_s - \vec{k}_1), \quad \alpha(r) = \frac{Z(r)}{k}, \text{ and } \quad \alpha_{01}(r) = -\frac{1}{2k_{01}}. \tag{A.3}$$

The potential V describes the Coulomb interaction between the incident projectile and the active (ejected) target electron, and is given by:

$$V = -\frac{1}{r_0} + \frac{1}{r_{01}}; \quad r_{01} = |\vec{r}_0 - \vec{r}_1| \tag{A.4}$$

The corresponding transition matrix element T_{if} is therefore written as:

$$T_{if} = \langle\Psi_f|V|\Psi_i\rangle \tag{A.5}$$

The matrix element becomes:

$$T_{if} = T_{if}^{Int} - T_{if}^{0} \tag{A.6}$$

calculating T_{if}^{Int}

$$T_{if}^{Int} = \iiint \phi_c^{Z_s *}(\vec{k}_s, \vec{r}_0)\phi_c^{Z_e *}(\vec{k}_1, \vec{r}_1) C^*(\alpha_{01}, \vec{k}_{s1}, \vec{r}_{01}) \left(\frac{1}{r_{01}}\right) \phi_c^{Z_i}(\vec{k}_i, \vec{r}_0)\Phi(\vec{r}_1) d\vec{r}_0 d\vec{r}_1 d\vec{r}_{01} \tag{A.7}$$

To treat the terms involving $\vec{r}_{01}$ more efficiently, we follow the Fourier-transform approach proposed by Kornberg and Miraglia.

$$\begin{aligned} \phi(\vec{r}) &= \frac{1}{(2\pi)^{3/2}} \int e^{i\vec{p}\cdot\vec{r}} \tilde{\phi}(\vec{p}) d\vec{p} \\ \tilde{\phi}(\vec{p}) &= \frac{1}{(2\pi)^{3/2}} \int e^{-i\vec{p}\cdot\vec{r}} \phi(\vec{r}) d\vec{r} \end{aligned} \tag{A.8}$$

Such that:

$$\phi(\vec{r}) = \frac{1}{(2\pi)^3} \int e^{i\vec{p}\cdot\vec{r}} \int e^{-i\vec{p}\cdot\vec{r}'} \phi(\vec{r}') d\vec{r}' d\vec{p} \tag{A.9}$$

Applying the Fourier transform to the interaction term yields the following representation:

$$C^*(\alpha_{01}, \vec{k}_{s1}, \vec{r}_{01}) = \frac{1}{(2\pi)^3} \int e^{i\vec{p}\cdot\vec{r}_{01}} \int e^{-i\vec{p}\cdot\vec{r}'_{01}} C^*(\alpha_{01}, \vec{k}_{s1}, \vec{r}'_{01}) d\vec{r}'_{01} d\vec{p} \tag{A.10}$$

the equation (A.7) becomes:

$$\begin{aligned} T_{if}^{Int} = \frac{1}{(2\pi)^3} \int \Bigg(&\int \phi_c^{Z_e *}(\vec{k}_1, \vec{r}_1)\, e^{-i\vec{p}\cdot\vec{r}_1}\, \Phi(\vec{r}_1)\, d\vec{r}_1 \times \int \phi_c^{Z_s *}(\vec{k}_s, \vec{r}_0)\, \phi_c^{Z_i}(\vec{k}_i, \vec{r}_0)\, e^{i\vec{p}\cdot\vec{r}_0}\, d\vec{r}_0 \\ &\times \int \frac{C^*(\alpha_{01}, \vec{k}_{s1}, \vec{r}'_{01})}{\vec{r}'_{01}}\, e^{-i\vec{p}\cdot\vec{r}'_{01}}\, d\vec{r}'_{01} \Bigg) d\vec{p} \end{aligned} \tag{A.11}$$

By introducing two infinitesimal parameters λ_1 and λ_2 (tending to 0) to ensure convergence of the integrals, we obtain:

$$\begin{aligned} T_{if} = \frac{\sqrt{4\pi}}{(2\pi)^3} \lim_{\alpha\to 0} \lim_{\lambda\to 0} \int \Bigg(&\int \phi_c^{Z_e *}(\vec{k}_1, \vec{r}_1) e^{-i\vec{p}\cdot\vec{r}_1} \Phi(\vec{r}_1) d\vec{r}_1 \times \int \phi_c^{Z_s *}(\vec{k}_s, \vec{r}_0)\phi_c^{Z_i}(\vec{k}_i, \vec{r}_0) e^{i\vec{p}\cdot\vec{r}_0} e^{-\alpha r_0} Y_{100} d\vec{r}_0 \\ &\times \int C^*(\alpha_{01}, \vec{k}_{s1}, \vec{r}'_{01}) \frac{1}{r'_{01}} e^{i(\vec{k}_{01}-\vec{p})\cdot\vec{r}'_{01}} e^{-\lambda r_0} d\vec{r}'_{01} \Bigg) d\vec{p} \end{aligned} \tag{A.12}$$

To further simplify the calculation and improve computational efficiency, the integration over each term can be separated into finite and asymptotic regions based on the general behavior of the variable charge Z(r) as follows: On the one hand, we have:

$$\int_0^{\infty} \phi_c^{Z_e*}(\vec{k}_1,\vec{r}_1)e^{-i\vec{p}\cdot\vec{r}_1}\Phi(\vec{r}_1)d\vec{r}_1 = \int_0^{d} \phi_c^{Z_e*}(\vec{k}_1,\vec{r}_1)e^{-i\vec{p}\cdot\vec{r}_1}\Phi(\vec{r}_1)d\vec{r}_1 + \int_d^{\infty} \phi_c^{Z=1*}(\vec{k}_1,\vec{r}_1)e^{-i\vec{p}\cdot\vec{r}_1}\Phi(\vec{r}_1)d\vec{r}_1 \tag{A.13}$$

on the other hand, we have:

$$\int_d^{\infty} \phi_c^{Z=1*}(\vec{k}_1,\vec{r}_1)e^{-i\vec{p}\cdot\vec{r}_1}\Phi(\vec{r}_1)d\vec{r}_1 = \int_0^{\infty} \phi_c^{Z=1*}(\vec{k}_1,\vec{r}_1)e^{-i\vec{p}\cdot\vec{r}_1}\Phi(\vec{r}_1)d\vec{r}_1 - \int_0^{d} \phi_c^{Z=1*}(\vec{k}_1,\vec{r}_1)e^{-i\vec{p}\cdot\vec{r}_1}\Phi(\vec{r}_1)d\vec{r}_1 \tag{A.14}$$

Combining the previous two expressions, we can rewrite the integral in the more compact form:

$$\begin{aligned}\int_0^{\infty} \phi_c^{Z_e*}(\vec{k}_1,\vec{r}_1)e^{-i\vec{p}\cdot\vec{r}_1}\Phi(\vec{r}_1)d\vec{r}_1 &= \int_0^{d} (\phi_c^{Z_e*}(\vec{k}_1,\vec{r}_1) - \phi_c^{Z=1*}(\vec{k}_1,\vec{r}_1))e^{-i\vec{p}\cdot\vec{r}_1}\Phi(\vec{r}_1)d\vec{r}_1 \\ &+ \int_0^{\infty} \phi_c^{Z=1*}(\vec{k}_1,\vec{r}_1)e^{-i\vec{p}\cdot\vec{r}_1}\Phi(\vec{r}_1)d\vec{r}_1\end{aligned} \tag{A.15}$$

Substituting these results into Eq. (A.12), the transition matrix element T_{if} can be rewritten as:

$$\begin{aligned}T_{if} = \frac{\sqrt{4\pi}}{(2\pi)^3} \lim_{\alpha\to 0}\lim_{\lambda\to 0} \int \Bigg[&\Bigg\{ \int_0^{d} (\phi_c^{Z_e*}(\vec{k}_1,\vec{r}_1) - \phi_c^{Z=1*}(\vec{k}_1,\vec{r}_1))e^{-i\vec{p}\cdot\vec{r}_1}\Phi(\vec{r}_1)d\vec{r}_1 \\ &+ \int_0^{\infty} \phi_c^{Z=1*}(\vec{k}_1,\vec{r}_1)e^{-i\vec{p}\cdot\vec{r}_1}\Phi(\vec{r}_1)d\vec{r}_1 \Bigg\} \\ &\times \Bigg\{ \int (\phi_c^{Z_s*}(\vec{k}_s,\vec{r}_0)\phi_c^{Z_i}(\vec{k}_i,\vec{r}_0) - \phi_c^{Z=1*}(\vec{k}_s,\vec{r}_0)\phi_c^{Z=0}(\vec{k}_i,\vec{r}_0))e^{i\vec{p}\cdot\vec{r}_0}\psi_{100}(\vec{r}_0)d\vec{r}_0 \\ &+ \int \phi_c^{Z=1*}(\vec{k}_s,\vec{r}_0)\phi_c^{Z=0}(\vec{k}_i,\vec{r}_0))e^{i\vec{p}\cdot\vec{r}_0}\psi_{100}(\vec{r}_0)d\vec{r}_0 \Bigg\} \\ &\times \int C^*(\alpha_{01},\vec{k}_{s1},\vec{r}'_{01})\frac{1}{r'_{01}}e^{i(\vec{k}_{01}-\vec{p})\cdot\vec{r}'_{01}}e^{-\lambda r_0}d\vec{r}'_{01} \Bigg] d\vec{p}\end{aligned} \tag{A.16}$$

Following a similar procedure, the term T_{if}^0 associated with the $1/r_0$ interaction potential is obtained as:

$$T_{if}^0 = \iiint \phi_c^{Z_s*}(\vec{k}_s,\vec{r}_0)\phi_c^{Z_e*}(\vec{k}_1,\vec{r}_1)C^*(\alpha_{01},\vec{k}_{s1},\vec{r}_{01})\left(\frac{1}{r_0}\right)\phi_c^{Z_i}(\vec{k}_i,\vec{r}_0)\Phi(\vec{r}_1)d\vec{r}_0 d\vec{r}_1 d\vec{r}_{01} \tag{A.17}$$

$$
\begin{aligned}
T_{if}^{0} = \frac{1}{(2\pi)^3} \int \Bigg(\int \phi_c^{Z_e *}(\vec{k}_1, \vec{r}_1)\, e^{-i\vec{p}\cdot\vec{r}_1}\, \Phi(\vec{r}_1)\, d\vec{r}_1 \times \int \phi_c^{Z_s *}(\vec{k}_s, \vec{r}_0)\, \phi_c^{Z_i}(\vec{k}_i, \vec{r}_0)\, \frac{e^{i\vec{p}\cdot\vec{r}_0}}{r_0}\, d\vec{r}_0 \\
\times \int C^{*}(\alpha_{01}, \vec{k}_{s1}, \vec{r}\,'_{01})\, e^{-i\vec{p}\cdot\vec{r}\,'_{01}}\, d\vec{r}\,'_{01} \Bigg) d\vec{p}
\end{aligned}
\tag{A.18}
$$

Applying the same developements in Eq. (A.13) and Eq. (A.14), we get:

$$
\begin{aligned}
T_{if}^{0} = \frac{\sqrt{4\pi}}{(2\pi)^3} \lim_{\alpha\to 0} \lim_{\lambda\to 0} \int \Bigg[\Bigg\{ & \int_0^d (\phi_c^{Z_e *}(\vec{k}_1, \vec{r}_1) - \phi_c^{Z=1 *}(\vec{k}_1, \vec{r}_1)) e^{-i\vec{p}\cdot\vec{r}_1} \Phi(\vec{r}_1) d\vec{r}_1 \\
& + \int_0^\infty \phi_c^{Z=1 *}(\vec{k}_1, \vec{r}_1) e^{-i\vec{p}\cdot\vec{r}_1} \Phi(\vec{r}_1) d\vec{r}_1 \Bigg\} \\
& \times \Bigg\{ \int (\phi_c^{Z_s *}(\vec{k}_s, \vec{r}_0) \phi_c^{Z_i}(\vec{k}_i, \vec{r}_0) - \phi_c^{Z=1 *}(\vec{k}_s, \vec{r}_0) \phi_c^{Z=0}(\vec{k}_i, \vec{r}_0)) \frac{e^{i\vec{p}\cdot\vec{r}_0}}{r_0} e^{-\lambda r_0} d\vec{r}_0 \\
& + \int \phi_c^{Z=1 *}(\vec{k}_s, \vec{r}_0) \phi_c^{Z=0}(\vec{k}_i, \vec{r}_0)) \frac{e^{i\vec{p}\cdot\vec{r}_0}}{r_0} e^{-\lambda r_0} d\vec{r}_0 \Bigg\} \\
& \times \int C^{*}(\alpha_{01}, \vec{k}_{s1}, \vec{r}\,'_{01}) e^{i(\vec{k}_{01} - \vec{p})\cdot\vec{r}_0} \psi_{100}(\vec{r}\,'_{01}) d\vec{r}\,'_{01} \Bigg] d\vec{p}
\end{aligned}
\tag{A.19}
$$